



**US Army Corps
of Engineers**
Construction Engineering
Research Laboratory

2

AD-A207 746

The Relationship Between Ground Permittivity and the Input Impedance of a Horizontal Dipole Near Ground

by
John H. Spears

Transmitting antennas located near the earth have a problem with electromagnetic scattering caused by the ground. Researchers suggest that the inverse of this problem may be used to determine the complex permittivity of the ground. That application is the goal of this thesis.

The solution of the half-space problem was originally formulated in 1909 by Arnold Sommerfeld. Unfortunately, his formulation was written in terms of a set of integrals that tend to have a slow rate of convergence. Since then, researchers have sought faster methods of computing fields in the presence of an arbitrary infinite half space by making approximations to Sommerfeld's integrals to increase their convergence rate. Others have replaced the ground with an equivalent image current.

Much of the work on this subject has been directed toward the inverse scattering problem, i.e., inferring the dielectric properties of the ground by measuring scattered fields, using time-domain techniques or continuous-wave measurements.

In choosing one method over another, the parameters related to the properties of the ground should be large enough or small enough to be measured with reasonable accuracy. The experimental setup should be straightforward and simple, and the analysis should not be overly complex.

Relating the input impedance of a dipole near the ground to its permittivity was deemed a practical experimental technique. The input impedance of a half-wave dipole is around 75 ohms, well within the measurement range of modern RF impedance meters, and the experiment requires only a one-port measurement of a simple antenna. The analysis involved was manageable. The method chosen for theoretical analysis was an image approach that replaces the ground with an equivalent image current located on a line in complex space.

This study addresses the theory between the electric properties of the ground to the input impedance of a horizontal electric dipole, including numerical computations, patterns of the input impedance, practical considerations, and recommendations for experimental methods of determining the ground permittivity using this theory.

DTIC
ELECTE
MAY 12 1989
S A D
J.A.

REPORT DOCUMENTATION PAGE

1a REPORT SECURITY CLASSIFICATION UNCLASSIFIED		1b RESTRICTIVE MARKINGS	
2a SECURITY CLASSIFICATION AUTHORITY		3 DISTRIBUTION / AVAILABILITY OF REPORT Approved for public release; distribution is unlimited.	
2b DECLASSIFICATION / DOWNGRADING SCHEDULE		5 MONITORING ORGANIZATION REPORT NUMBER(S)	
4 PERFORMING ORGANIZATION REPORT NUMBER(S) USACERL Technical Manuscript M-89/05		7a NAME OF MONITORING ORGANIZATION	
6a NAME OF PERFORMING ORGANIZATION U.S. Army Construction Engr Research Laboratory	6b OFFICE SYMBOL (if applicable)	7b ADDRESS (City, State, and ZIP Code)	
6c ADDRESS (City, State, and ZIP Code) P.O. Box 4005 Champaign, IL 61824-4005		9 PROCUREMENT INSTRUMENT IDENTIFICATION NUMBER HDL project XE77E3, "Hardened Technology"	
8a NAME OF FUNDING / SPONSORING ORGANIZATION Harry Diamond Laboratories	8b OFFICE SYMBOL (if applicable) SLCHD-CS	10 SOURCE OF FUNDING NUMBERS	
8c ADDRESS (City, State, and ZIP Code) 2800 Powder Mill Road Adelphia, MD 20783-1197		PROGRAM ELEMENT NO	PROJECT NO
11 TITLE (Include Security Classification) The Relationship Between Ground Permittivity and the Input Impedance of a Horizontal Dipole Near Ground (U)		TASK NO	WORK UNIT ACCESSION NO
12 PERSONAL AUTHOR(S) John H. Spears			
13a TYPE OF REPORT Final	13b TIME COVERED FROM _____ TO _____	14 DATE OF REPORT (Year, Month, Day) 1989, April	15 PAGE COUNT 80
16 SUPPLEMENTARY NOTATION Copies are available from the National Technical Information Service, 5285 Port Royal Road, Springfield, VA 22161-0001			
17 COSATI CODES		18 SUBJECT TERMS (Continue on reverse if necessary and identify by block number)	
FIELD	GROUP	ground permittivity	
20	14	electromagnetic scattering	
		dipoles	
19 ABSTRACT (Continue on reverse if necessary and identify by block number)			
<p>Transmitting antennas located near the earth have a problem with electromagnetic scattering caused by the ground. Researchers suggest that the inverse of this problem may be used to determine the complex permittivity of the ground. That application is the goal of this thesis.</p> <p>The solution of the half-space problem was originally formulated in 1909 by Arnold Sommerfeld. Unfortunately, his formulation was written in terms of a set of integrals that tend to have a slow rate of convergence. Since then, researchers have sought faster methods of computing fields in the presence of an arbitrary infinite half space by making approximations to Sommerfeld's integrals to increase their convergence rate. Others have replaced the ground with an equivalent image current.</p> <p style="text-align: right;">(Cont'd)</p>			
20 DISTRIBUTION / AVAILABILITY OF ABSTRACT <input type="checkbox"/> UNCLASSIFIED/UNLIMITED <input checked="" type="checkbox"/> SAME AS RPT <input type="checkbox"/> DTIC USERS		21 ABSTRACT SECURITY CLASSIFICATION UNCLASSIFIED	
22a NAME OF RESPONSIBLE INDIVIDUAL Linda Wheatley		22b TELEPHONE (Include Area Code) (217)352-6511 (x354)	22c OFFICE SYMBOL CECER-IMT

BLOCK 19. (Cont'd)

Much of the work on this subject has been directed toward the inverse scattering problem, i.e., inferring the dielectric properties of the ground by measuring scattered fields, using time-domain techniques or continuous-wave measurements.

In choosing one method over another, the parameters related to the properties of the ground should be large enough or small enough to be measured with reasonable accuracy. The experimental setup should be straightforward and simple, and the analysis should not be overly complex.

Relating the input impedance of a dipole near the ground to its permittivity was deemed a practical experimental technique. The input impedance of a half-wave dipole is around 75 ohms, well within the measurement range of modern RF impedance meters, and the experiment requires only a one-port measurement of a simple antenna. The analysis involved was manageable. The method chosen for theoretical analysis was an image approach that replaces the ground with an equivalent image current located on a line in complex space.

This study addresses the theory between the electric properties of the ground to the input impedance of a horizontal electric dipole, including numerical computations, patterns of the input impedance, practical considerations, and recommendations for experimental methods of determining the ground permittivity using this theory.

TABLE OF CONTENTS

	PAGE
1. INTRODUCTION	1
2. DERIVATION OF IMPEDANCE EXPRESSIONS	3
3. NUMERICAL CONSIDERATIONS	18
4. IMPEDANCE CHARACTERISTICS	44
5. EXPERIMENTAL CONSIDERATIONS	66
6. CONCLUDING REMARKS	71
LIST OF REFERENCES	72

1. INTRODUCTION

The problem of electromagnetic scattering caused by the ground has been investigated by a great number of researchers over the past few decades. It is an important problem because transmitting antennas are often located near the earth. Many have suggested that the inverse of this problem may be used as a means of determining the complex permittivity of the ground [1,2,3,4,5]. The latter application is the goal of this paper.

The solution of the half-space problem was originally formulated in 1909 by Arnold Sommerfeld [6]. His formulation is written in terms of a set of integrals now commonly known as Sommerfeld integrals. Unfortunately, these integrals tend to have a slow rate of convergence. Since that time, many researchers have sought faster methods of computing fields in the presence of an arbitrary infinite half space. Some have made approximations to Sommerfeld's integrals to increase their rate of convergence [7,8,9]. Others have replaced the ground with an equivalent image current [10,11,12,13].

Many of the papers on this subject have been specifically directed toward the inverse scattering problem, i.e., inferring the dielectric properties of the ground by measuring scattered fields. Some suggested time-domain techniques [3,5]. Others discussed continuous-wave measurements [1,2,4].

In choosing one method over another, a number of considerations need to be taken into account. One, the parameters related to the properties of the ground should be easy to measure, i.e., they should be large enough or small enough that they can be measured with reasonable accuracy. Two, the experimental setup should be fairly straightforward and simple. Three, the analysis should not be overly complex.

After weighing these factors, it was decided that relating the input impedance of a dipole near the ground to its permittivity would be a practical experimental technique. The input impedance of a half-wave dipole can be expected to be around 75 ohms, well within the measurement range of modern RF impedance meters. The experiment requires only a one-port measurement of a simple antenna. The analysis involved is manageable.

The method chosen for theoretical analysis is an image approach developed by Lindell and Alanen [13,14,15,16]. They replaced the ground with an equivalent image current located on a line in complex space.

In Chapter 2, Lindell's image current is rederived for the special case of a horizontal electric dipole (HED) over a ground with complex permittivity $\epsilon = \epsilon_r \epsilon_0$ and magnetic permeability $\mu = \mu_0$. It is then applied to obtain an expression for the input impedance of an electric dipole of arbitrary length over ground.

Numerical results are given in Chapter 3, convergence of integrals is shown, and the limitations of some assumptions will be addressed.

In Chapter 4, the relationship between the permittivity of the ground and dipole impedance is discussed. Graphs are shown depicting the effects of dipole height and length on the impedances.

Finally, Chapter 5 addresses experimental considerations.

2. DERIVATION OF IMPEDANCE EXPRESSIONS

The derivation of the image current begins with the two-dimensional transform in the x-y plane of Maxwell's equations. The source will be an infinitesimal HED with current magnitude I , length L , direction \hat{x} , and location at a height $z = h$ above the ground.

Thus, after the transform of Maxwell's equations with respect to x and y , we have

$$\hat{z} \times \mathbf{E}' - j\mathbf{K} \times \mathbf{E} + j\omega\mu_0\mathbf{H} = 0 \quad z > 0 \quad (2.1)$$

$$\hat{z} \times \mathbf{H}' - j\mathbf{K} \times \mathbf{H} - j\omega\epsilon_0\mathbf{E} = IL\hat{x}\delta(z-h) \quad z > 0 \quad (2.2)$$

$$\hat{z} \times \mathbf{E}_1' - j\mathbf{K} \times \mathbf{E}_1 + j\omega\mu_0\mathbf{H}_1 = 0 \quad z > 0 \quad (2.3)$$

$$\hat{z} \times \mathbf{H}_1' - j\mathbf{K} \times \mathbf{H}_1 - j\omega\epsilon_1\mathbf{E}_1 = 0 \quad z > 0 \quad (2.4)$$

where \mathbf{K} is the two-dimensional transform variable, the prime indicates the derivative with respect to z , $\epsilon_1 = \epsilon_r\epsilon_0$, and a subscript of one denotes the earth. Note that the magnetic permeability is assumed to be the same as that of free space, since that is usually the case in nature. Equations (2.1) thru (2.4) can be uniquely expressed in terms of the transverse components of electric and magnetic fields, represented here by \mathbf{e} and \mathbf{h} . Therefore, after some manipulating and considering only the transverse fields, we are left with

$$\mathbf{e}' = j\frac{\eta}{\mathbf{K}} (\mathbf{I}_t k^2 - \mathbf{K}\mathbf{K}) \times \hat{z} \cdot \mathbf{h} \quad (2.5)$$

$$\mathbf{h}' = -j\frac{1}{\mathbf{K}} (\mathbf{I}_t k^2 - \mathbf{K}\mathbf{K}) \times \hat{z} \cdot \mathbf{e} \quad (2.6)$$

$$\mathbf{e}_1' = j\frac{\eta_1}{\mathbf{K}_1} (\mathbf{I}_t k_1^2 - \mathbf{K}\mathbf{K}) \times \hat{z} \cdot \mathbf{h}_1 \quad (2.7)$$

$$\mathbf{h}_1' = -j\frac{1}{\mathbf{K}_1} (\mathbf{I}_t k_1^2 - \mathbf{K}\mathbf{K}) \times \hat{z} \cdot \mathbf{e}_1 \quad (2.8)$$

The two-dimensional idem dyadic is $\underline{\underline{I}}_t$. Also, $\eta = \sqrt{\mu_0/\epsilon_0}$, $\eta_1 = \sqrt{\mu_0/\epsilon_1}$, $k = \omega\sqrt{\mu_0\epsilon_0}$, and $k_1 = \omega\sqrt{\mu_0\epsilon_1}$. For the sake of clarification, dyadics will be represented by double underlined capital letters except at times when their meaning is better conveyed by writing two vectors next to each other, e.g., $\nabla\nabla$.

Note that the above equations are of the same form as the telegrapher's equations.

$$\underline{U}'(z) = -z_d \underline{I}(z) + u(z) \quad (2.9)$$

$$\underline{I}'(z) = -y_d \underline{U}(z) + i(z). \quad (2.10)$$

This similarity opens the possibility of representing each medium by an equivalent distributed impedance. If the voltage represents e and the current h , the corresponding distributed impedance and admittance are dyadics given by

$$\underline{\underline{Z}}_d = -j\eta (\underline{\underline{I}}_t k^2 - \underline{\underline{K}}\underline{\underline{K}}) \times \hat{z} \quad z > 0 \quad (2.11)$$

$$\underline{\underline{Y}}_d = \frac{-j}{\eta} (\underline{\underline{I}}_t k^2 - \underline{\underline{K}}\underline{\underline{K}}) \times \hat{z} \quad z > 0. \quad (2.12)$$

A subscript of one is added when $z < 0$. The product of $\underline{\underline{Z}}_d$ and $\underline{\underline{Y}}_d$ is

$$\underline{\underline{Z}}_d \cdot \underline{\underline{Y}}_d = -(k^2 - K^2) \underline{\underline{I}}_t = -\beta^2 \underline{\underline{I}}_t. \quad z > 0. \quad (2.13)$$

Here, β is the z -component of the wave number, k , given by

$$\beta = \sqrt{k^2 - K^2}, \quad \beta_1 = \sqrt{\epsilon_r k^2 - K^2} = \sqrt{(\epsilon_r - 1)k^2 - \beta^2} \quad (2.14)$$

and K is the magnitude of the vector $\underline{\underline{K}}$. The branches of β and β_1 are taken such that their arguments are between $-\pi$ and 0 . The reason for this choice will be made clear, as it will insure that the electric field approaches zero as $z \rightarrow \infty$ in Equation (2.24).

Now that the equivalent impedance is known, the next step is to find a suitable reflection dyadic.

$$\underline{\underline{R}} = (\underline{\underline{Z}}_1 - \underline{\underline{Z}}) \cdot (\underline{\underline{Z}}_1 + \underline{\underline{Z}})^{-1} \quad (2.15)$$

The inverse of a two-dimensional dyadic is the same as that of its associated matrix.

$$\underline{\mathbf{A}}^{-1} = \frac{\text{adj}(\underline{\mathbf{A}})}{\det(\underline{\mathbf{A}})}, \quad (2.16)$$

where $\text{adj}(\underline{\mathbf{A}})$ and $\det(\underline{\mathbf{A}})$ are the adjoint and determinant of the associated matrix. Applying (2.16) to the inverse dyadic in (2.15) and simplifying the result yield the following reflection dyadic:

$$\underline{\mathbf{R}} = R^{\text{TM}} \mathbf{K}\mathbf{K}/K^2 + R^{\text{TE}} \text{adj}(\mathbf{K}\mathbf{K})/K^2. \quad (2.17)$$

R^{TM} and R^{TE} are the familiar reflection coefficients for the transverse magnetic and transverse electric cases. They are given by

$$R^{\text{TE}} = \frac{\beta - \beta_1}{\beta + \beta_1} = \frac{\beta - \sqrt{(\epsilon_r - 1)k^2 + \beta^2}}{\beta + \sqrt{(\epsilon_r - 1)k^2 + \beta^2}} \quad (2.18)$$

$$R^{\text{TM}} = \frac{\epsilon_r \beta - \beta_1}{\epsilon_r \beta + \beta_1} = \frac{\epsilon_r \beta - \sqrt{(\epsilon_r - 1)k^2 + \beta^2}}{\epsilon_r \beta + \sqrt{(\epsilon_r - 1)k^2 + \beta^2}}. \quad (2.19)$$

The general form of this reflection dyadic was derived by Lindell in [13]. Here R^{TE} has been made more specific by setting $\mu = \mu_0$. The adjoint operator and the denominator K^2 make the reflection dyadic in (2.17) somewhat awkward to work with. Applying the dyadic property

$$\text{adj}(\mathbf{K}\mathbf{K}) = K^2 \underline{\mathbf{I}}_t - \mathbf{K}\mathbf{K}, \quad (2.20)$$

$\underline{\mathbf{R}}$ can be written

$$\underline{\mathbf{R}} = R^{\text{TE}} \underline{\mathbf{I}}_t + R_0 \mathbf{K}\mathbf{K}/k^2, \quad (2.21)$$

$$\text{with } R_0 = k^2(R^{\text{TM}} - R^{\text{TE}})/K^2 = \frac{2(\epsilon_r - 1)k^2}{(\beta + \beta_1)(\epsilon_r \beta + \beta_1)} = \frac{\epsilon_r + 1}{\epsilon_r} \left(R^{\text{TM}} + \frac{\epsilon_r - 1}{\epsilon_r + 1} \right). \quad (2.22)$$

This form isolates the transform variable \mathbf{K} to a dyadic in only one of the terms. Thus, the inverse transform of the dyadic part of $\underline{\mathbf{R}}$ is accomplished by simply replacing $\mathbf{K}\mathbf{K}$ with $-\nabla_t \nabla_t$, where ∇_t is the x-y component of the vector operator ∇ .

Substituting \mathbf{h}' from (2.6) into (2.5), a Helmholtz-like equation is obtained.

$$\mathbf{e}'' + \beta^2 \mathbf{e} = j\omega\mu_0 \text{IL}(\underline{\mathbf{I}}_t k^2 - \mathbf{K}\mathbf{K})/k^2 \delta(z-h). \quad (2.23)$$

From this, the electric field is found to be

$$\mathbf{e} = \frac{-j\omega\mu_0}{2\beta} \text{IL}(\underline{\mathbf{I}}_t - k^{-2}\mathbf{K}\mathbf{K}) \cdot \hat{\mathbf{x}} \cdot (\underline{\mathbf{I}}_t e^{-j\beta|z+h|} + \underline{\mathbf{R}} e^{-j\beta(z+h)}) \quad z > 0. \quad (2.24)$$

Although \mathbf{h} can be derived similarly, it will not be necessary to discuss both \mathbf{e} and \mathbf{h} . Note that the first term above is that portion of the field associated with a dipole in free space and is travelling away from the $z = h$ plane. The second term is travelling upward and can be thought of as a wave reflected from the earth.

This leads us to represent the electric field as the sum of the well-known free-space field, \mathbf{E}_1 , and the electric field scattered from the ground, \mathbf{E}_2 .

$$\mathbf{E} = \mathbf{E}_1 + \mathbf{E}_2 \quad (2.25)$$

$$\mathbf{E}_1 = -j\omega\mu_0 \int \underline{\mathbf{G}}(|\mathbf{r}+\hat{\mathbf{z}}l|) \cdot \hat{\mathbf{x}} I(x) dx, \quad (2.26)$$

where $\underline{\mathbf{G}}(\mathbf{r})$ is the free-space Green's dyadic function $(\underline{\mathbf{I}} - \nabla\nabla)G(d)$, and $G(d) = (e^{-jk d})/4\pi d$. Notice that taking the inverse Fourier transform of the first term of (2.24) yields only the transverse components of \mathbf{E}_1 . Yet, the sole difference between \mathbf{E}_1 and the transverse fields is that (2.24) produces the dyadic operator $(\underline{\mathbf{I}}_t + \nabla_t \nabla_t)$ instead of $(\underline{\mathbf{I}} - \nabla\nabla)$. This simple relationship will be called on later to recover the z-component of \mathbf{E}_2 rather than carry longitudinal components through the derivation.

At this point, instead of taking the inverse Fourier transform of (2.25) (as is normally done), the reflection dyadic will be represented as the Laplace transform of a function:

$$\underline{\mathbf{R}}(\beta) = \int_0^{\infty} \underline{\mathbf{F}}(t) e^{-\beta t} dt . \quad (2.27)$$

After inserting (2.27) in (2.25), changing the order of transformation, and taking the inverse Fourier transform, the solution of \mathbf{E}_2 becomes

$$\mathbf{E}_2 = -j\omega\mu_0\mathbb{L} \int_0^{\infty} \underline{\mathbf{G}}(\mathbf{r}+\hat{\mathbf{z}}(h-jt)) \cdot \underline{\mathbf{F}}(t) \cdot \hat{\mathbf{x}} dt , \quad (2.28)$$

which implies that the ground can be replaced by an equivalent image current.

$$\begin{aligned} \mathbf{E}_2(\mathbf{r}) &= -j\omega\mu_0 \int_{-h}^{\infty} \underline{\mathbf{G}}(\mathbf{r}-\mathbf{z}'\hat{\mathbf{z}}) \cdot \underline{\mathbf{I}}(\mathbf{z}') dz' \\ \underline{\mathbf{I}}(\mathbf{z}') &= -j\mathbb{L} \underline{\mathbf{F}}(-j(z'+h)) \cdot \hat{\mathbf{x}} \\ z' &= jt - h . \end{aligned} \quad (2.29)$$

What remains to the solution is to find an expression for the dyadic, $\underline{\mathbf{F}}(t)$. If we solve Equation (2.27) for $\underline{\mathbf{F}}(t)$, we find that the inverse Laplace transform can be broken into two parts:

$$\underline{\mathbf{F}}(t) = \mathbb{L}^{-1}\{\mathbf{R}^{\text{TE}}\} \underline{\mathbf{I}}_t - \mathbb{L}^{-1}\{\mathbf{R}_0\} \mathbf{K}\mathbf{K}/k^2 . \quad (2.30)$$

The inverse transform of \mathbf{R}^{TE} can be found in the Laplace transform tables [18] or [19] to be

$$\mathbb{L}^{-1}\{\mathbf{R}^{\text{TE}}\} = \frac{-2 J_2\left(kt\sqrt{\epsilon_r-1}\right)}{t} \quad (2.31)$$

$$= \frac{-2 J_2(-jk(z'+h)\sqrt{\epsilon_r-1})}{z'+h} \quad (2.32)$$

Thus, the contribution of the first term of $\underline{\mathbf{R}}$ in (2.22) to the image current is

$$I_{ia}(p) = \frac{-2I L J_2(-jk(z'+h)\sqrt{\epsilon_r-1})}{z'+h} \cdot \hat{x} \quad (2.33)$$

On inspection, it is noted that if z' in (2.32) is real the Bessel function will have a complex argument and, therefore, become singular as z' approaches infinity. In fact, to insure convergence, the argument of the Bessel function must be real. Hence, it is set equal to the positive real variable p :

$$p = -jk(z'+h)\sqrt{\epsilon_r-1} \quad (2.34)$$

This forces z' to be a complex number given by

$$z' = -h + \frac{j p}{k\sqrt{\epsilon_r-1}} \quad (2.35)$$

Using this definition of z' , the electric field due to this image current can be written as

$$E_{2a} = 2j\omega\mu_0 \int_0^{\infty} \underline{\mathbf{G}}(d) \cdot \hat{x} \frac{J_2(p)}{p} dp \quad (2.36)$$

The branch of the distance function, d , is defined as $-\pi < \arg(d) \leq 0$ to insure that the Green's function asymptotically approaches zero allowing the integral of E_{2a} to converge. With this definition of the branch of d , the integral in (2.36) is fairly well behaved. In fact, it decays exponentially after p is large enough to dominate the exponent of the Green's function. Therefore, the integration can be performed numerically using a simple computer routine. The numeric evaluation of this integral will be discussed in further detail in the next chapter.

The inverse transform of the second term of the reflection dyadic, R_0 , is somewhat more difficult than the first one. Because R_0 is essentially R^{TM} plus a constant, we will begin by taking the inverse transform of R^{TM} . As a matter of convenience, the transform variable β will be replaced by $qk\sqrt{\epsilon_r-1}$ to give

$$R^{TM} = \frac{\epsilon_r q - \sqrt{q^2+1}}{\epsilon_r q - \sqrt{q^2+1}}, \quad (2.37)$$

where q can be thought of as a dimensionless, normalized propagation constant. After rearranging (2.37) and applying the Laplace transform property of differentiation, R^{TM} can be expressed in the form

$$R^{TM} = \frac{\epsilon_r-1}{\epsilon_r+1} - \frac{\epsilon_r \gamma^2}{q^2-\gamma^2} + \frac{\epsilon_r \gamma^2}{q^2-\gamma^2} (q - \sqrt{q^2+1})^2. \quad (2.38)$$

Here, γ is defined as $1/\sqrt{\epsilon_r^2-1}$. The first term above corresponds to a delta function in the spatial domain. The second is the transform of the hyperbolic sine. The inverse transform of the third term can be expressed as the convolution of a hyperbolic sine and a Bessel function.

$$\begin{aligned} f(p) &= L^{-1}\{R^{TM}\} \\ &= \frac{\epsilon_r-1}{\epsilon_r+1} \delta(p) - \epsilon_r \gamma \frac{\epsilon_r-1}{\epsilon_r+1} \sinh(\gamma p) + 2\epsilon_r \gamma \int_0^p \sinh(\gamma(p-s)) \frac{J_2(p)}{p} dp. \end{aligned} \quad (2.39)$$

The above transforms and transform properties can be found in [17] and [18].

At first glance, the hyperbolic-sine functions make $f(p)$ appear to diverge as p approaches infinity. However, the second and third terms tend to cancel for large p , causing $f(p)$ to approach zero in the limit as p approaches infinity. Yet, these terms also create significant round-off error making the form of $f(p)$ in (2.39) impractical for

numerical computation. Hence, another representation of $f(p)$ will be necessary. Taking advantage of the property

$$\int_0^{\infty} f(p) e^{-\gamma p} dp = \frac{\epsilon_r - 1}{\epsilon_r + 1}, \quad (2.40)$$

$f(p)$ can be written as

$$f(p) = \frac{\epsilon_r - 1}{\epsilon_r + 1} \delta(p) + f_{\epsilon}(p) \quad (2.41)$$

$$f_{\epsilon}(p) = \int_0^{\infty} e^{-\gamma s} \left(\frac{J_2(s-p)}{s-p} - \frac{J_2(s+p)}{s+p} \right) ds \quad (2.42)$$

Here we introduce the function $f_{\epsilon}(p)$ as the nonsingular part of $f(p)$. Note also that $(\epsilon_r + 1)f_{\epsilon}(p)/\epsilon_r$ is the inverse transform of R_0 . For ease of numerical calculation, Lindell [16] expressed the integral (2.42) as a couple of series expansions.

$$f_{\epsilon}(p) = \epsilon_r \gamma^2 \sum_{n=1}^{\infty} n \left(\frac{\epsilon_r - 1}{\epsilon_r + 1} \right)^n \frac{J_2(p)}{p} \quad (2.43)$$

$$\begin{aligned} f_{\epsilon}(p) \sim & -2\epsilon_r^2 \gamma^3 e^{-\gamma p} + \frac{2\sqrt{2}}{\epsilon_r p^{3/2} \sqrt{\pi}} \sin(p+\pi/4) + \frac{3(8-3\epsilon_r^2)}{2\epsilon_r^3 p^{5/2} \sqrt{2\pi}} \cos(p+\pi/4) \\ & + \frac{15}{\epsilon_r^3 p^{7/2} \sqrt{2\pi}} \left(-\frac{23}{32} + \frac{9}{2\epsilon_r^2} - \frac{4}{\epsilon_r^4} \right) \sin(p+\pi/4) \\ & - \frac{105}{2\epsilon_r^3 p^{9/2} \sqrt{2\pi}} \left(-\frac{91}{128} + \frac{59}{16\epsilon_r^2} - \frac{7}{\epsilon_r^4} + \frac{4}{\epsilon_r^6} \right) \cos(p+\pi/4). \end{aligned} \quad (2.44)$$

The series (2.43) is an exact representation of $f_{\epsilon}(p)$. However, it does not begin to converge until $2n > p$. Thus, (2.44), an asymptotic expansion of $f_{\epsilon}(p)$, serves as a better

means of calculating it for large p . Reference [15] describes a method that can be used to obtain the full series representation of (2.44). It was found by trial and error that $p = 5$ is a fairly good point to make the transition between (2.43) and (2.44).

Note that for the special case of $\epsilon_r = 1$, $f_\epsilon(p)$ becomes $f_1(p) = -2J(p)/p$. This is the same as the inverse transform of R^{TE} . It is also convenient to mention at this time that $f_\epsilon(p)$ satisfies the differential equation

$$\left((\epsilon_r^2 - 1) \frac{d^2}{dp^2} - 1 \right) f_\epsilon(p) = - \left(f_1(p) + \frac{1 - \epsilon_r}{1 + \epsilon_r} \delta(p) \right). \quad (2.45)$$

This is seen by applying the transform property of differentiation in conjunction with the inverse transform of (2.37).

The dyadic $\underline{\underline{F}}(p)$ can now be expressed in terms of the two functions $f_1(p)$ and $f_\epsilon(p)$.

$$\underline{\underline{F}}(p) = f_1(p) \underline{\underline{I}} - \frac{\epsilon_r + 1}{\epsilon_r} f_\epsilon(p) \nabla \nabla k^{-2}. \quad (2.46)$$

It follows that the scattered electric field is

$$\mathbf{E}_2 = -j\omega\mu_0 \mathbf{I} L \int_0^\infty \underline{\underline{G}} \left(\mathbf{r} - \left(\mathbf{r}' - \frac{j p}{k \sqrt{\epsilon_r - 1}} \hat{z} \right) \right) \cdot \underline{\underline{F}}(p) \cdot \hat{\mathbf{x}} dx. \quad (2.47)$$

Therefore, the image current is

$$\begin{aligned} \mathbf{I}_i &= \underline{\underline{F}}(p) \cdot \hat{\mathbf{x}} \mathbf{I} L \\ &= \left(f_1(p) \underline{\underline{I}} + \frac{\epsilon_r + 1}{\epsilon_r} f_\epsilon(p) \nabla \nabla k^{-2} \right) \cdot \hat{\mathbf{x}} \mathbf{I} L. \end{aligned} \quad (2.48)$$

If (2.48) is generalized, to allow the current to be a function of \mathbf{x} , the image becomes

$$I_i = f_1(p)I(x)\hat{x} - \frac{j(\epsilon_r+1)}{\epsilon_r k \sqrt{\epsilon_r-1}} f'_\epsilon(p)I'(x)\hat{z} . \quad (2.49)$$

where $-jk\sqrt{\epsilon_r-1} dz = dp$. Thus, the image current associated with an HED, depicted in Fig. 2.1 (all figures appear at the end of each chapter), consists of a horizontal and a vertical component both along the same line in the complex z -plane. As would be expected, both components decay to zero as p becomes large.

Finding an expression for the input impedance of the HED defined in Fig. 2.2 using the image current above is a straightforward procedure using image currents. The input impedance is defined by the stationary functional

$$Z = -\frac{1}{I_0^2} \int \mathbf{E} \cdot \hat{x} I(x) dx . \quad (2.50)$$

The electric field, given in (2.26) and (2.47), can be plugged into (2.50) to give

$$Z = \frac{jk\eta}{I_0^2} \iint I(x) \hat{x} \cdot \underline{\underline{G}}(|r-r'|) \cdot \hat{x} I(x') dx' dx \\ + \frac{jk\eta}{I_0^2} \iint \int_0^\infty I(x) \hat{x} \cdot \underline{\underline{G}}(|r-(r'-jp/\sqrt{\epsilon_r-1})|) \cdot \underline{\underline{F}}(p) \cdot \hat{x} I(x') dp dx' dx . \quad (2.51)$$

Equation (2.51) implies that the impedance, like the electric field, can be expressed as the sum of the free-space impedance and the change in impedance due to the ground. That can be done, of course, only if the current distribution is not significantly changed by the ground. The validity of this assumption will be discussed in Chapter 3. After evaluating the dyadics and applying the differential equation (2.45), ΔZ can be written as

$$\Delta Z = \frac{jk\eta}{I_0^2} \iint I(x)I(x')K_1(|x-x'|)I'(x)I'(x') \left(\frac{1}{\epsilon_r} K_\epsilon(|x-x'|) - \frac{\epsilon_r-1}{\epsilon_r+1} G(D_0) \right) dx' dx, \quad (2.52)$$

where

$$K_{\epsilon}(|x-x'|) = \int_0^{\infty} f_{\epsilon}(p)G(D) dp \quad (2.53)$$

$$K_1(|x-x'|) = \int_0^{\infty} f_1(p)G(D) dp \quad (2.54)$$

$$D(p) = \sqrt{(x-x')^2 + \left(2h - \frac{jp}{k\sqrt{\epsilon_r-1}}\right)^2} \quad (2.55)$$

$$D_0 = D(p=0) = \sqrt{(x-x')^2 + 4h^2}. \quad (2.56)$$

If a sinusoidal current is assumed for the case of a half-wave-dipole, the impedance change is

$$\begin{aligned} \Delta Z = jk\eta \int_{-\lambda/4}^{\lambda/4} \int_{-\lambda/4}^{\lambda/4} \cos(kx)\cos(kx')K_1(|x-x'|) \\ - \sin(kx)\sin(kx') \left(\frac{1}{\epsilon_r} K_{\epsilon}(|x-x'|) - \frac{\epsilon_r-1}{\epsilon_r+1} G(D_0) \right) dx' dx. \quad (2.57) \end{aligned}$$

A change of variables of $\theta = k|x-x'|$ and $\phi = k|x+x'|$ allows one of the integrals in (2.57) to be done analytically leaving

$$\begin{aligned} \Delta Z = jk\eta \int_0^{\pi} (\sin\theta + (\pi-\theta)\cos\theta)K_1(|x-x'|) \\ + (\sin\theta + (\pi-\theta)\cos\theta) \left(\frac{1}{\epsilon_r} K_{\epsilon}(|x-x'|) - \frac{\epsilon_r-1}{\epsilon_r+1} G(D_0) \right) dx' dx. \quad (2.58) \end{aligned}$$

The integrand of (2.58) is very well behaved, and is not difficult to integrate numerically.

For a dipole of arbitrary length, $2H$, and current distribution, $\sin(k(H-|z|))$, the impedance change is

$$\Delta Z = \frac{j\eta}{kI_0^2} \int_0^{kH} \left(AK_1(\theta/k) - B \left(\frac{1}{\epsilon_r} K_\epsilon(|x-x'|) - \frac{\epsilon_r-1}{\epsilon_r+1} G(D_0) \right) \right) d\theta$$

$$+ \frac{j\eta}{kI_0^2} \int_{kH}^{2kH} \left(CK_1(\theta/k) - D \left(\frac{1}{\epsilon_r} K_\epsilon(|x-x'|) - \frac{\epsilon_r-1}{\epsilon_r+1} G(D_0) \right) \right) d\theta \quad (2.59)$$

with

$$I_0 = \sin(kH) \quad (2.60)$$

$$A = -(\cos 2kH + \theta \sin 2kH + 1) \sin \theta + (\theta + (2kH - 2\theta) \cos 2kH) \cos \theta + \sin(2kH - \theta)$$

$$B = (\cos 2kH + 1) \sin \theta + (\theta + (2kH - 2\theta) \cos 2kH + \sin 2kH) \cos \theta + \sin(2kH - \theta)$$

$$+ \sin 2kH \cos(2kH - \theta)$$

$$C = (2kH - 2\theta) \cos \theta - \cos 2kH \sin(2kH - \theta)$$

$$D = (2kH - 2\theta) \cos \theta + \cos 2kH \sin(2kH - \theta).$$

Equation (2.60) shows that the expressions representing the coefficients A-D are long. However, they are much more efficient than the alternative which is the double integration of (2.58).

As the dipole height increases, the integral (2.58) can be approximated by an algebraic expression. For large kh , $D(p)$ becomes $2h - jp/\sqrt{\epsilon_r-1}$. Hence, by applying the integral identity

$$\int_0^\infty f_1(p) e^{-p/\sqrt{\epsilon_r-1}} dp = \frac{1-\sqrt{\epsilon_r}}{1+\sqrt{\epsilon_r}} \quad (2.61)$$

The new Green's function, K_1 , can be simplified to

$$K_1 \cong - \left(\frac{1-\sqrt{\epsilon_r}}{1+\sqrt{\epsilon_r}} \right) \frac{e^{-j2kh}}{2\pi h} \quad kh \rightarrow \infty. \quad (2.62)$$

Since the Green's function K_e is no longer a function of θ , the double integration for the currents can be performed analytically. The resulting expression is equivalent to the image reflection coefficient approximation.

$$\Delta Z \sim \frac{-jh}{2\pi kh} \left(\frac{1 - \sqrt{\epsilon_r}}{1 + \sqrt{\epsilon_r}} \right) e^{-j2kh} \quad kh \rightarrow \infty. \quad (2.63)$$

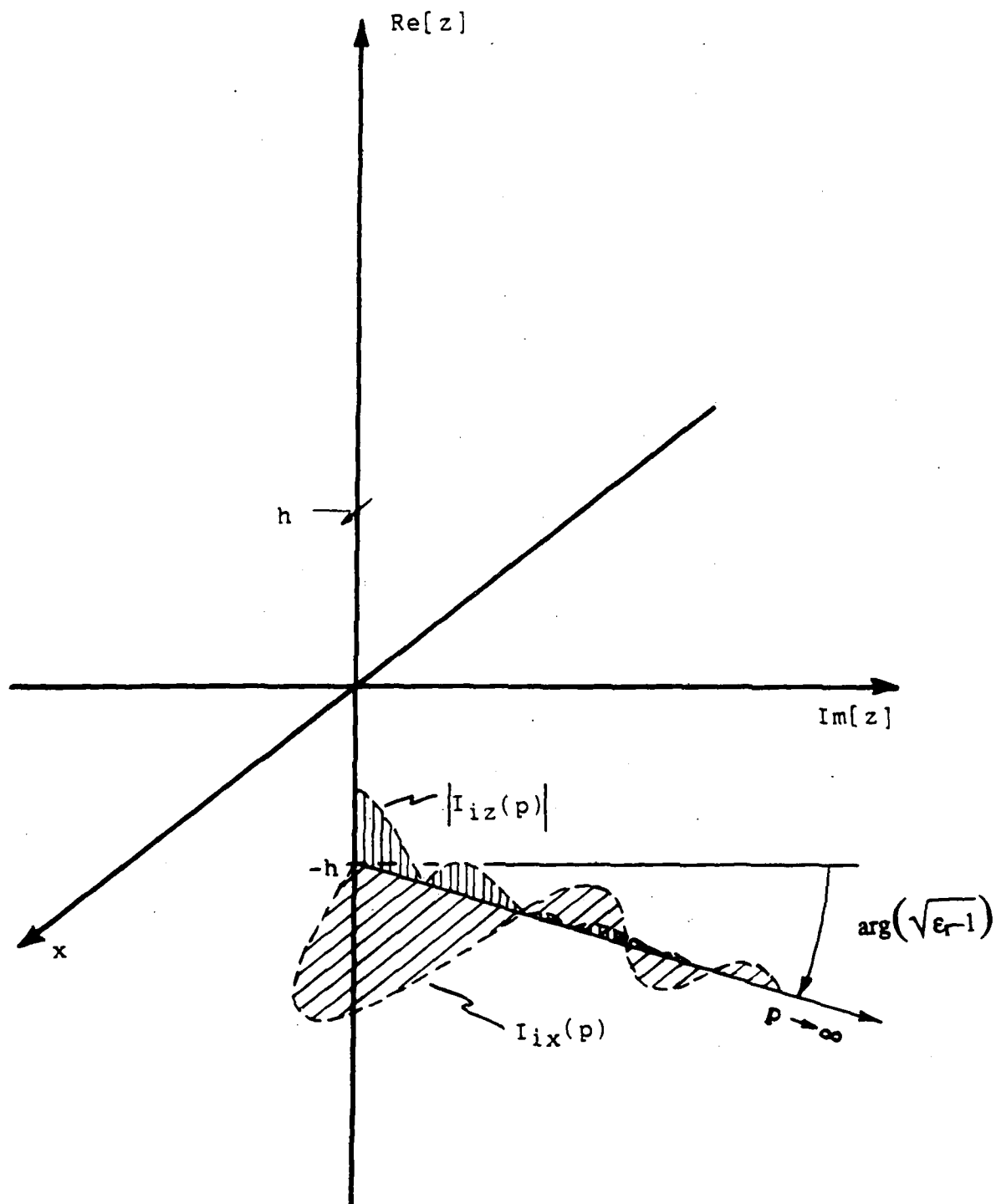


Figure 2.1. Image current due to HED over an infinite half space of complex permittivity, ϵ . The current lies in the complex z -plane and has two parts: I_{ix} parallel to the dipole, and I_{iz} oriented vertically.

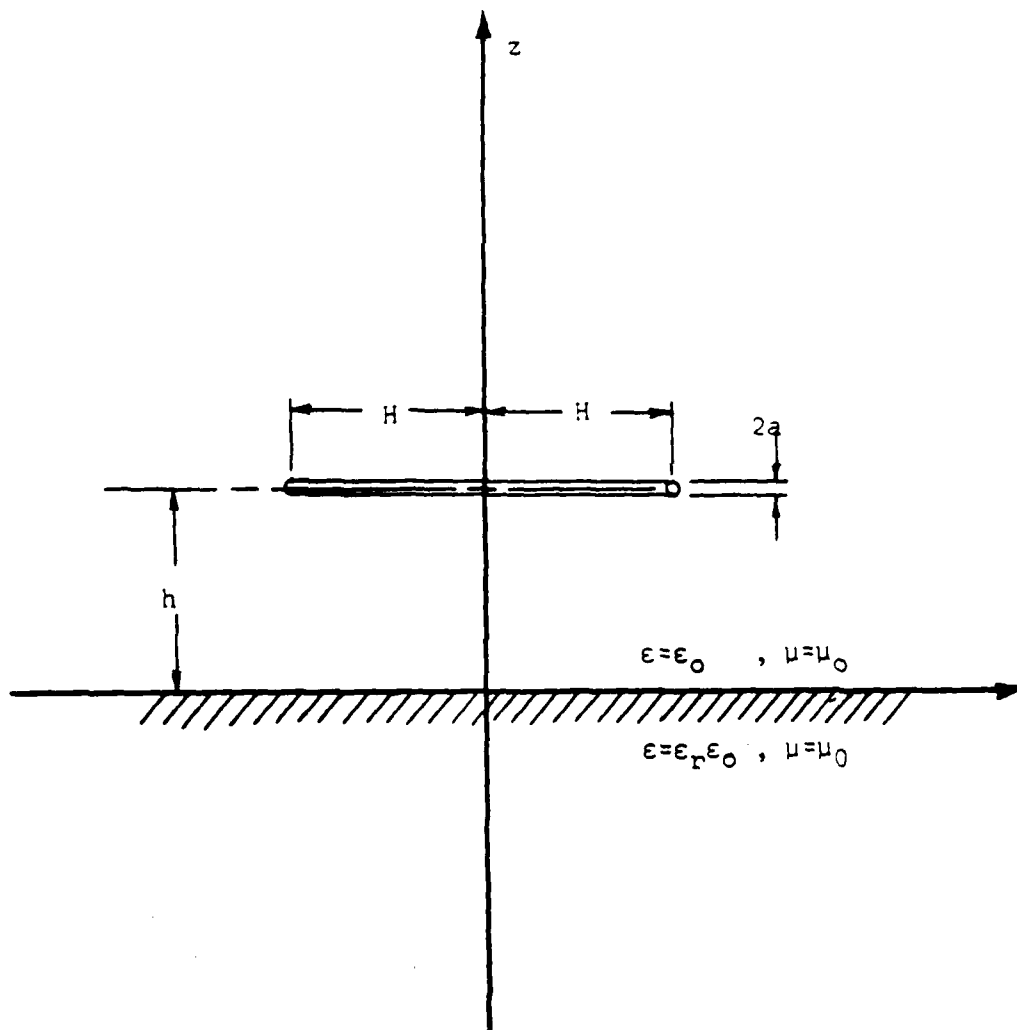


Figure 2.2. Depiction of an electric dipole above an arbitrary ground plane.

3. NUMERICAL CONSIDERATIONS

In this Chapter, the graphical characteristics of some of the equations given in Chapter 1 are presented. To begin, the transcendental function $f_\epsilon(p)$ is studied. This is followed by a discussion of the integrand of $K_\epsilon(\theta)$ and its integration to infinity.

The function $f_\epsilon(p)$, represented by Equations (2.43) and (2.44), was coded as a Fortran subroutine to be used later in calculating dipole impedances. As a test of the subroutine, Figures 3.1 through 3.5 were generated and compared with those published by Lindell [15,16]. Figures 3.1 through 3.4 agree quite well with Lindell's. These graphs demonstrate the general appearance of $f_\epsilon(p)$. Notice that for small ϵ_r , the functions are much larger near the origin. On the other hand, as the permittivity increases, the magnitude of $f_\epsilon(p)$ is more evenly distributed along the p-axis. In fact, when $\epsilon_r = 50$ (Figure 3.2), $f_\epsilon(p)$ is practically a line with a small downward slope.

Upon close inspection of Figures 3.1 through 3.5, one can see a very slight discontinuity in the curves at $p = 5$. This is seen best in Figure 3.2 when $\epsilon_r = 10$. It is caused by the inexactness of the asymptotic approximation at the transition between Equations (2.43) and (2.44). In the case of impedance calculations, this bump causes negligible error. However, there may be some applications that require higher accuracy. If this is the case, the transition between the two representations can be moved to a higher p , or the method described in [15] could be used to generate the next few terms of the asymptotic expansion.

Figures 3.5 through 3.7 show how the magnitude of $f_\epsilon(p)$ is affected by the argument of ϵ_r . A quick comparison of Figure 3.5 and Lindell's [16] results (Figure 3.8) shows a discrepancy for large $\arg(\epsilon_r)$. To determine which is correct, we need only inspect Equation (2.44), the first few terms of which are

$$\begin{aligned}
f_{\epsilon}(p) \sim & -2\epsilon_r^2 \gamma^3 e^{-\gamma p} + \frac{2\sqrt{2}}{\epsilon_r p^{3/2} \sqrt{\pi}} \sin(p+\pi/4) + \frac{3(8-3\epsilon_r^2)}{2\epsilon_r^3 p^{5/2} \sqrt{2\pi}} \cos(p+\pi/4) \\
& + \frac{15}{\epsilon_r^3 p^{7/2} \sqrt{2\pi}} \left(-\frac{23}{32} + \frac{9}{2\epsilon_r^2} - \frac{4}{\epsilon_r} \right) \sin(p+\pi/4). \quad (3.1)
\end{aligned}$$

We see that the second term and higher-order terms tend to zero for all values of ϵ_r as p becomes large. The first term decays with an attenuation constant $\tau = \gamma = \operatorname{Re}\left(\sqrt{\epsilon_r^2 - 1}\right)^{-1}$, $\tau \geq 0$. If we take the extreme case of the permittivity being completely imaginary, we see that $\tau = 0$ and $f_{\epsilon}(p)$ approaches the expression

$$f_{\epsilon}(p) \sim 2\epsilon_r^2 \gamma^3 e^{-\gamma p}, \quad \operatorname{Re}(\epsilon_r) = 0. \quad (3.2)$$

In fact, for this case, $f_{\epsilon}(p)$ approaches a helical form as $p \rightarrow \infty$. Therefore, Figure 3.5 is the more accurate graph. At first glance, it may be disturbing that the image currents do not decay to zero as $p \rightarrow \infty$. However, $f_{\epsilon}(p)$ can be thought of as a distribution. In a distribution sense, the limit as p approaches infinity can be treated as zero. This follows from the Riemann-Lebesgue lemma [19].

The program used to generate $f_{\epsilon}(p)$ was then tested in the two integral properties

$$\int_0^{\infty} f_{\epsilon}(p) dp = \frac{-2\epsilon_r}{\epsilon_r + 1} \quad (3.3)$$

$$\int_0^{\infty} f_1(p) e^{-p/\sqrt{\epsilon_r - 1}} dp = \frac{1 - \sqrt{\epsilon_r}}{1 + \sqrt{\epsilon_r}}. \quad (3.4)$$

The integrations were performed with an adaptive trapezoidal routine that was truncated when the integrand became negligible. The results varied with the step size and the point of truncation. It is apparent from the results of this test, shown in Table 3.1 (p. 23), that the computation of $f_{\epsilon}(p)$ as well as the integration are being performed properly.

The image currents are obtained from $f_{\epsilon}(p)$. The horizontal component of the image current is equal to $f_1(p)$, while the vertical current is proportional to the derivative of $f_{\epsilon}(p)$. Some plots of the vertical image currents for different values of ϵ_r are given in Figures 3.9 through 3.12. Recall that in impedance calculations the vertical image current need not be calculated since $f_{\epsilon}(p)$ is differentiated a second time, and a substitution can be made for $f_{\epsilon}''(p)$ via the differential Equation (2.45) eliminating all terms containing derivatives of $f_{\epsilon}(p)$.

The next step is the integration to compute the Green's function, $K_{\epsilon}(\theta)$,

$$K_{\epsilon}(|x-x'|) = \int_0^{\infty} f_{\epsilon}(p)G(D) dp \quad (3.5)$$

$$D(p) = \sqrt{(x-x')^2 + \left(2h - \frac{ip}{k\sqrt{\epsilon_r-1}}\right)^2} \quad (3.6)$$

At first glance, it appears the integration to infinity could be the source of some difficulty. When p becomes large enough to dominate $D(p)$ in Equation (3.6), we see that $G(D)$ can be approximated by

$$G(D) = \sqrt{\epsilon_r-1} \frac{e^{-p/\sqrt{\epsilon_r-1}}}{4\pi p}, \quad p \text{ large.} \quad (3.7)$$

Hence, when the approximation (3.7) applies, $G(D)$ decays exponentially. The function $f_{\epsilon}(p)$ also diminishes as p increases. It is apparent that the integration can be truncated after (3.7) is valid and allowed to decay a few time constants.

For ϵ_r of small arguments, $D(p)$ moves through a minimum slightly before $G(D)$ begins to decay, causing a spike in the integrand. This is illustrated in Figures 3.13 through 3.15. As the normalized height, h/λ , of the dipole decreases, the spike tends to increase. However, while the height is greater than zero the spike will remain bounded.

Figures 3.13 through 3.20 are examples of the integrand. The first three are identical to those published by Lindell [14]. The next five plots (Figures 3.16-20) were added to show the effect of a change on the parameters θ , h/λ , $\arg(\epsilon_r)$, and $|\epsilon_r|$. Figure 3.16 shows that an increase in θ moves the peak further from the origin. The corresponding integrands of $K_1(\theta)$ are plotted in Figure 3.17. Note that the peaks in these two figures occur at the same places along the p -axis. As shown in Figure 3.18, the peak in the integrand decreases as h/λ increases. Figure 3.19 shows that the peak is sharp only for small arguments of ϵ_r . As seen in Figure 3.20, increasing the magnitude of ϵ_r also moves the peak further from the origin while smoothing it out at the same time.

It is clear by inspection of Figures 3.13 through 3.20 that the integration producing $K_\epsilon(\theta)$ and $K_1(\theta)$ can be truncated after a certain point, p_0 , with negligible error. In these graphs we see that p_0 varies as θ , h/λ , and ϵ_r change. Therefore, a valid means of detecting the truncation point is needed. One solution to this problem is to test segments of the integrand to determine whether that part of the integrand is more or less than, for example, 0.01% of the integration to that point. This method was used with the adaptive integration routine mentioned earlier and found to be very effective.

Another means of predicting a good truncation point was derived by equating the magnitudes of two approximations for $D(p)$, $|D(\text{small } p)|$ and $|D(\text{large } p)|$. This leads to

$$|\sqrt{\theta^2 + k^2 h^2}| = |kh - jp_1 / \sqrt{\epsilon_r - 1}|. \quad (3.8)$$

As a result, the p satisfying (3.8) should be in the region slightly before $G(D)$ decays exponentially. It can be approximated by

$$p_1 \cong |\sqrt{\epsilon_r - 1}| (8kh + \theta). \quad (3.9)$$

If we allow $G(D)$ to decay a few attenuation constants beyond p_1 and add 10 to it as an extra precaution, we should be able to truncate the integration when

$$p = |\sqrt{\epsilon_r - 1}| (8kh + \theta + 3) + 10. \quad (3.10)$$

Using (3.10) in place of infinity as a limit of integration proved to give good results. In fact, Figures 3.13 through 3.20 were all generated using the aforementioned adaptive trapezoidal routine with (3.10) as an endpoint. Note that the plots are all relatively smooth, even in the region of the spike (Fig. 3.15), and in each case the integrand had become small enough before truncation that it could no longer be read on the graph.

Equation (3.10) indicates that as $|\epsilon_r|$, h , or θ become large the integral for the Green's function, $K_\epsilon(\theta)$, takes longer to compute. Thus, direct computation of impedances using Equation (2.51) becomes impractical when p_1 is large. In the case of large h , Equation (2.63) can be used. No asymptotic approximations were derived for large $|\epsilon_r|$ or large θ . It is the opinion of the author that $K_\epsilon(\theta)$ can be represented by an infinite summation much as $f_\epsilon(p)$ was. Similar integrals were found in [20] and [21]. Unfortunately, no solution for integrals of form identical to $K_\epsilon(\theta)$ could be found.

Table 3.1. Percent error of adaptive trapezoidal integration routine when applied to the integral identities in Equations (3.3) and (3.4).

REAL EPSILON	IMAGINARY EPSILON	% ERROR EQ. 3.3	% ERROR EQ. 3.4
2	0	0.0656	0.1168
10	0	0.1048	0.0012
20	0	0.0835	0.0009
50	0	0.0758	0.0013
2	-0.5	0.2832	0.0009
10	-2.5	0.0296	0.0012
20	-5	0.0560	0.0009
50	-12.5	0.0732	0.0013
2	-1	0.2464	0.0006
10	-5	0.1117	0.0012
20	-10	0.0606	0.0009
50	-25	0.0647	0.0012
2	-2	0.1578	0.0009
10	-10	0.0366	0.0012
20	-20	0.0648	0.0011
50	-50	0.0705	0.0012
2	-4	0.0547	0.0018
10	-20	0.0515	0.0010
20	-40	0.0578	0.0013
50	-100	0.0183	0.0012
2	-10	0.0308	0.0014
10	-50	0.0166	0.0012
20	-100	0.0089	0.0013
50	-250	0.0074	0.0008

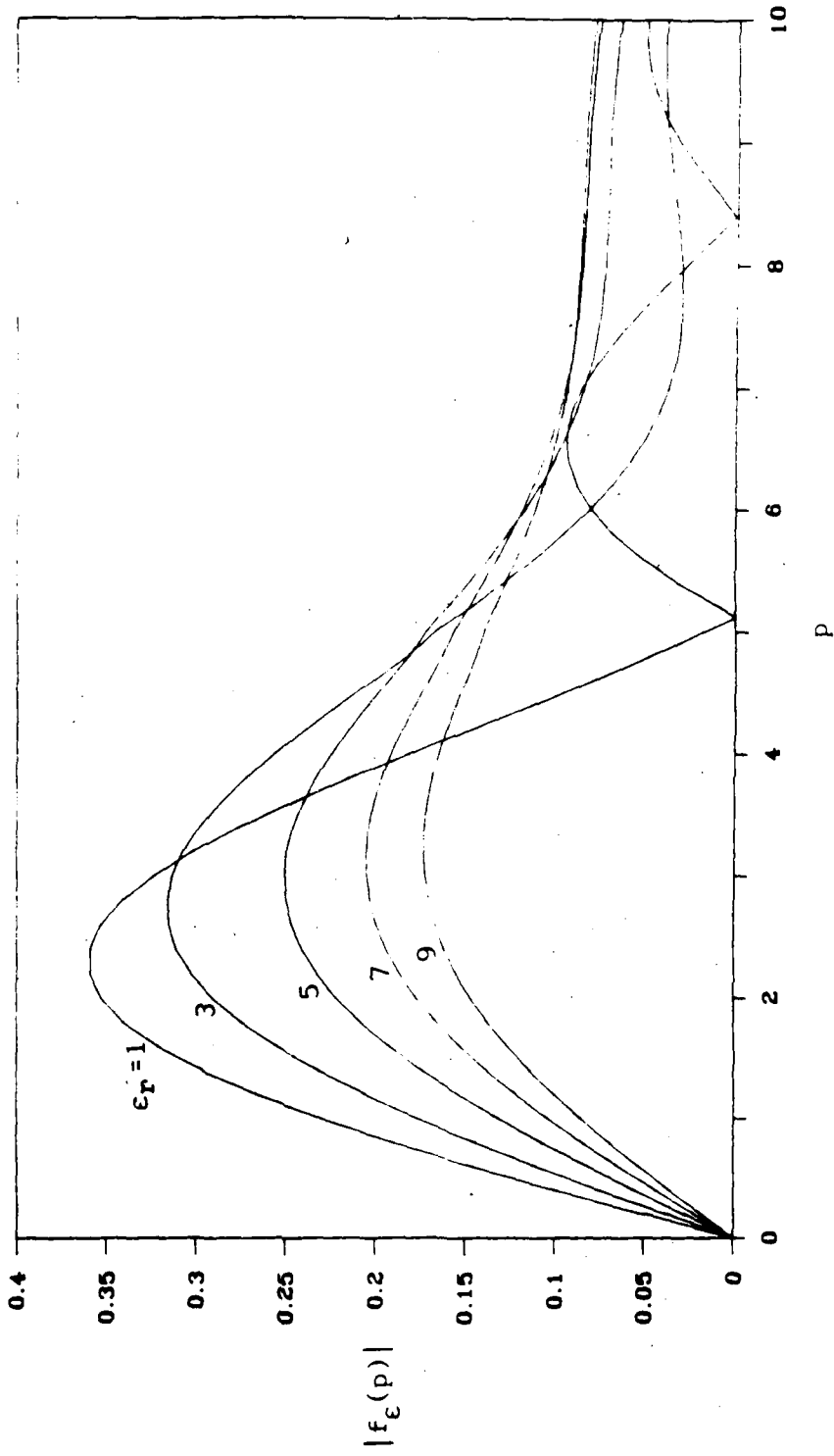


Figure 3.1. $|f_\epsilon(p)|$ for different ϵ_r . In this plot and in those following, p is the positive real variable defined in Equation (2.34). Note the decrease in the peak as ϵ_r increases.

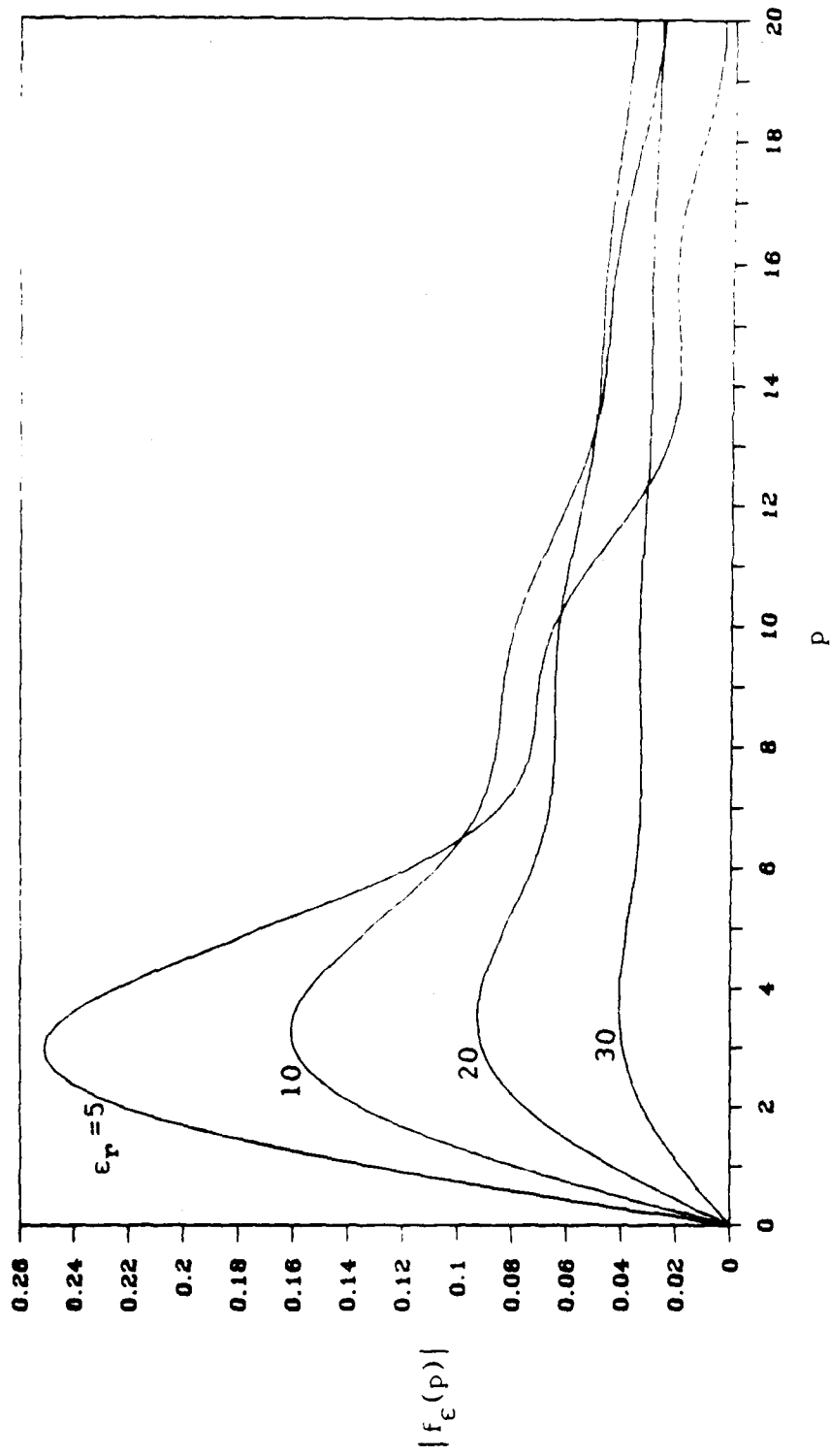
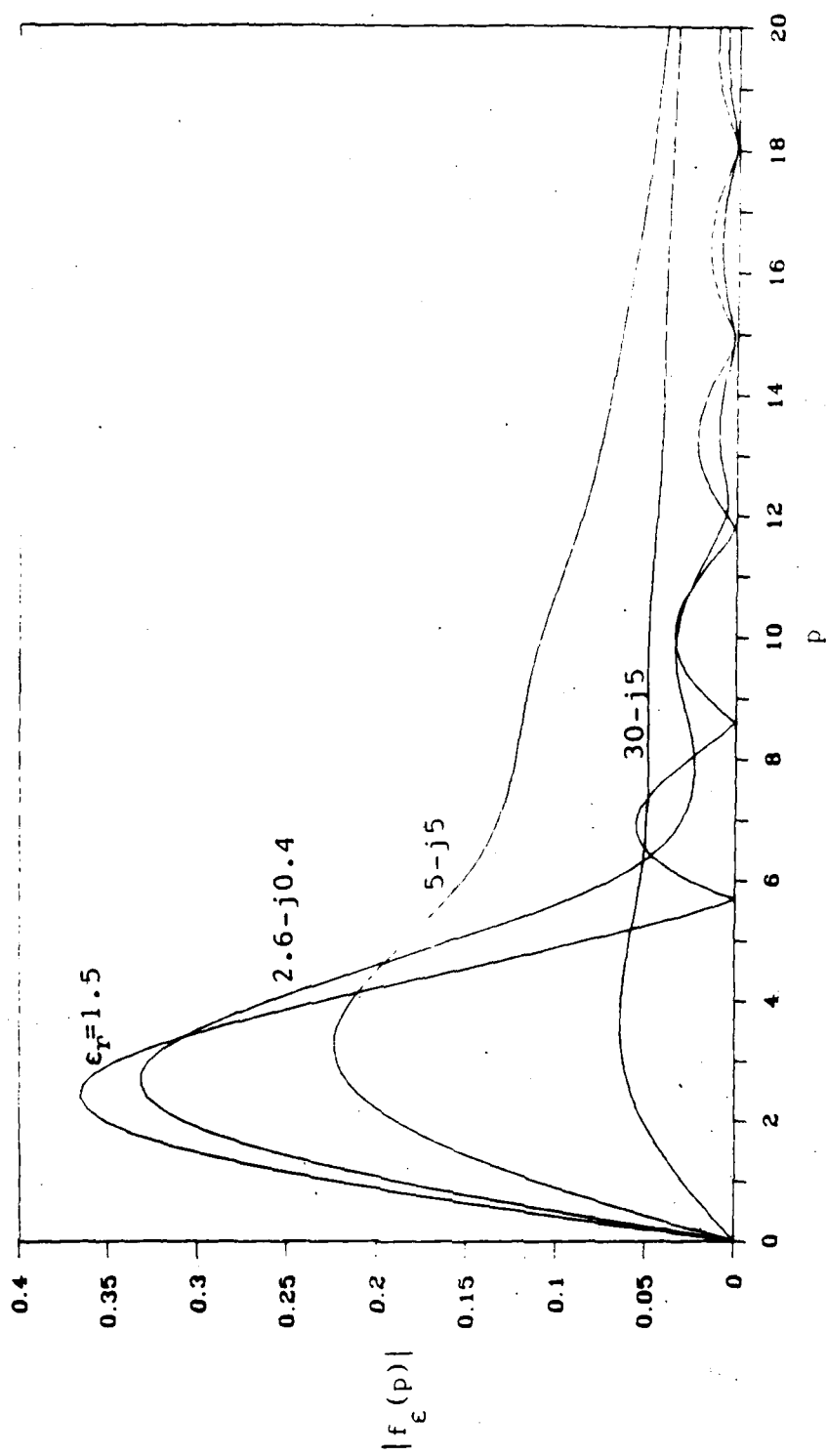
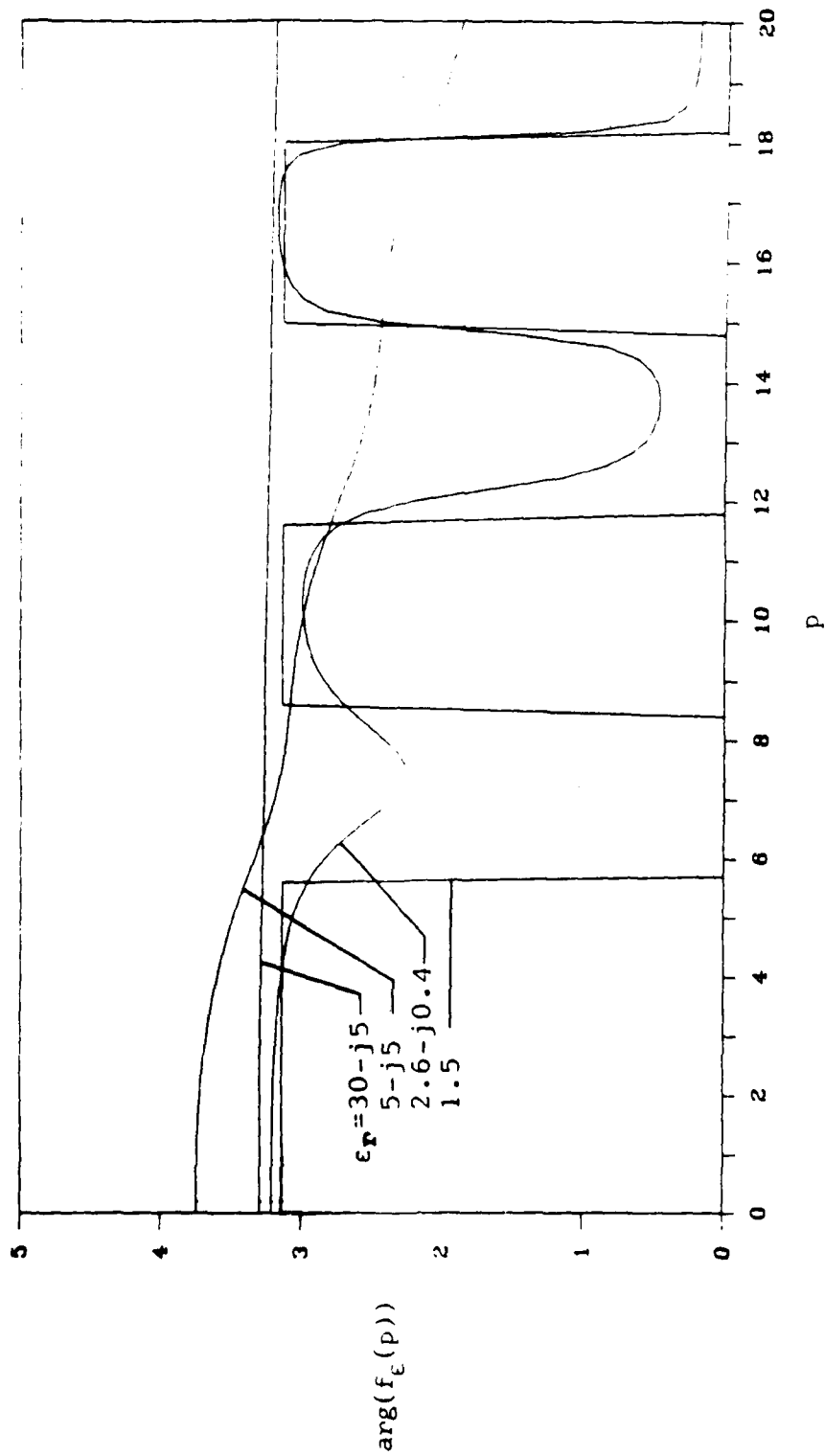


Figure 3.2. $|f_\epsilon(p)|$ for different ϵ_r . Note that for ϵ_r large the downward slope in $|f_\epsilon(p)|$ is very small.

Figure 3.3. $|f_\epsilon(p)|$ for different ϵ_r .

Figure 3.4. Argument of $f_\epsilon(p)$ for different ϵ_r .

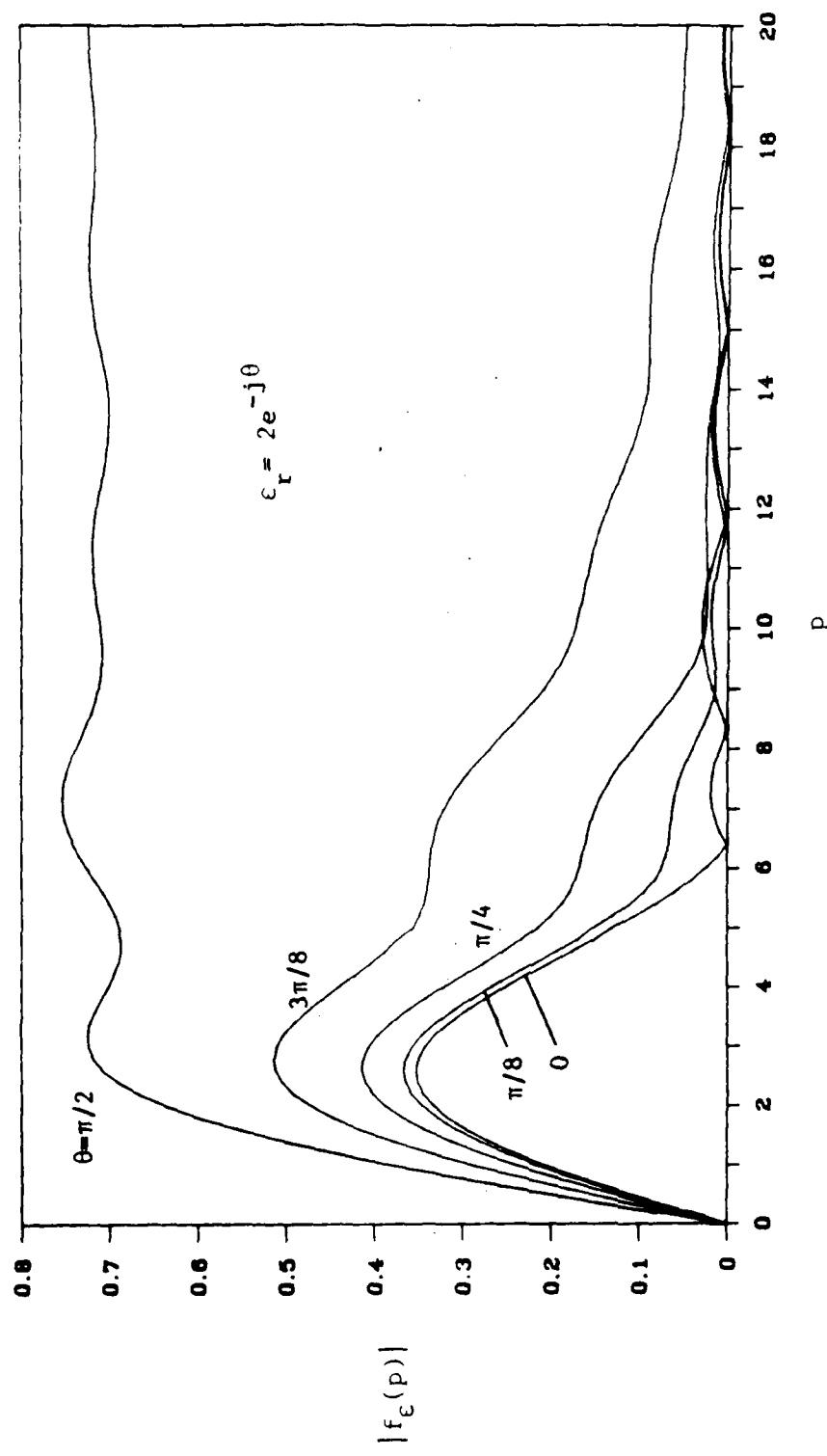


Figure 3.5. $|f_\epsilon(p)|$ for different arguments of ϵ_r .

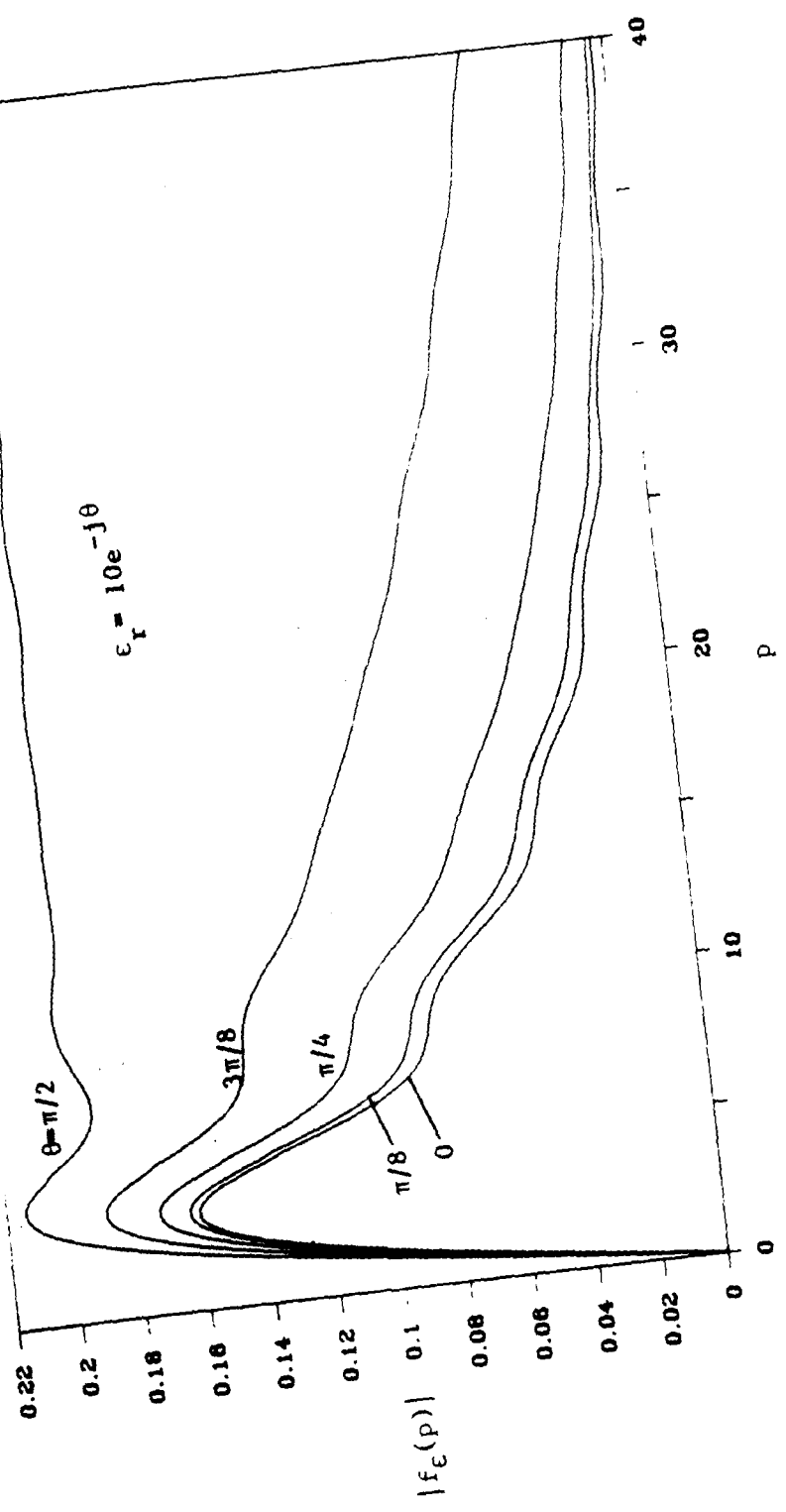


Figure 3.6. $|f_\epsilon(p)|$ for different arguments of ϵ_r .

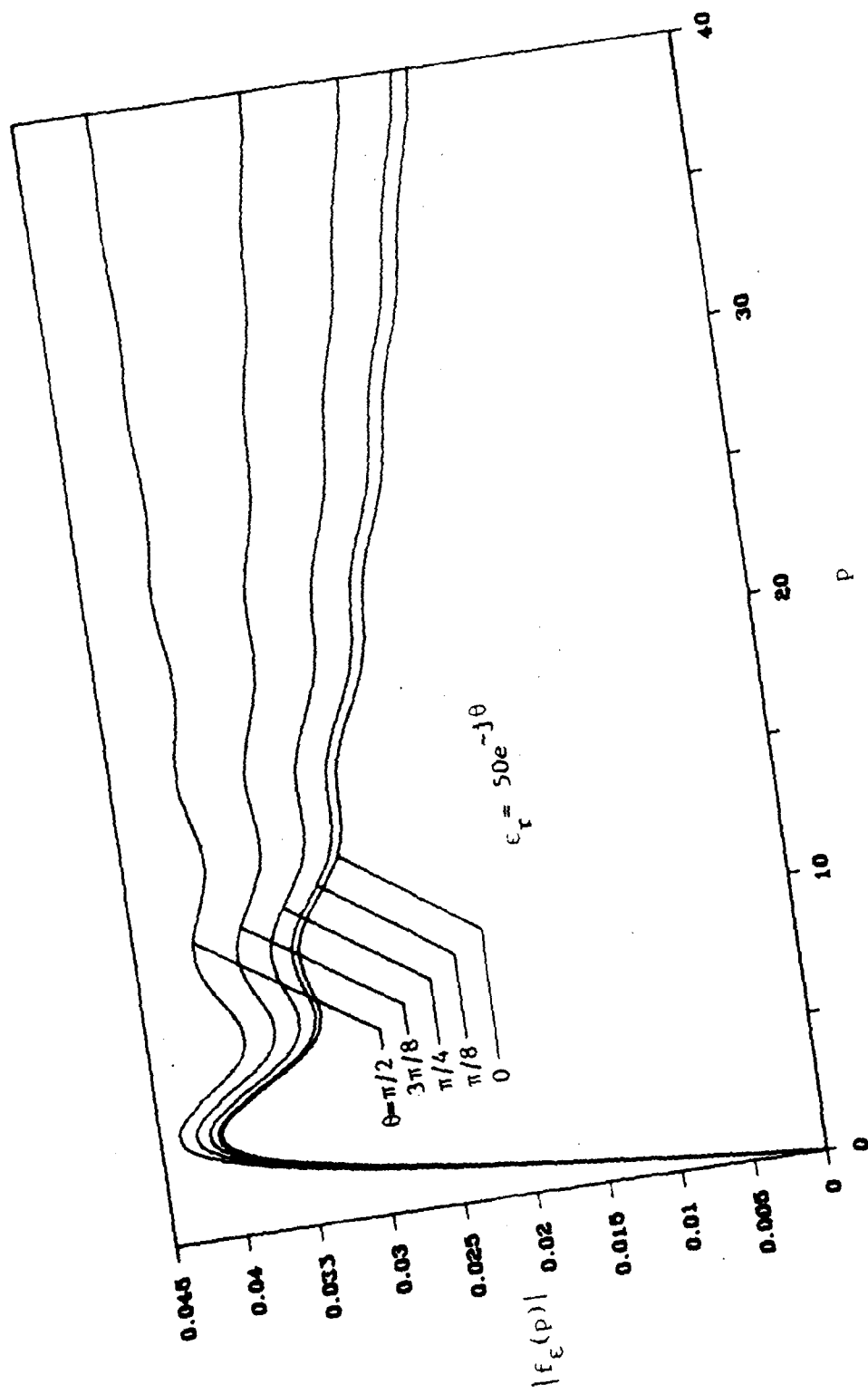


Figure 3.7. $|f_\epsilon(p)|$ for different arguments of ϵ_r .

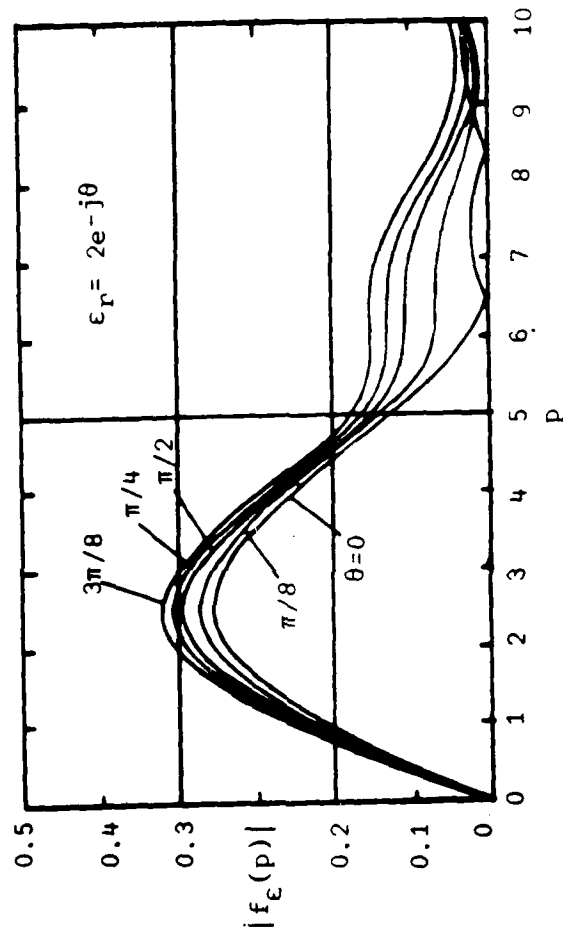


Figure 3.8. $|f_\epsilon(p)|$ for different arguments of ϵ_r . (Source: I. V. Lindell, E. Alanen, and K. Mannersalo, "Exact image method for impedance computation of antennas above the ground," *IEEE Trans. Antennas Propag.*, vol AP-33, no. 9 [September 1985]. Used with permission.)

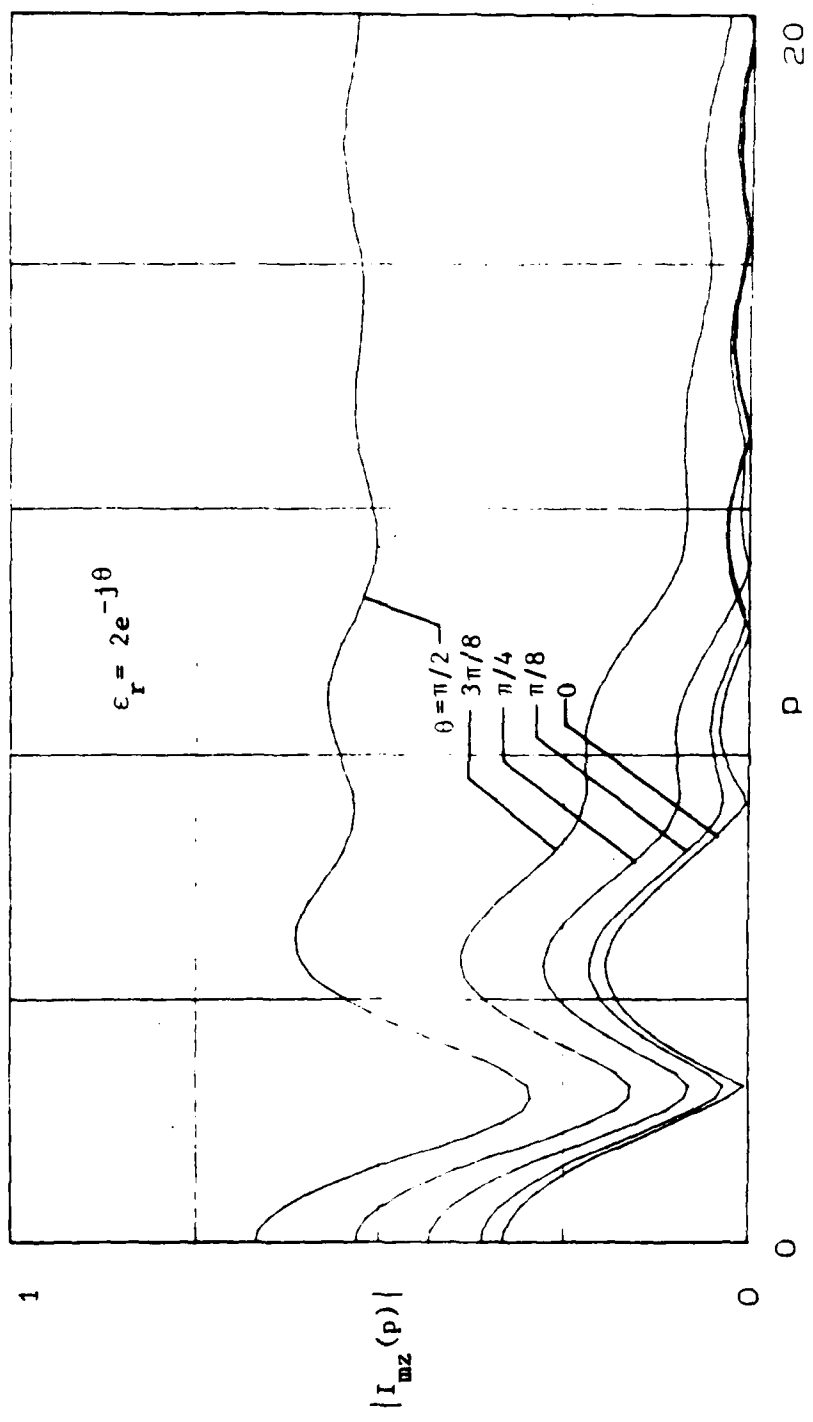


Figure 3.9. Magnitude of vertical image current for different values of ϵ_r .

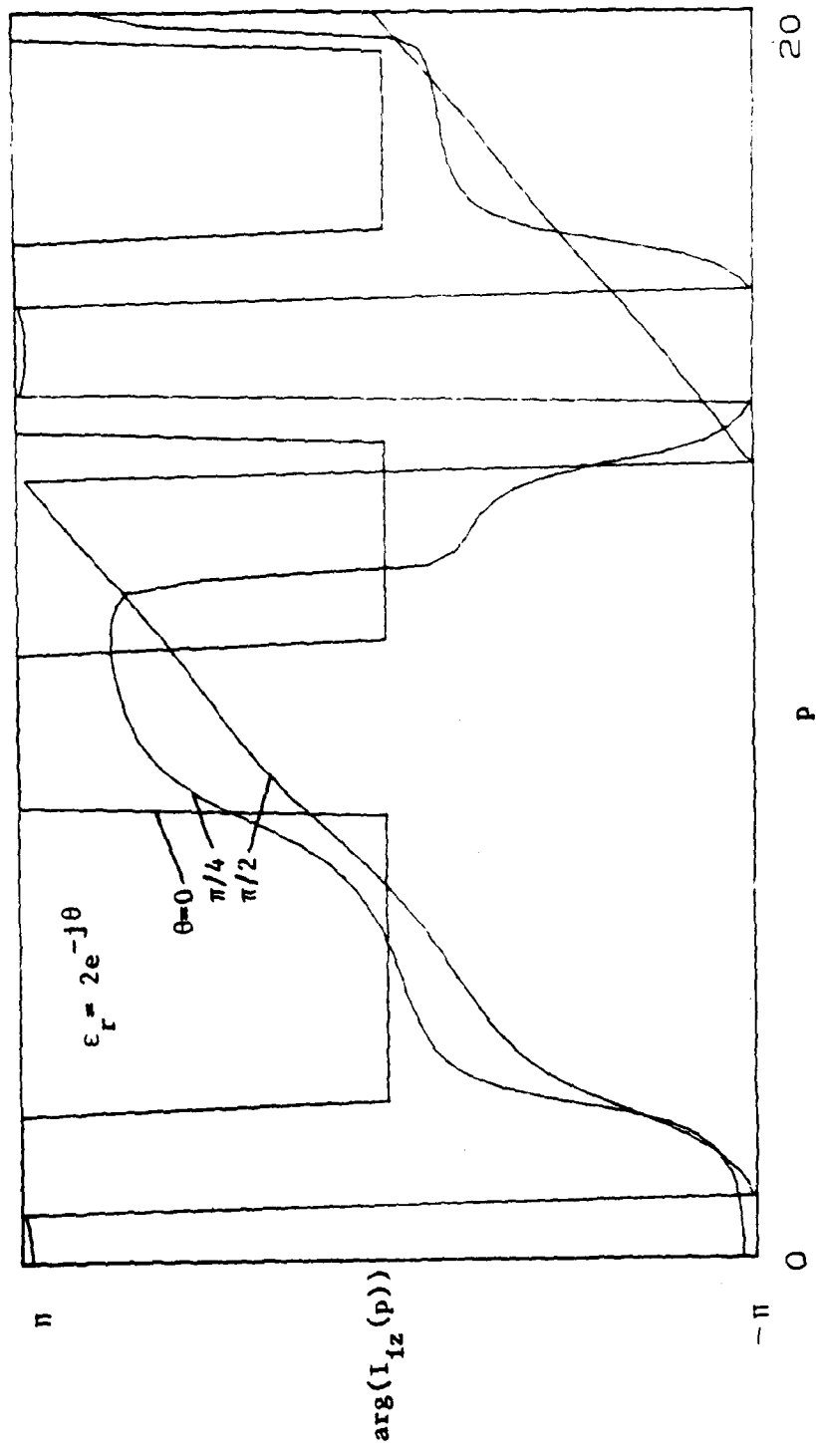


Figure 3.10. Argument of vertical image current for different values of ϵ_r .

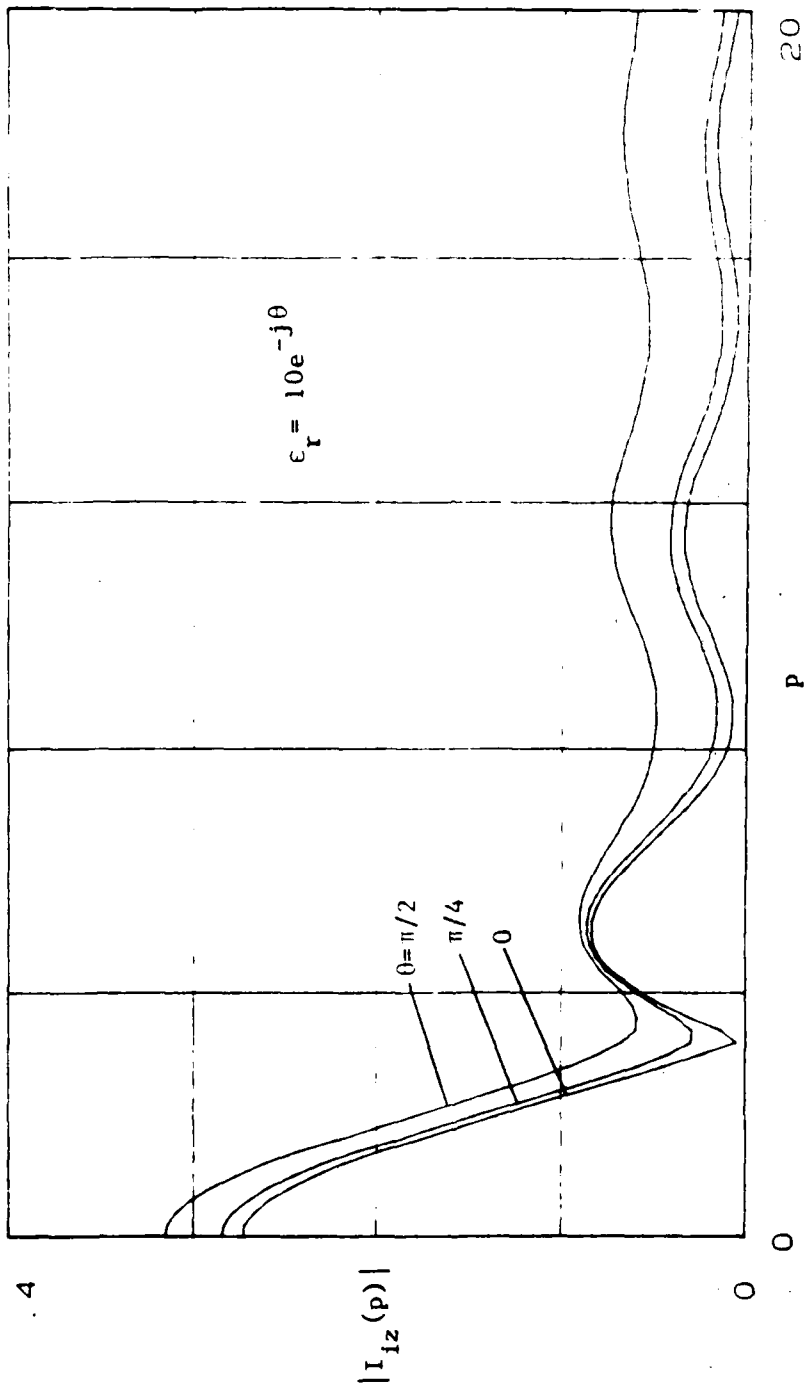


Figure 3.11. Magnitude of vertical image current for different values of ϵ_r .

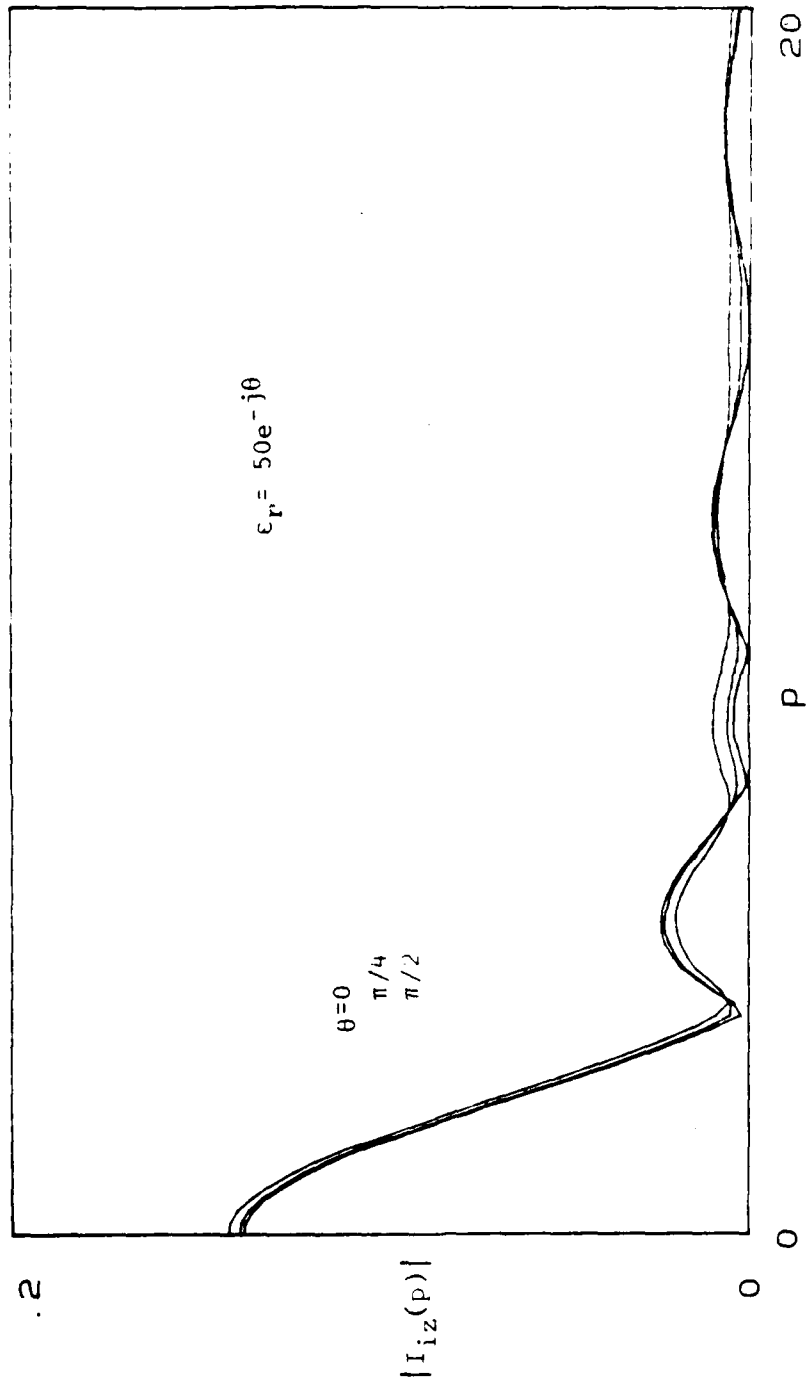


Figure 3.12. Magnitude of vertical image current for different values of ϵ_r .

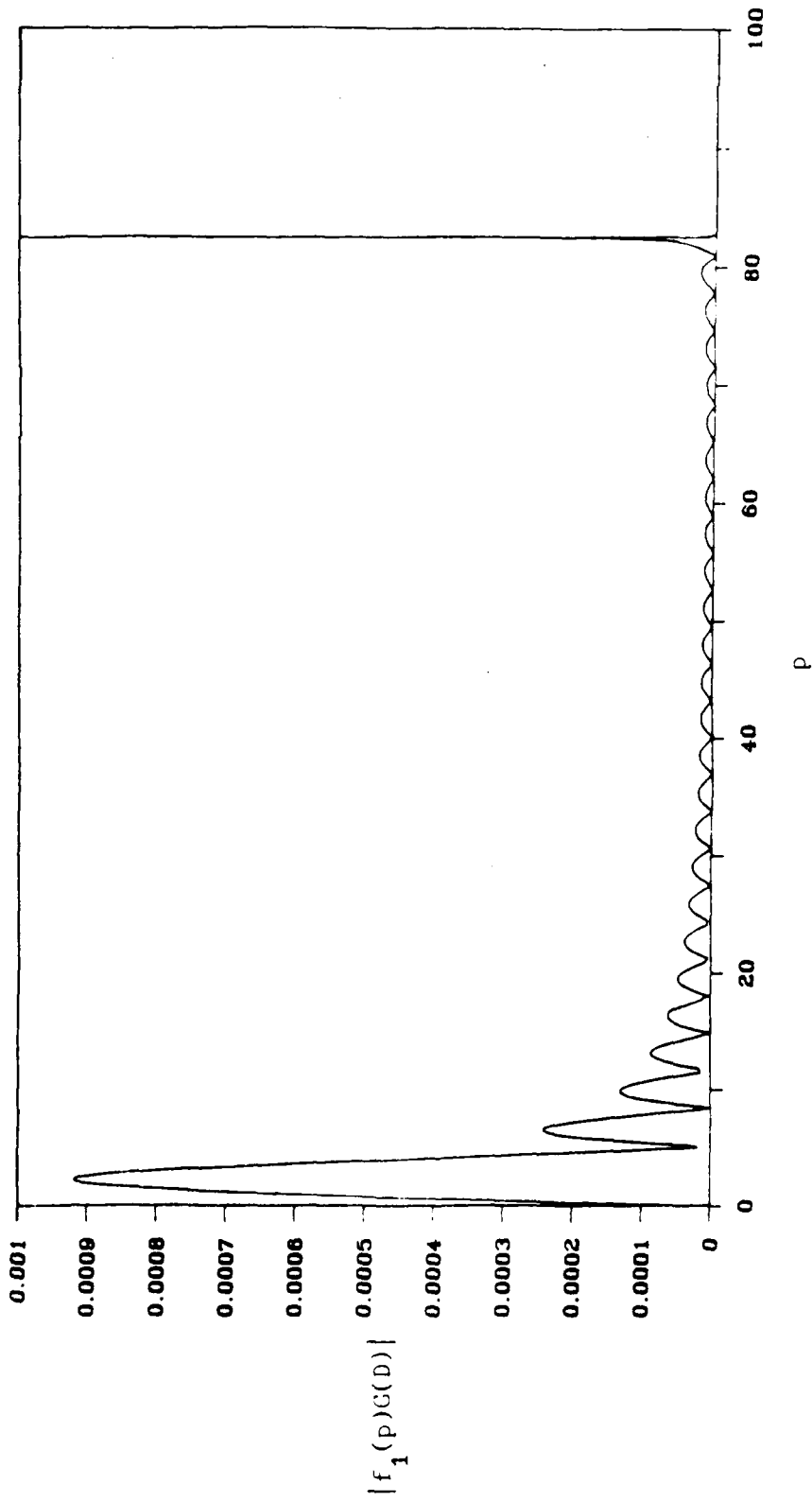


Figure 3.13. Magnitude of the integrand of $K_1(\theta)$ when $\theta = 31.14$, $\epsilon_1 = 8$, and $kh = 0.00001$

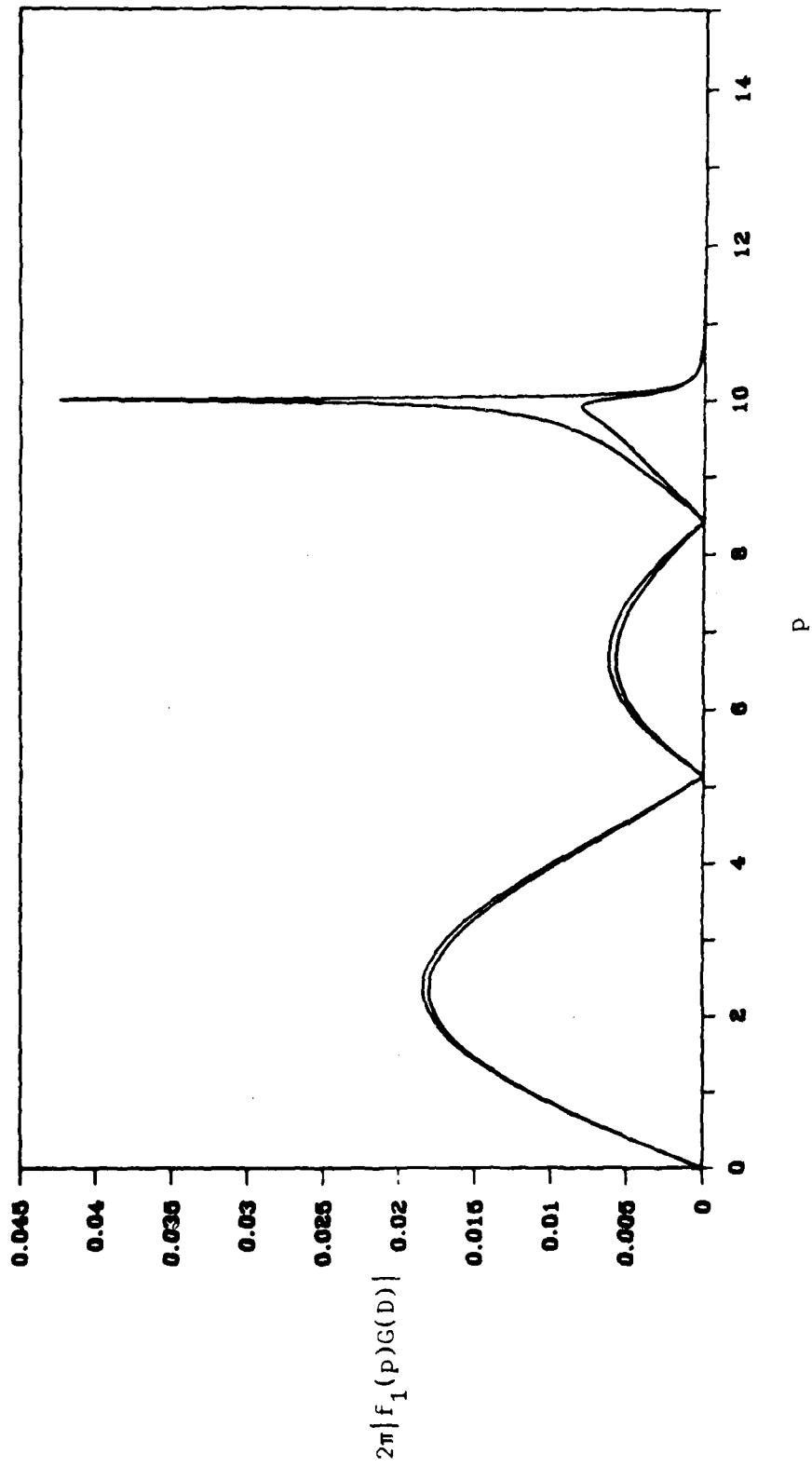


Figure 3.14. Magnitude of the integrand of $K_1(\theta)$ with $\theta = 10$, $\epsilon_r = 2$, and two different heights $kh = 0.01$ and $kh = 0.1$.

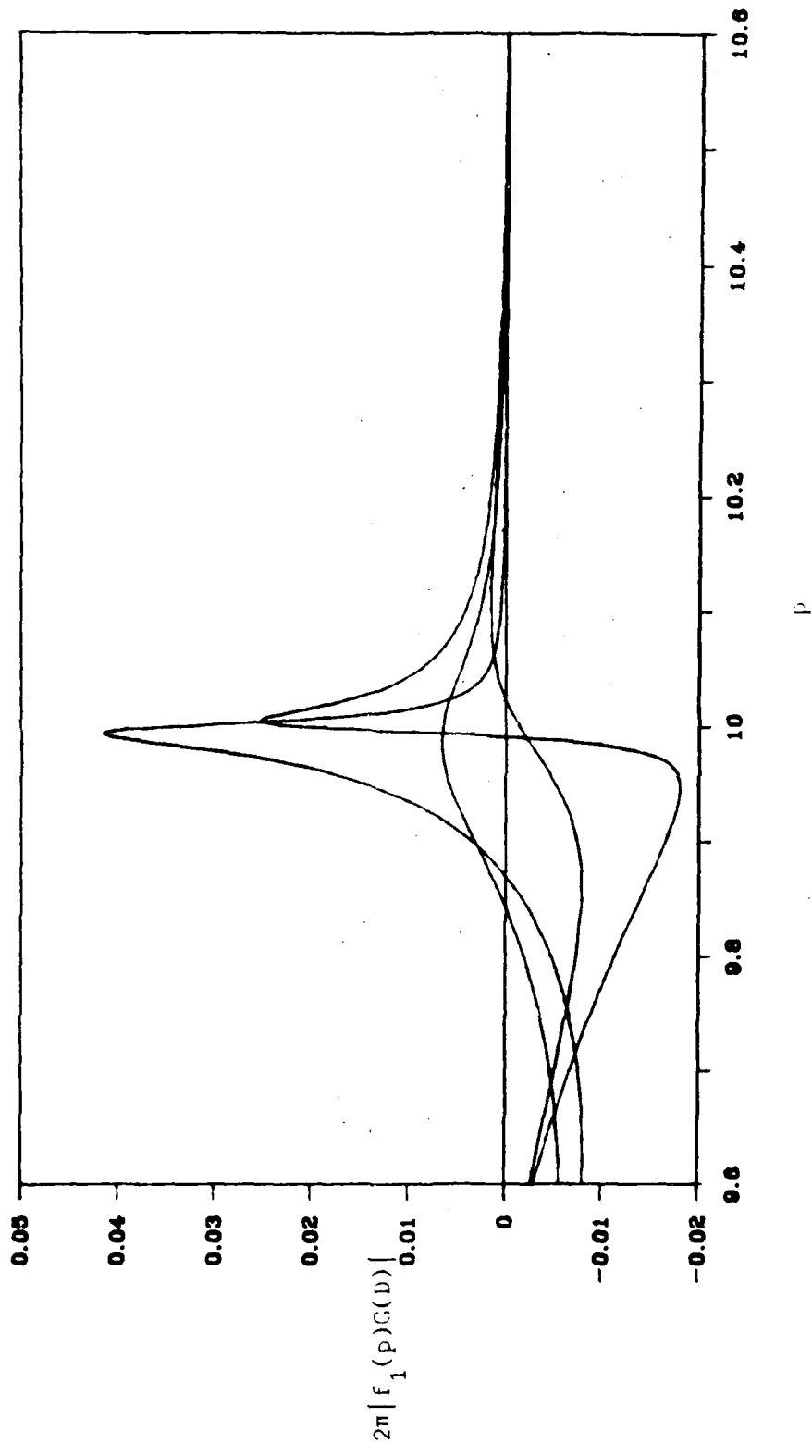


Figure 3.15. Real and imaginary parts of integrands in Figure 3.14 near the peak.

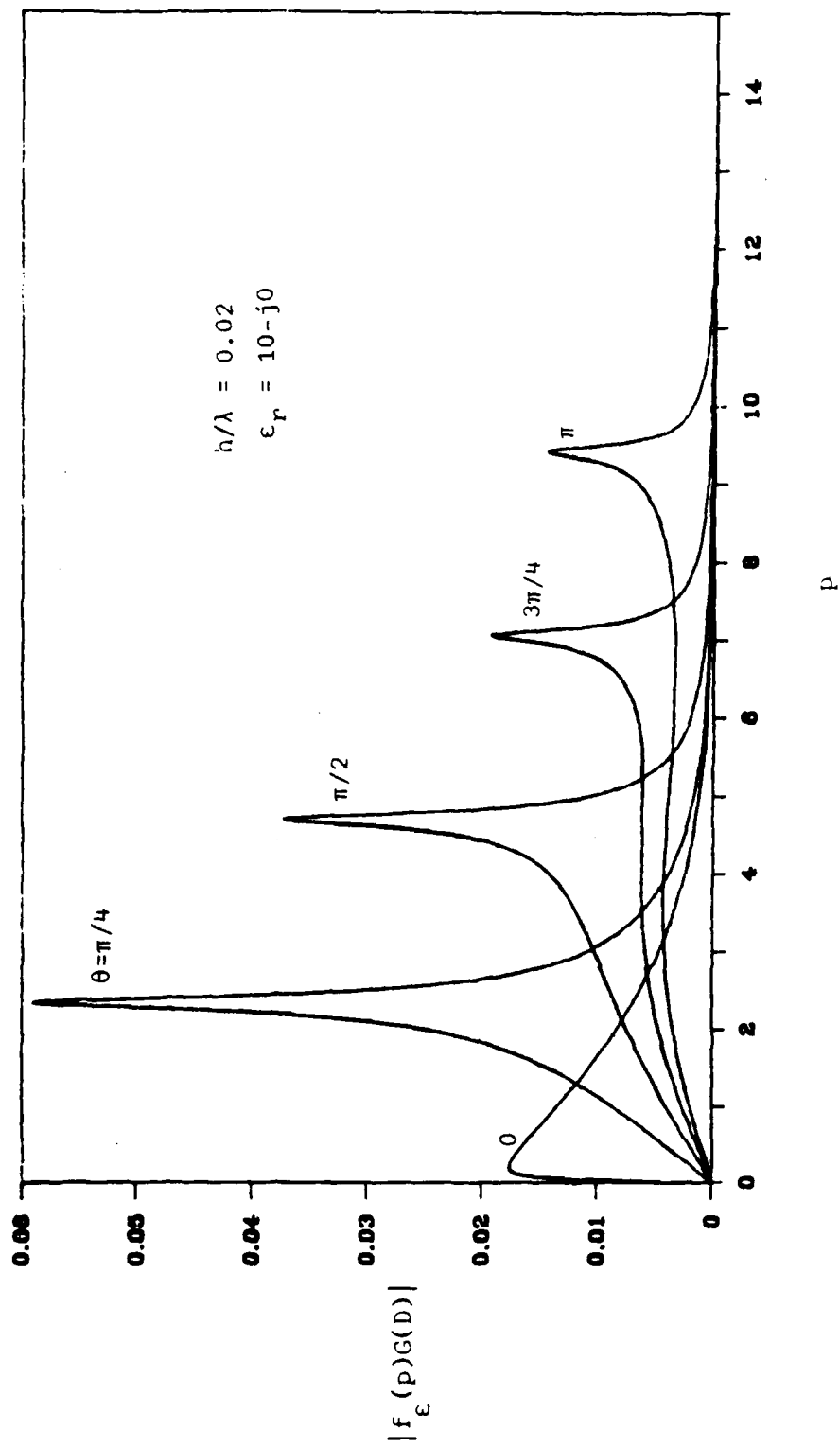


Figure 3.16. Magnitude of integrand of $K_\epsilon(\theta)$ for different θ , with $h/\lambda = 0.02$, $\epsilon_r = 10-j0$.

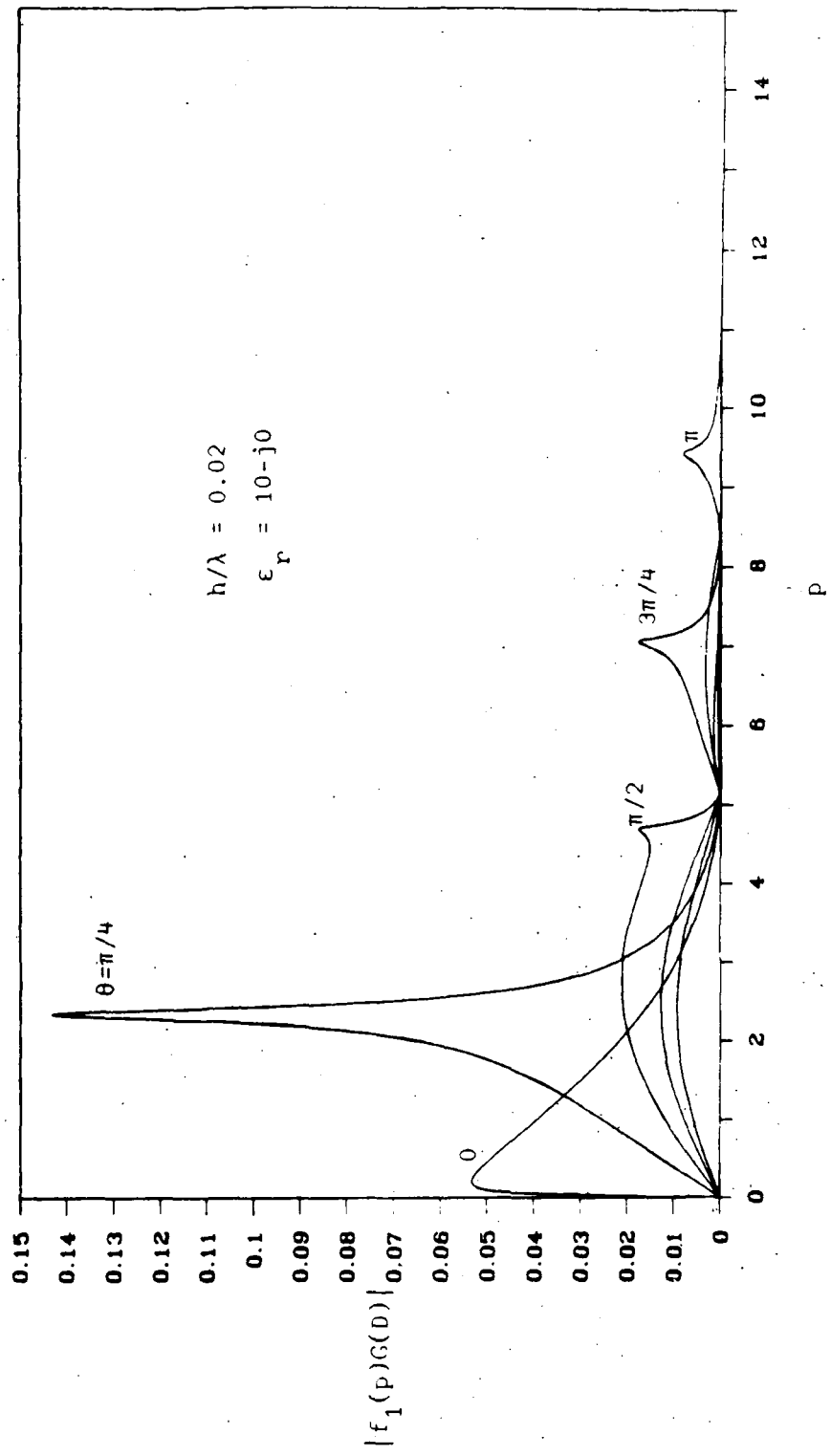


Figure 3.17. Magnitude of integrand of $K_1(\theta)$ for different θ , with $h/\lambda = 0.02$, $\epsilon_r = 10-j0$.

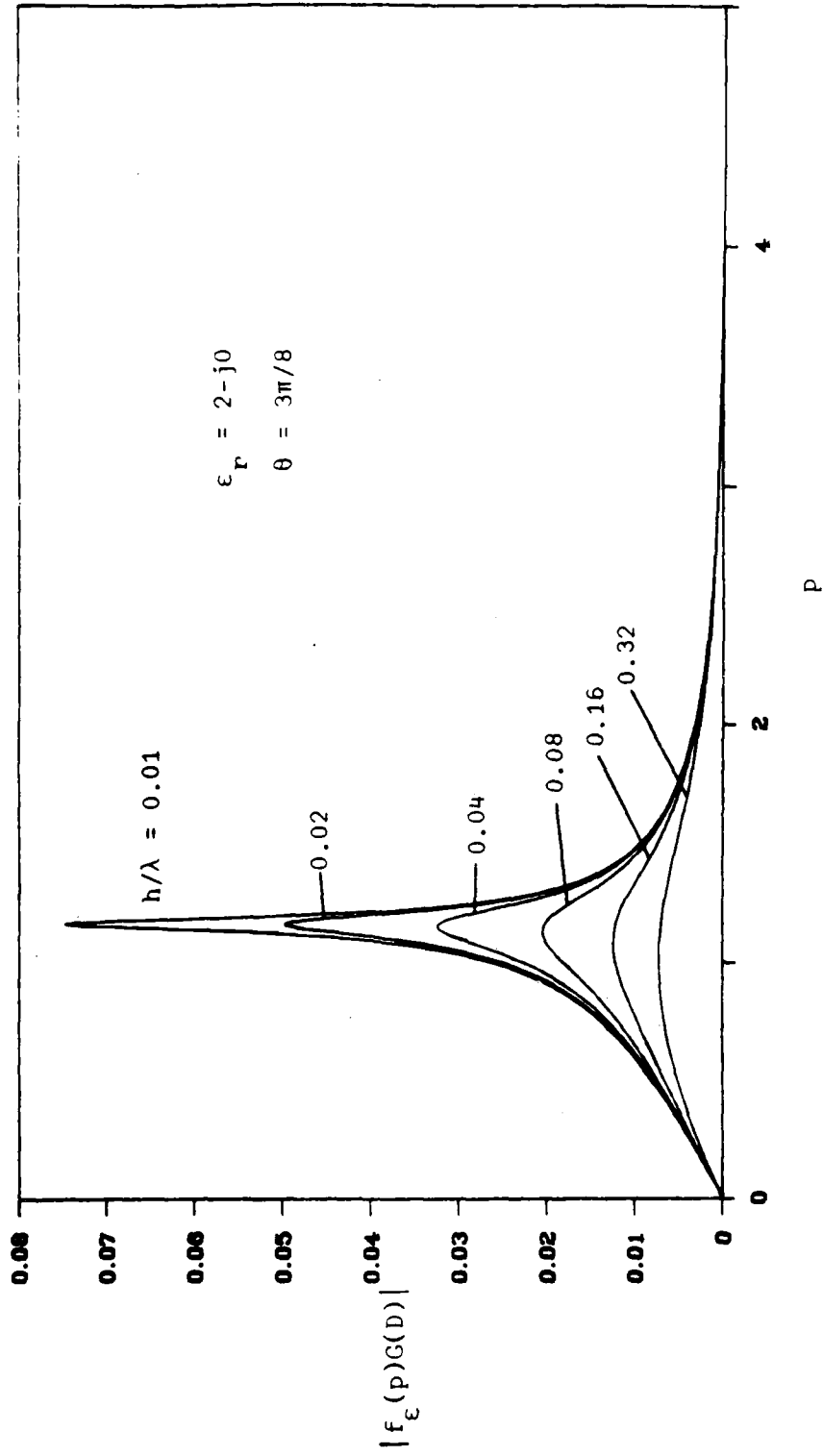


Figure 3.18. Magnitude of integrand of $K_\epsilon(\theta)$ for different h/λ , with $\epsilon_r = 2-j0$ and $\theta = 3\pi/8$.

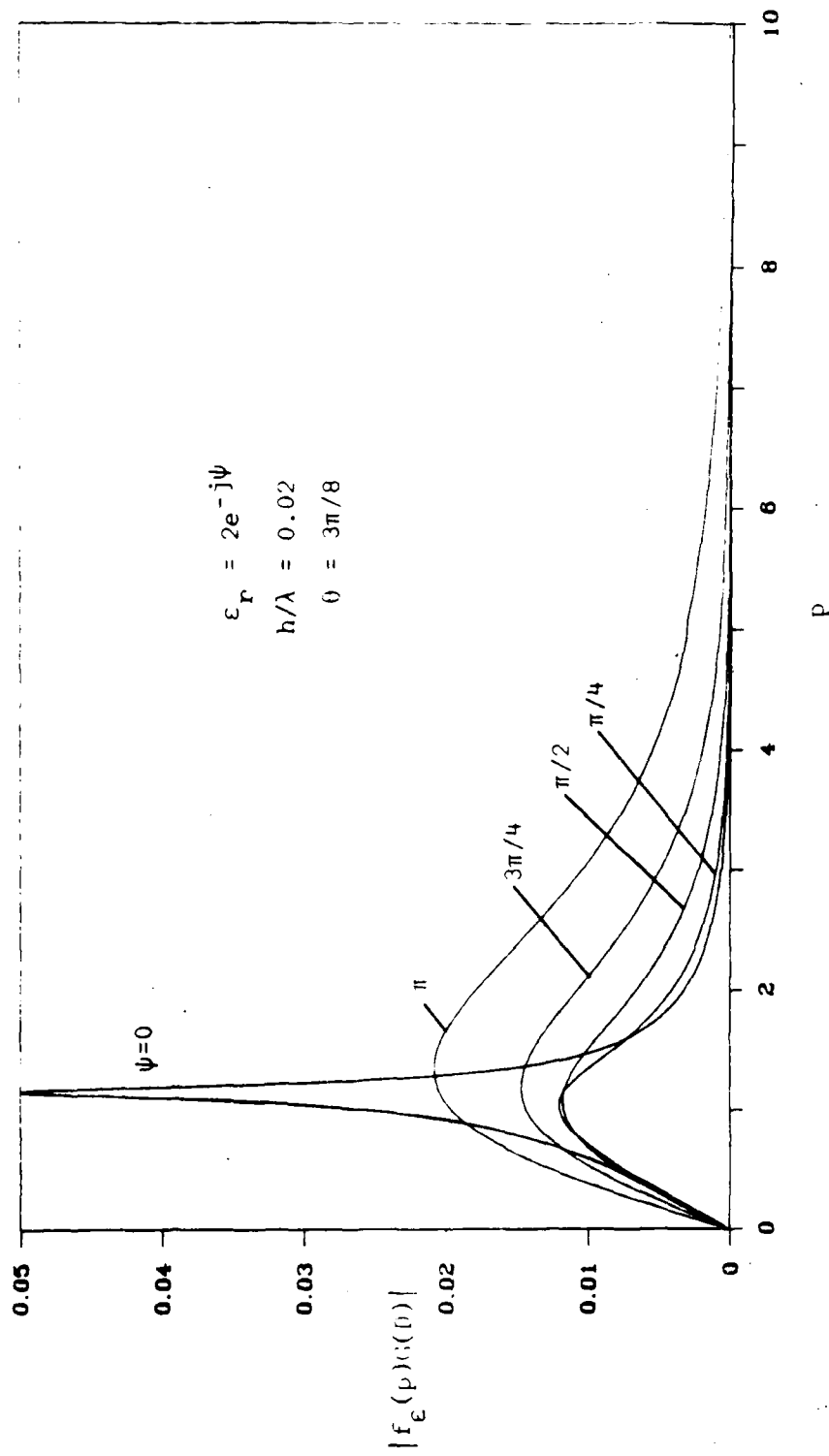


Figure 3.19. Magnitude of integrand of $K_\epsilon(\theta)$ for different $\arg(\epsilon_r)$, with $|\epsilon_r| = 2$, $\theta = 3\pi/8$, and $h/\lambda = 0.02$.

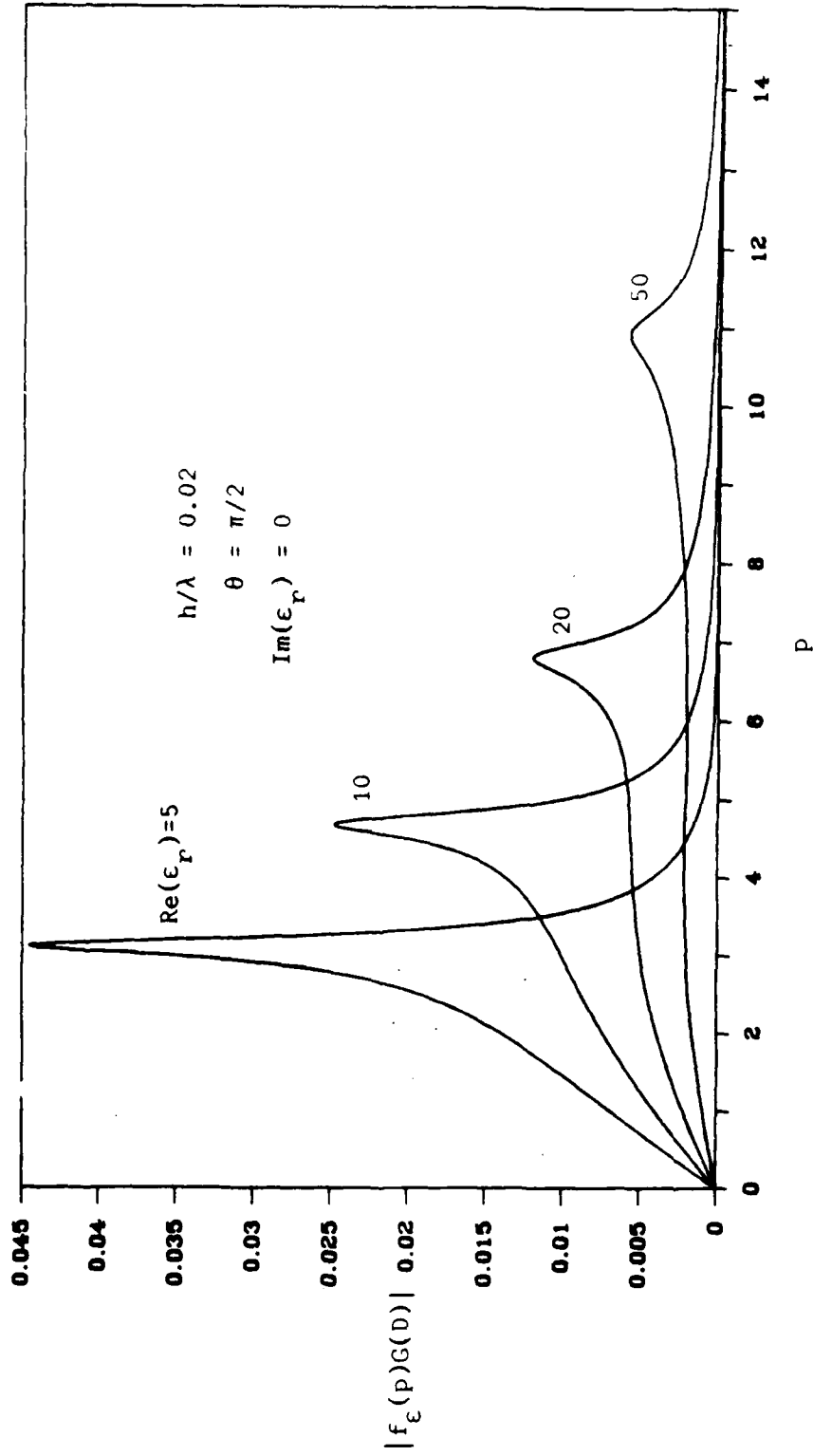


Figure 3.20. Magnitude of integrand of $K_\epsilon(\theta)$ for different $|\epsilon_r|$, with $\arg(\epsilon_r) = 0$, $\theta = 3\pi/8$, and $h/\lambda = 0.02$.

4. IMPEDANCE CHARACTERISTICS

This Chapter discusses dipole impedance characteristics. Because the case of the half-wave dipole is often discussed in the literature, it will be considered first. Equation (2.58) is used to compute the effect of the ground. This is added to the thin-wire free-space input impedance, $73.1 + j42.5$ ohms. The integration in Equation (2.58) is performed using the same adaptive trapezoidal routine as was used in the calculations of the preceding chapter.

Figures 4.1 through 4.4 were generated to be compared with results already published in [22], [23], and [16], respectively. The resistances compare well with those published. The reactance, on the other hand, does not agree with that documented by Lindell [16]. The reason for this is not known. As one would expect, these figures show that the ground has more of an effect on the input impedance of antennas at lower heights. Note also that there are nodes at heights slightly before integer multiples of a quarter-wavelength. Hence, heights of $\lambda/8$ or less will result in the largest change in impedance and thus will yield the highest resolution when measuring permittivity.

As a study of the accuracy of the approximate impedance given in Equation (2.63), Figures 4.5 through 4.7 were generated. Each figure shows the real and imaginary parts of the input impedances calculated using both Equations (2.60) and (2.63). The RCM (reflection coefficient method) gives accurate impedances at larger heights. As the relative height, h/λ , of the dipole decreases, the RCM impedance becomes less accurate, until at low heights, it no longer even resembles the correct input impedance. Although the RCM approximation may be useful in many applications, it is clear that it is not appropriate for use in determining ground permittivity since the approximation seems to be valid only when the impedance is least affected by the permittivity.

Calculations were made using Equation (2.59). The results were plotted as the ratio of change in impedance to free-space input impedance as a function of $2kH$ in Figures 4.8 through 4.15. The first four contrast impedances for different heights, while the last four show the effect of changing ϵ_r . In the plots, $2kH = \pi$ corresponds to a half-wave dipole and $2kH = 2\pi$ to a full-wave dipole. The free-space values were determined using the theoretical expression given in [24]. The first four of these figures reinforce the idea that the impedance change in general increases as the height decreases for antennas of any length. Notice that as the dipole approaches a wave length, $\Delta R/R$ and $\Delta X/X$ tend toward zero. Also, the ratio of the imaginary parts approaches zero when $2kH$ is small. When the relative changes in input impedances are zero regardless of ground permittivity, it is difficult to infer a permittivity. Therefore, it would be best to use dipoles with $2H \leq 3\lambda/4$. In the case of short dipoles, the effect of the half space can only be seen in the real part of the impedance. This allows only one degree of freedom to determine both the real and imaginary parts of the permittivity. It would be best to use antenna lengths that show variations in both the real and imaginary parts of the impedance. Therefore, to obtain good resolution between the input impedance and complex permittivity, the length of the dipole should be in the region $\lambda/4 \leq 2H \leq 3\lambda/4$.

The next five figures, 4.16 through 4.20, are contour maps showing the relationship between ground permittivity and input impedance at different heights above the ground. After a quick inspection of these figures, one can see that the contours are larger at lower heights. They are all well behaved. Once the input impedance is known, the complex permittivity can be easily determined using a contour similar to those shown here. Only at the lower heights does the contour begin to fold onto itself. If a measurement falls into this region, another measurement can be taken at some other height or frequency to isolate the correct permittivity.

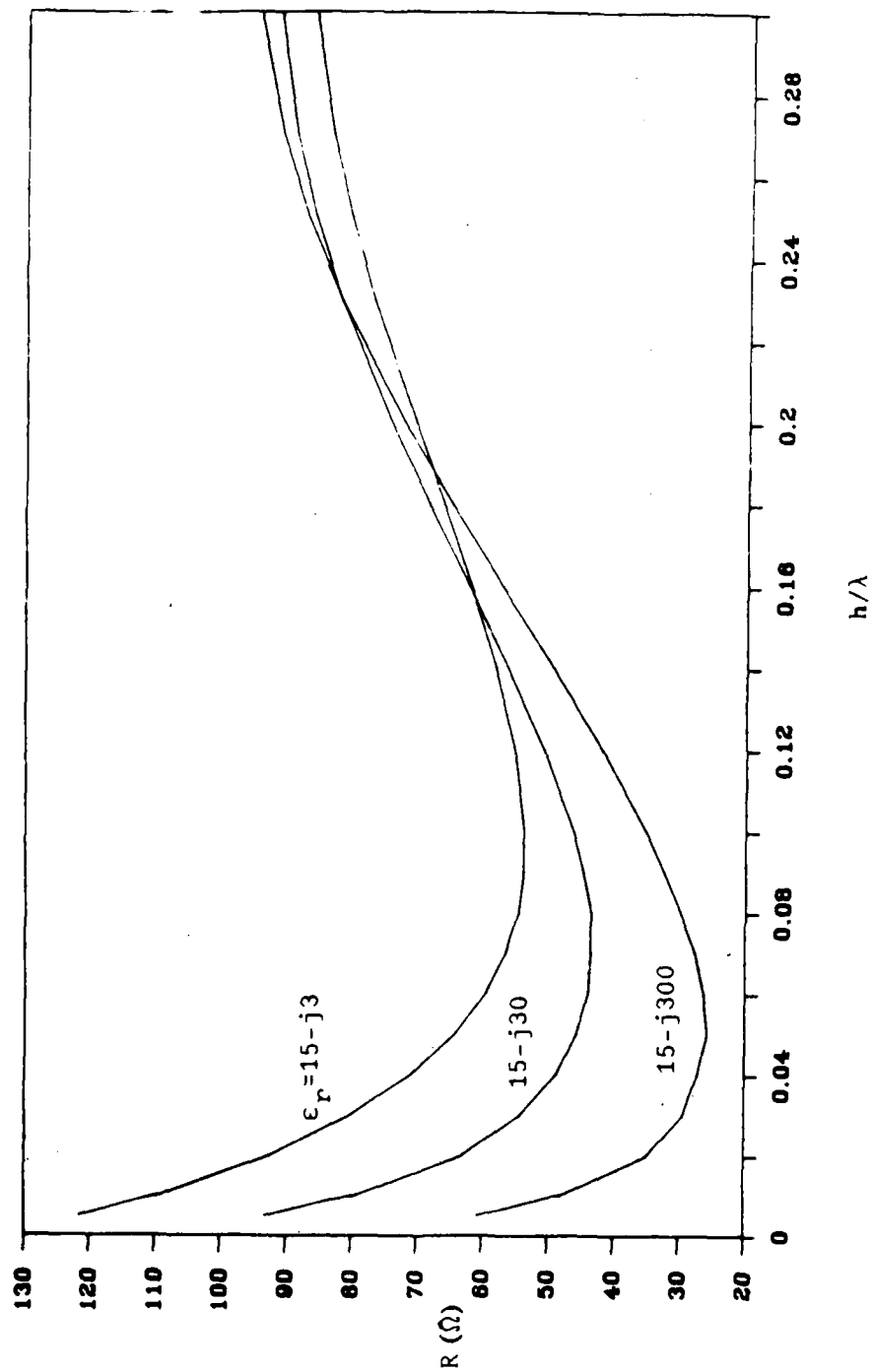


Figure 4.1. Input resistance (R) of half-wave dipole as a function of relative height (h/λ) above various grounds. This compares well with graphs published by Miller [22].

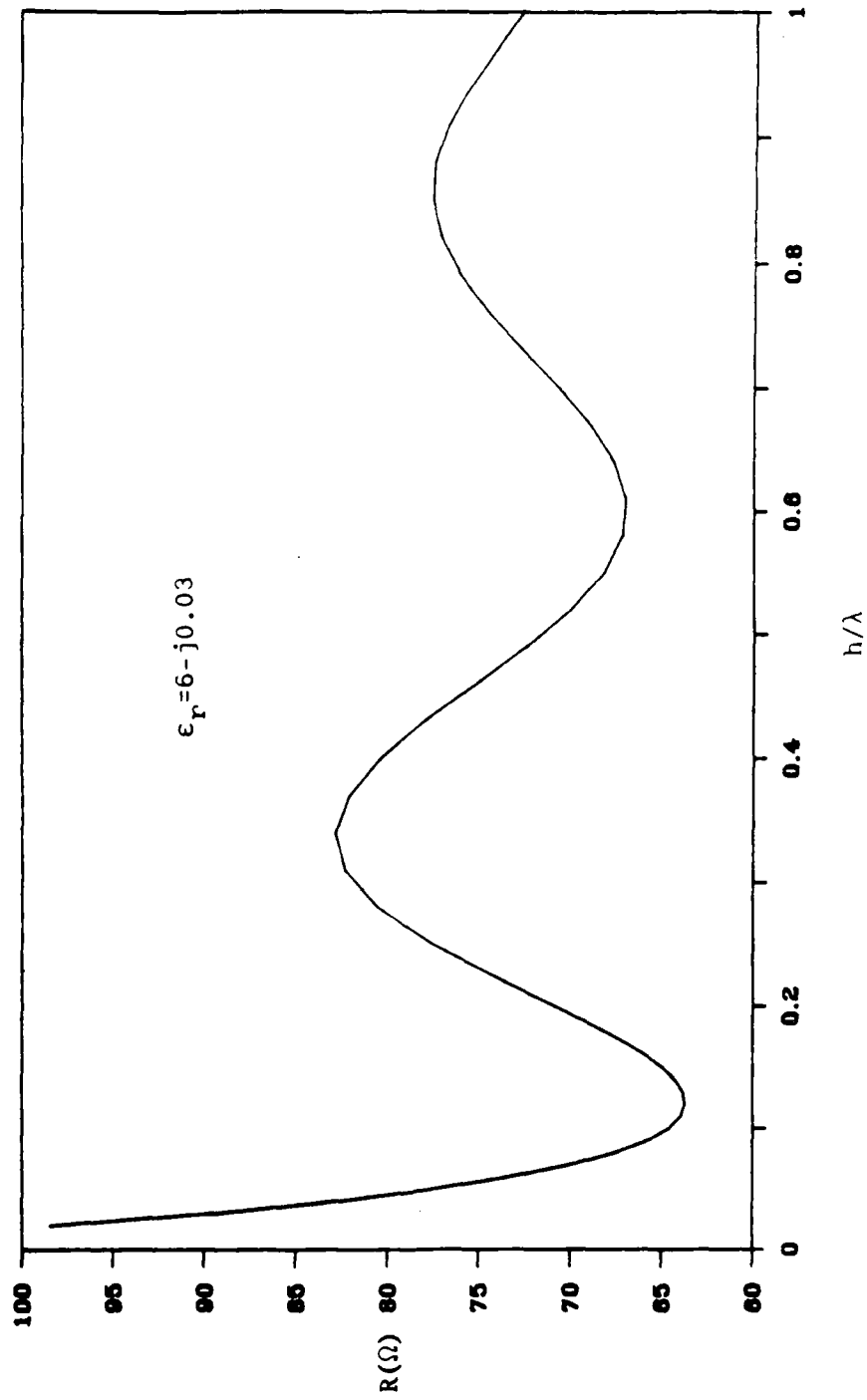


Figure 4.2. Input resistance (R) of half-wave dipole as a function of relative height (h/λ) above a ground with $\epsilon_r = 6 - j0.03$. This compares well with graphs published by Lindell [23].

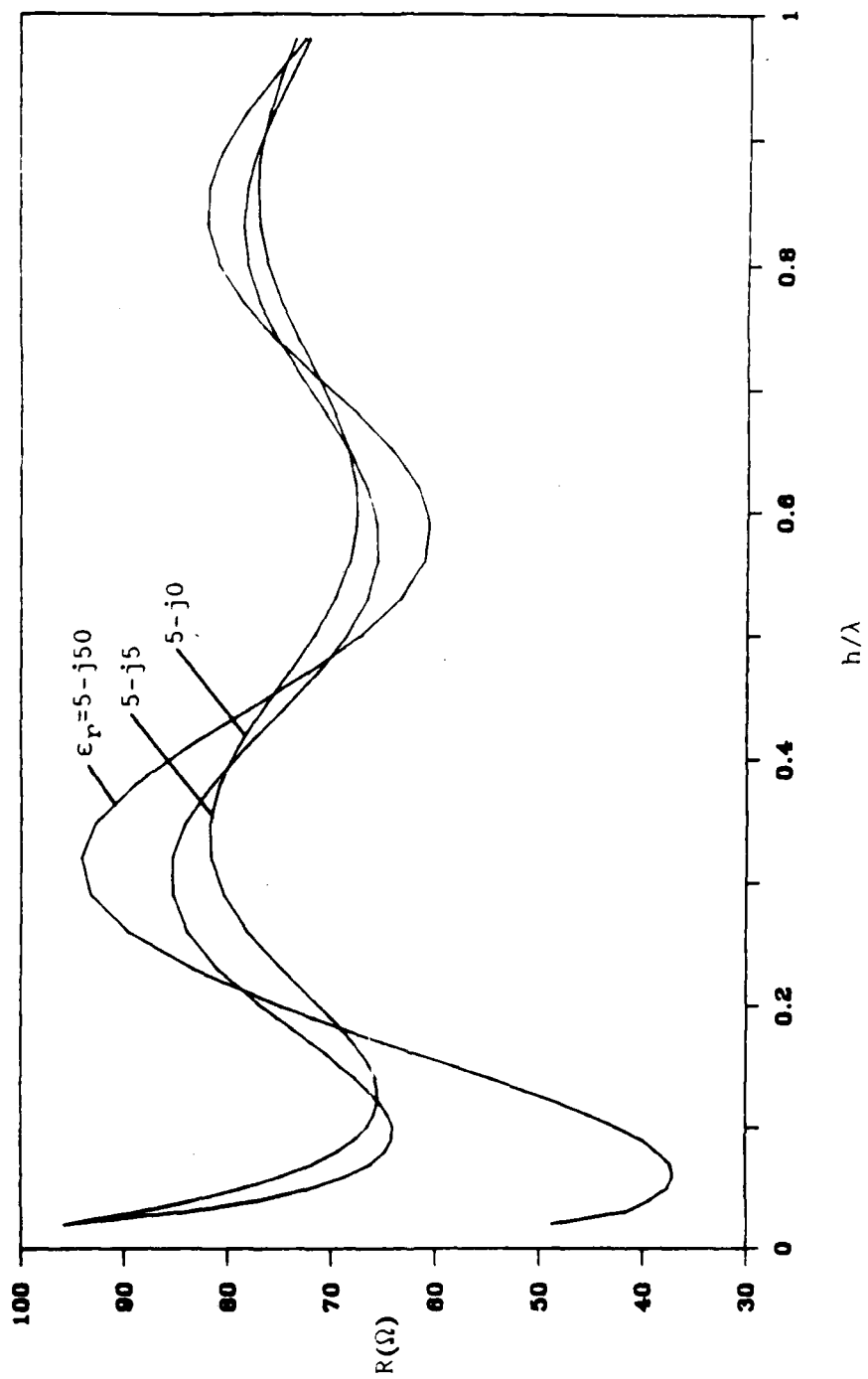


Figure 4.3. Input resistance (R) of half-wave dipole as a function of relative height (h/λ) above various grounds. This compares well with graphs published by Lindell [16].

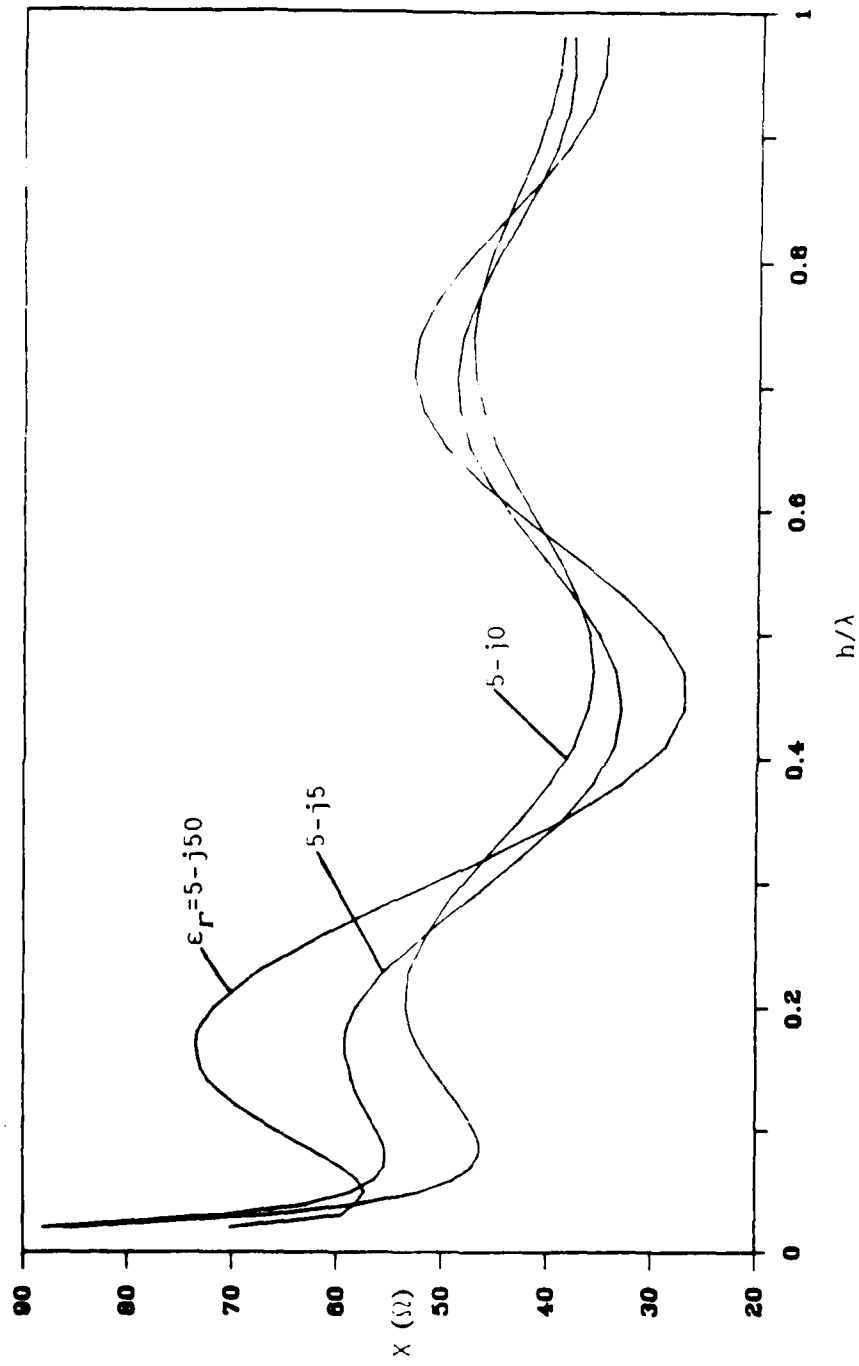


Figure 4.4. Input reactance (X) of half-wave dipole as a function of relative height (h/λ) above various grounds. These graphs do not compare well with those published by Lindell [16]. The reason for this is not known.

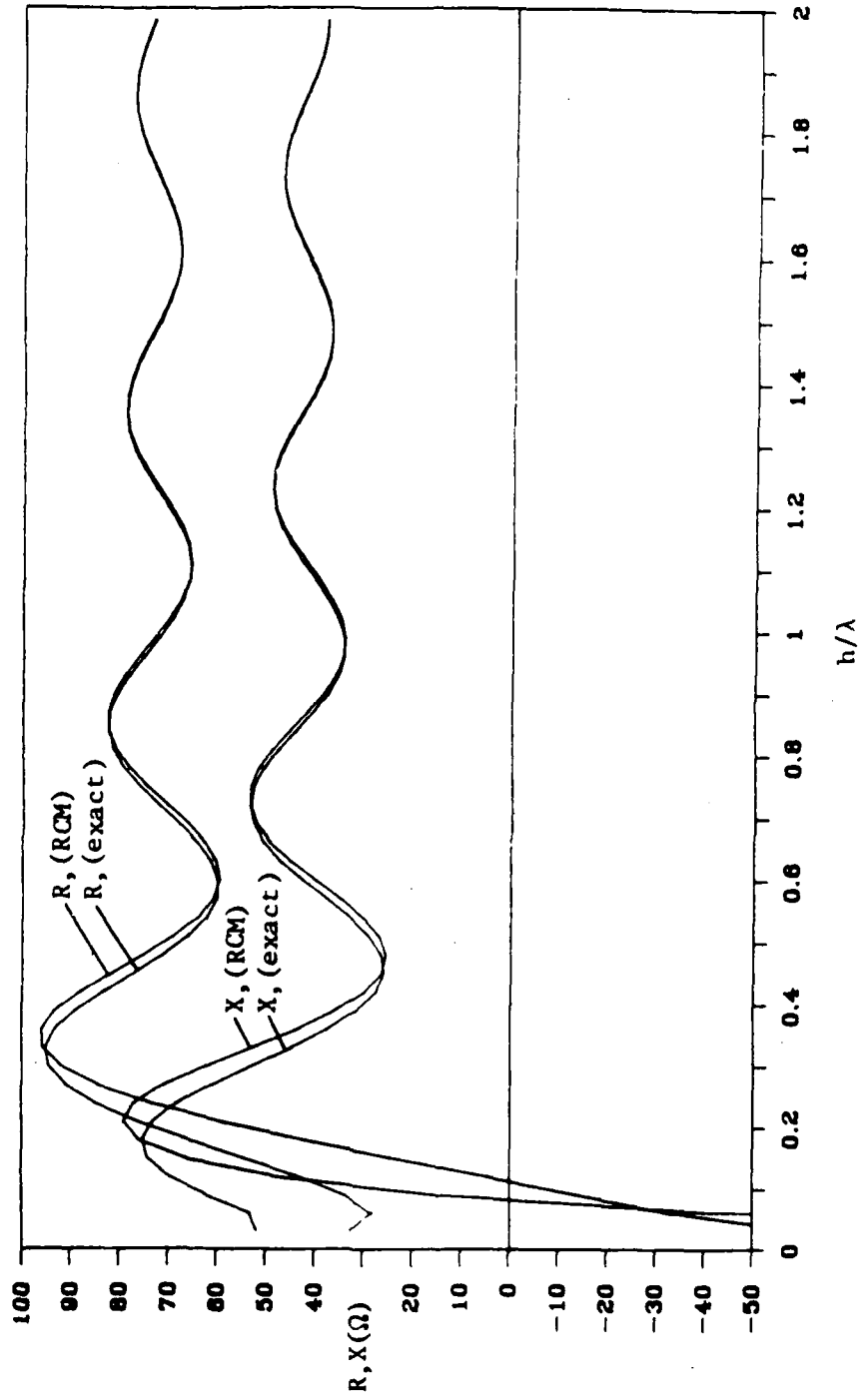


Figure 4.5. Comparison of input impedances for half-wave dipoles calculated using the RCM approximation, Equation (2.63), and direct computation, Equation (2.58), with $\epsilon_r = 10 - j0$.

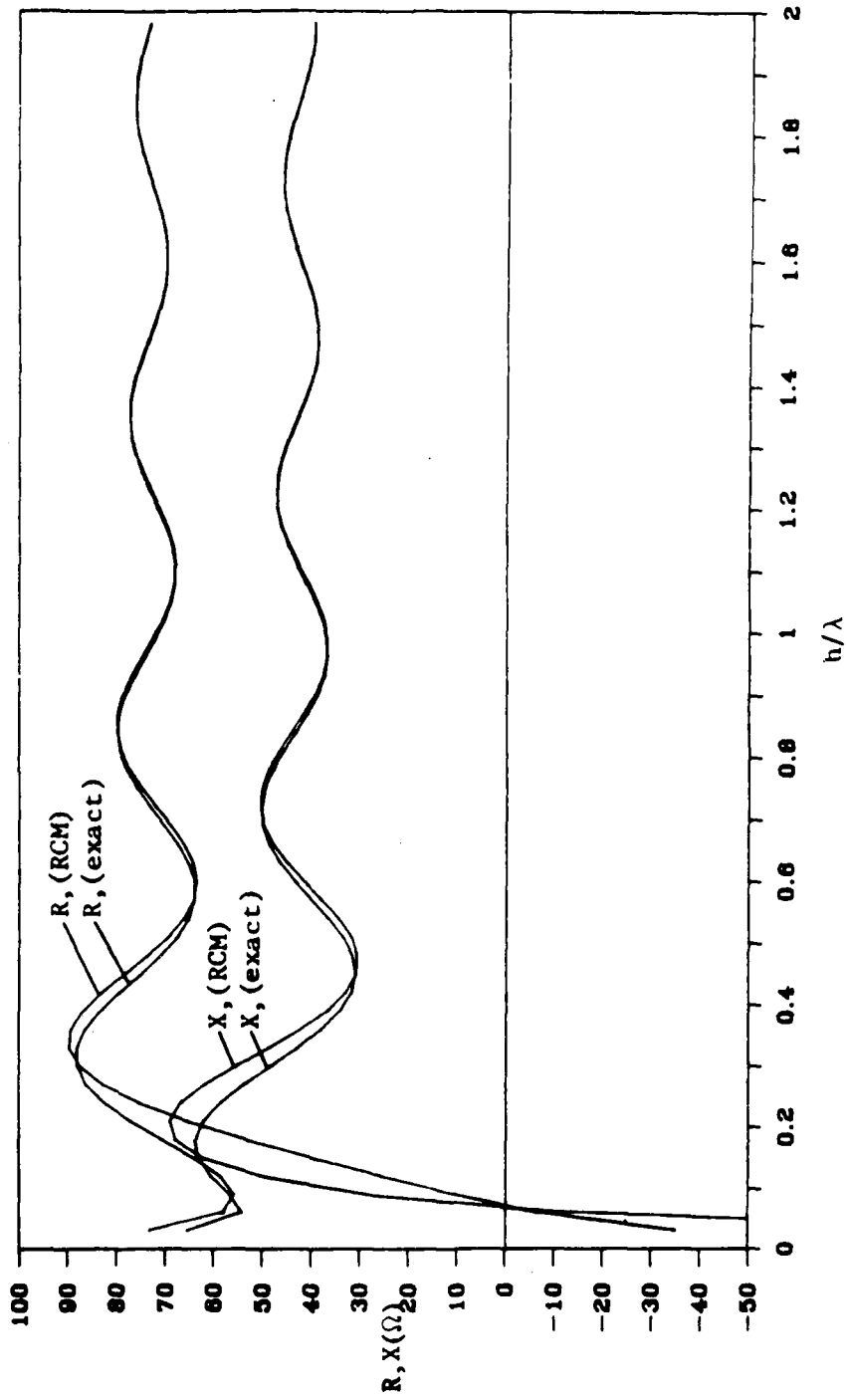


Figure 4.6. Comparison of input impedances for half-wave dipoles calculated using the RCM approximation, Equation (2.63), and direct computation, Equation (2.58), with $\epsilon_r = 10 - j10$.

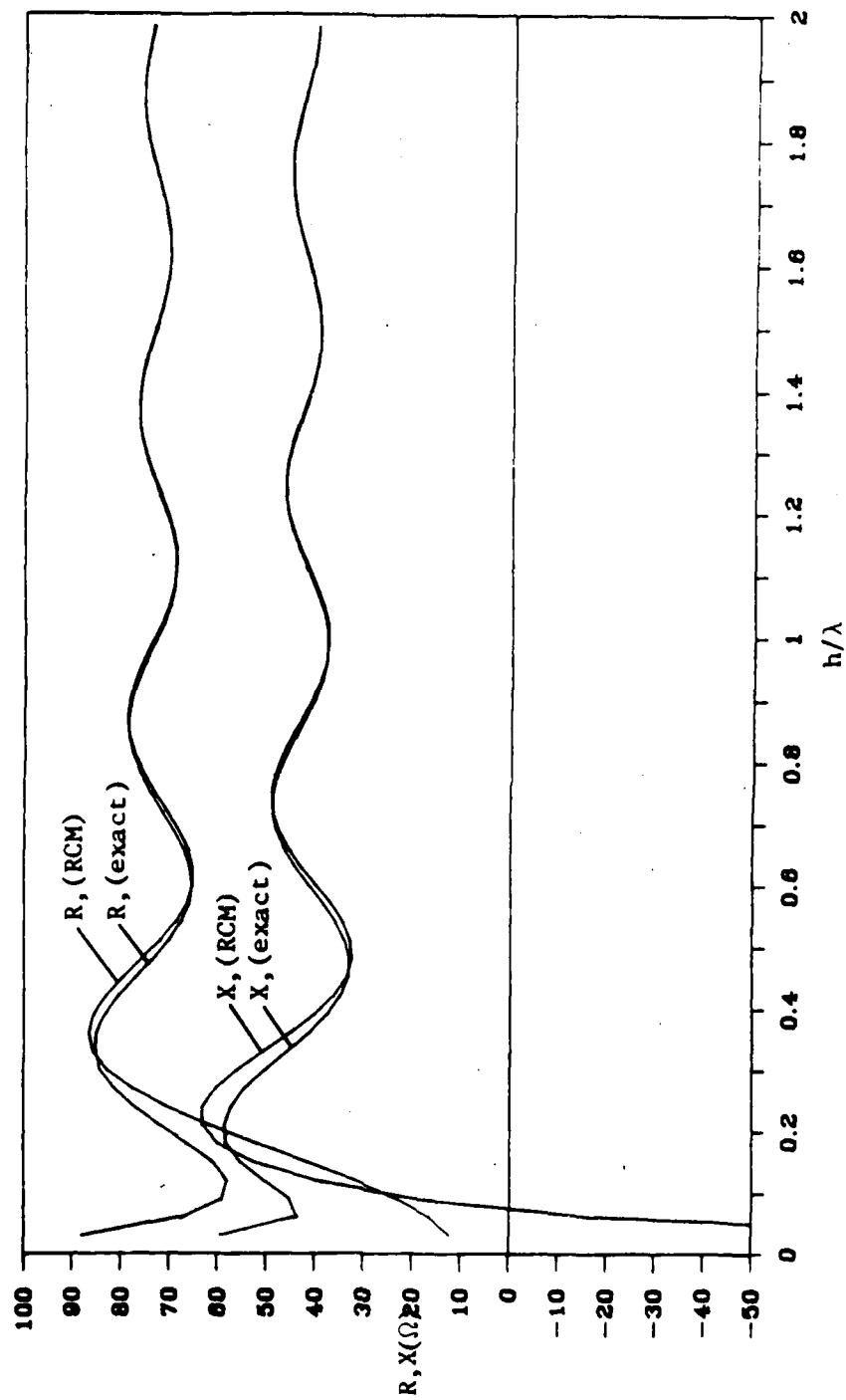


Figure 4.7. Comparison of input impedances for half-wave dipoles calculated using the RCM approximation, Equation (2.63), and direct computation, Equation (2.58), with $\epsilon_r = 10 - j100$.

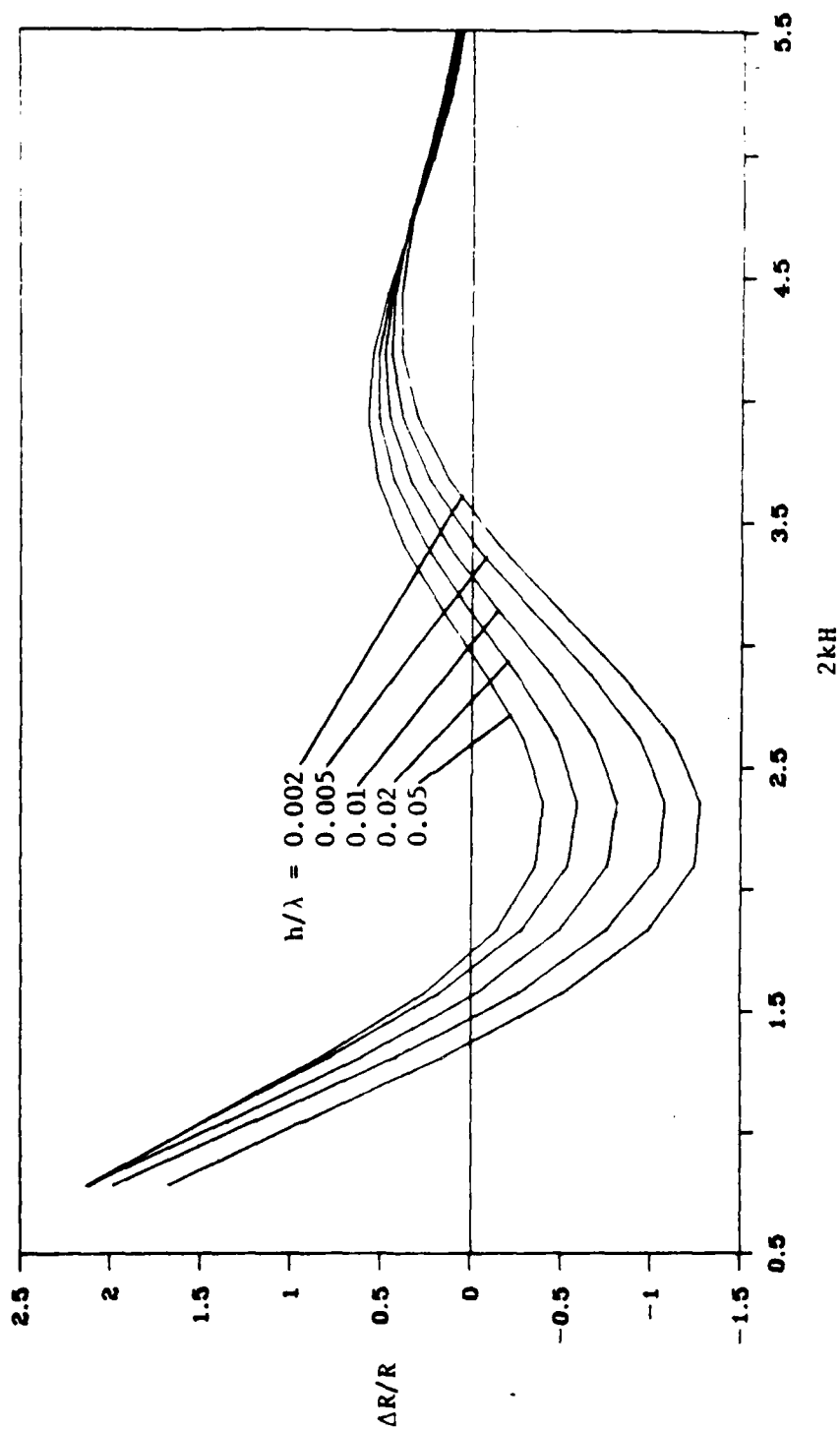


Figure 4.8. Change in input resistance (ΔR) relative to free-space input resistance (R) at different heights above the ground for different length antennas ($2kH$) with $\epsilon_r = 5 - j50$.

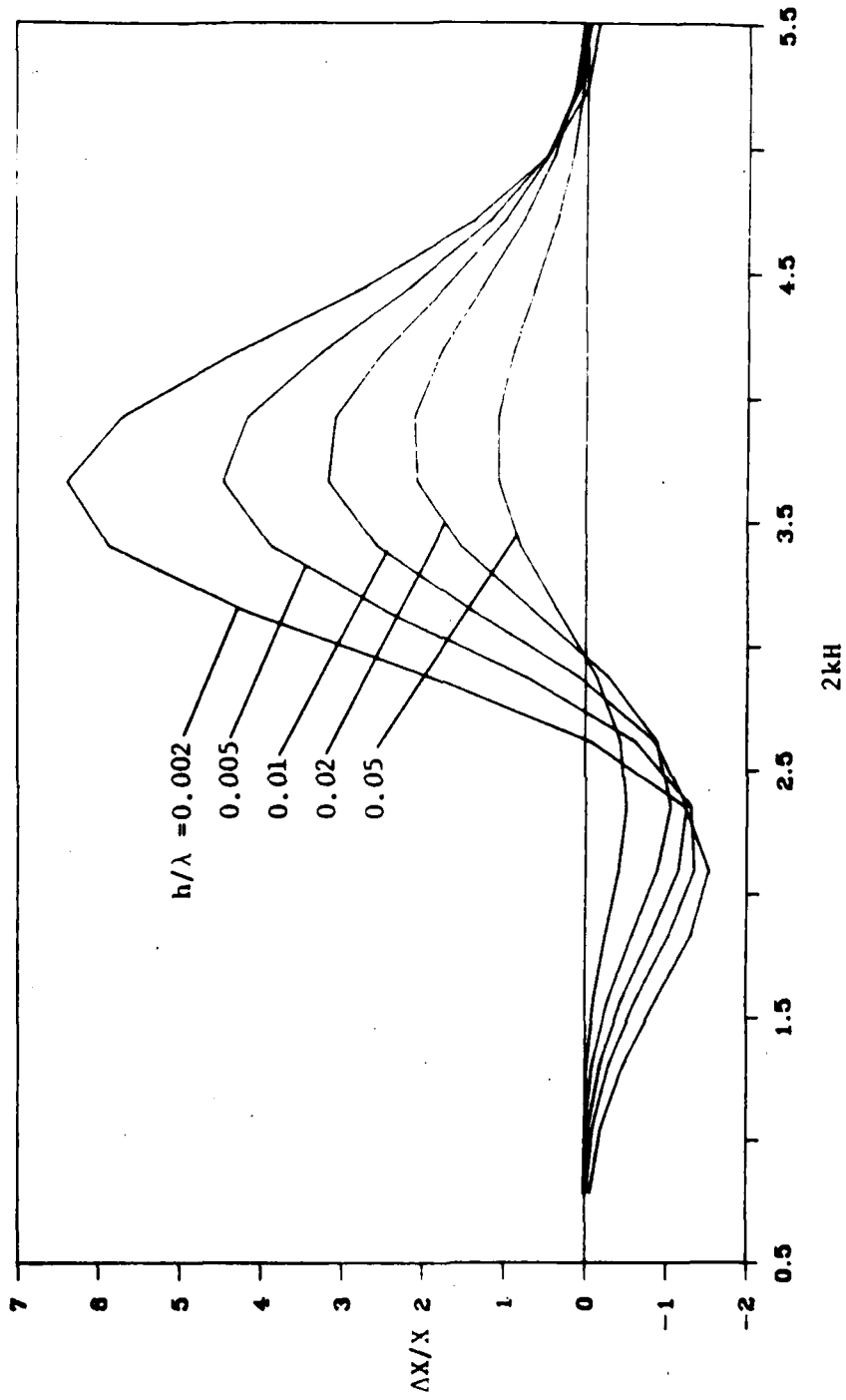


Figure 4.9. Change in input reactance (ΔX) relative to free-space input reactance (X) at different heights above the ground for different length antennas ($2kH$) with $\epsilon_r = 5 - j50$.

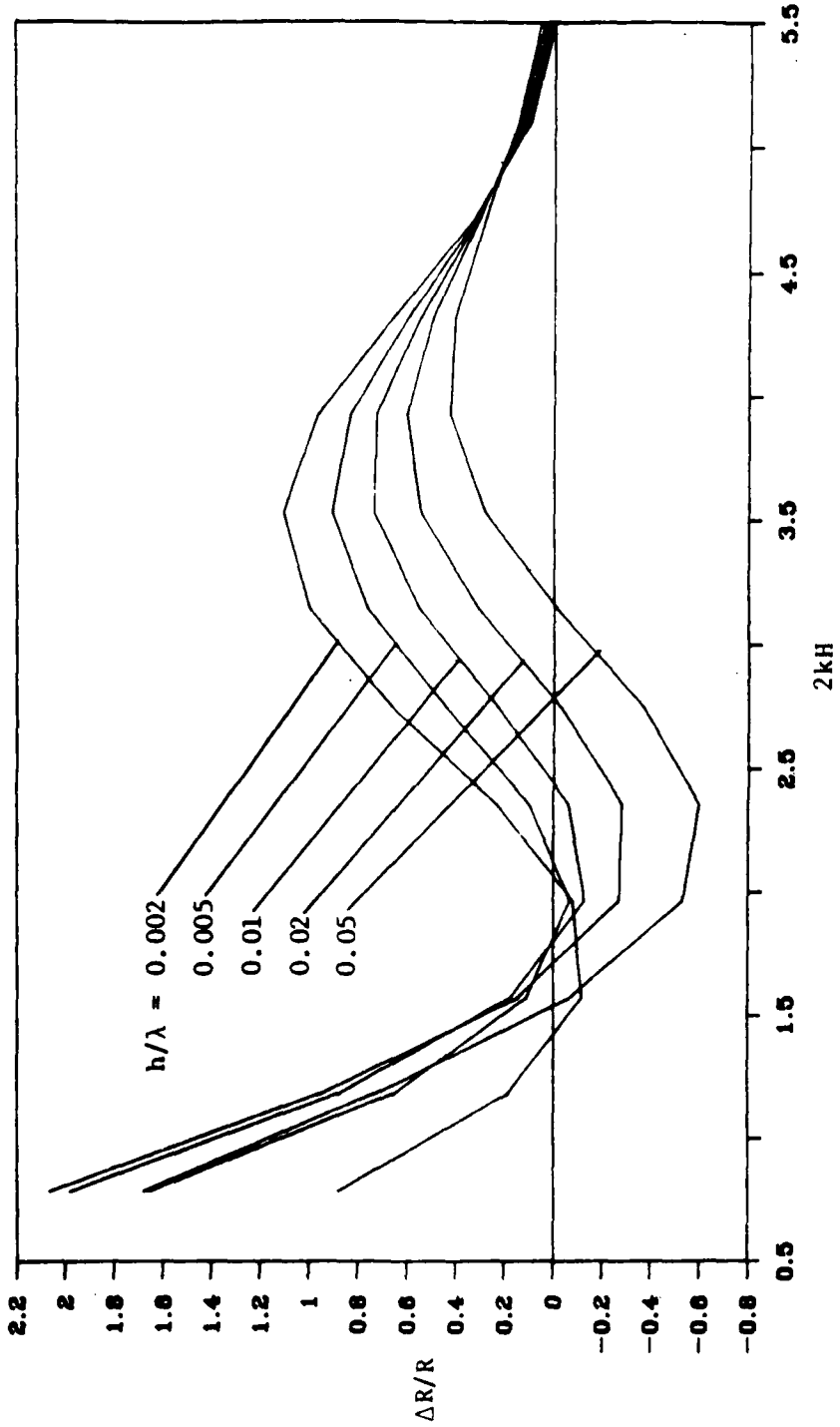


Figure 4.10. Change in input impedance (ΔR) relative to free-space input impedance (R) at different heights above the ground for different length antennas ($2kH$) with $\epsilon_r = 5 - j5$.

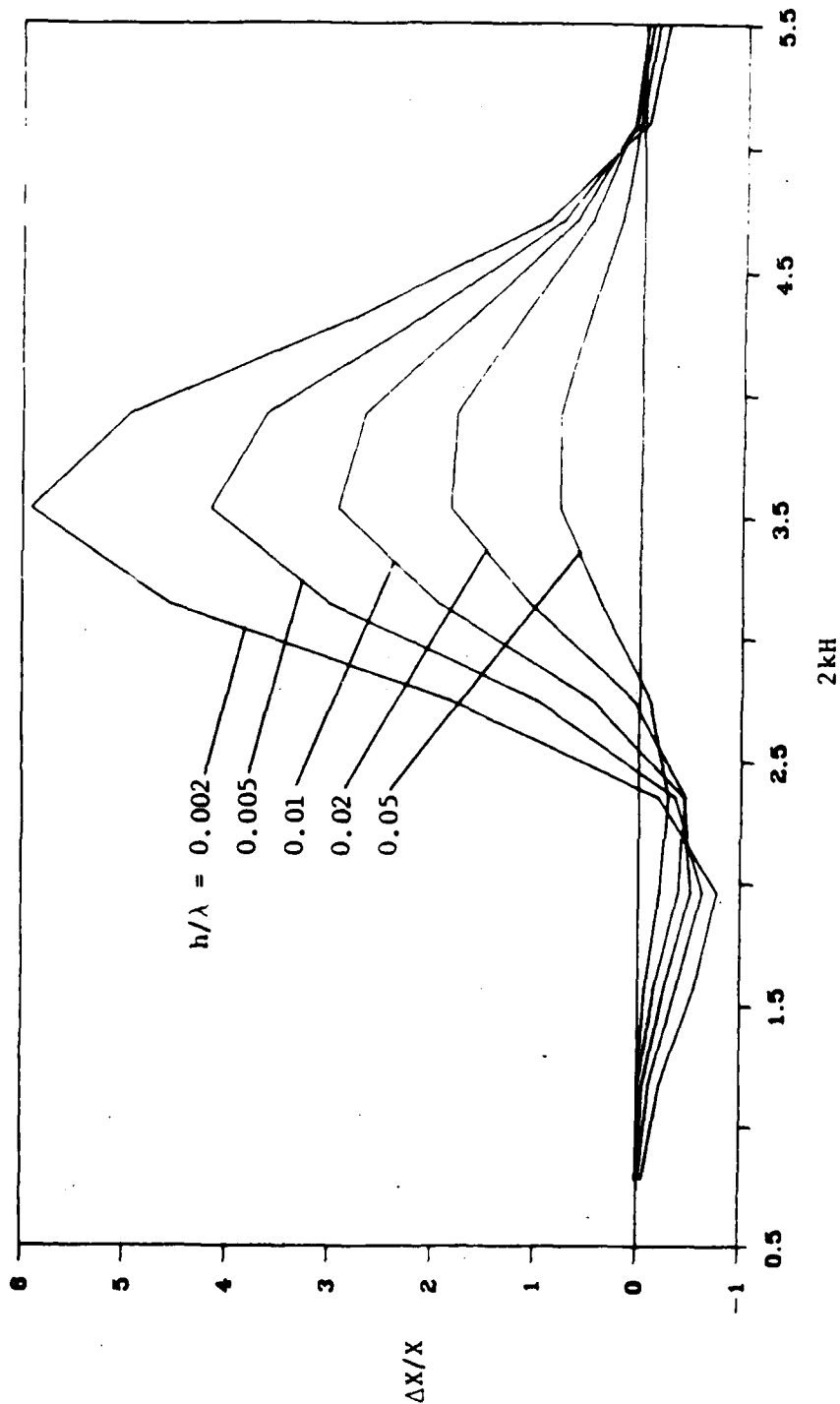


Figure 4.11. Change in input reactance (ΔX) relative to free-space input reactance (X) at different heights above the ground for different length antennas ($2kH$) with $\epsilon_r = 5 - j5$.

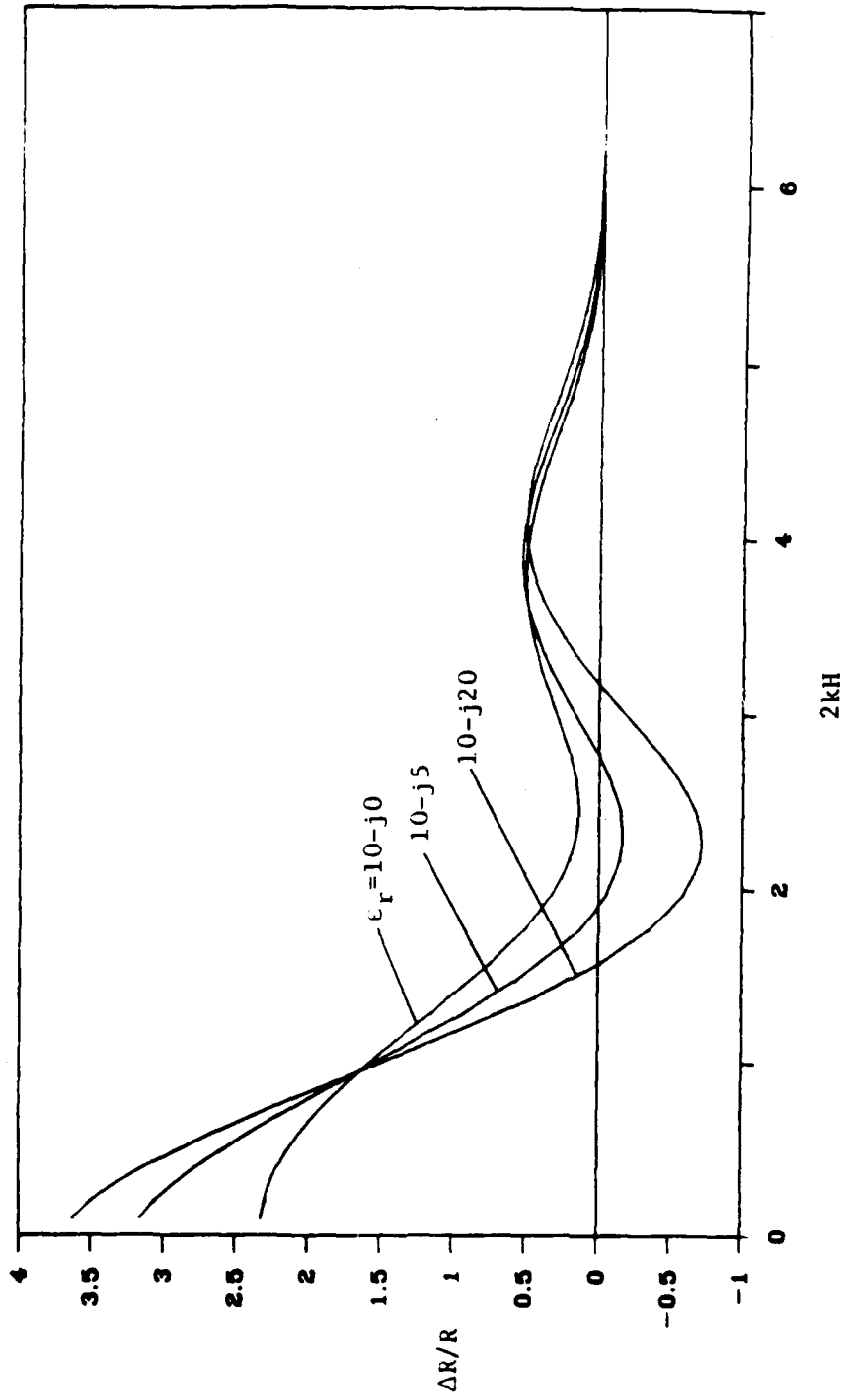


Figure 4.12. Change in input resistance (ΔR) relative to free-space input resistance (R) above various grounds for different length antennas ($2kH$) with $h/\lambda = 0.02$.

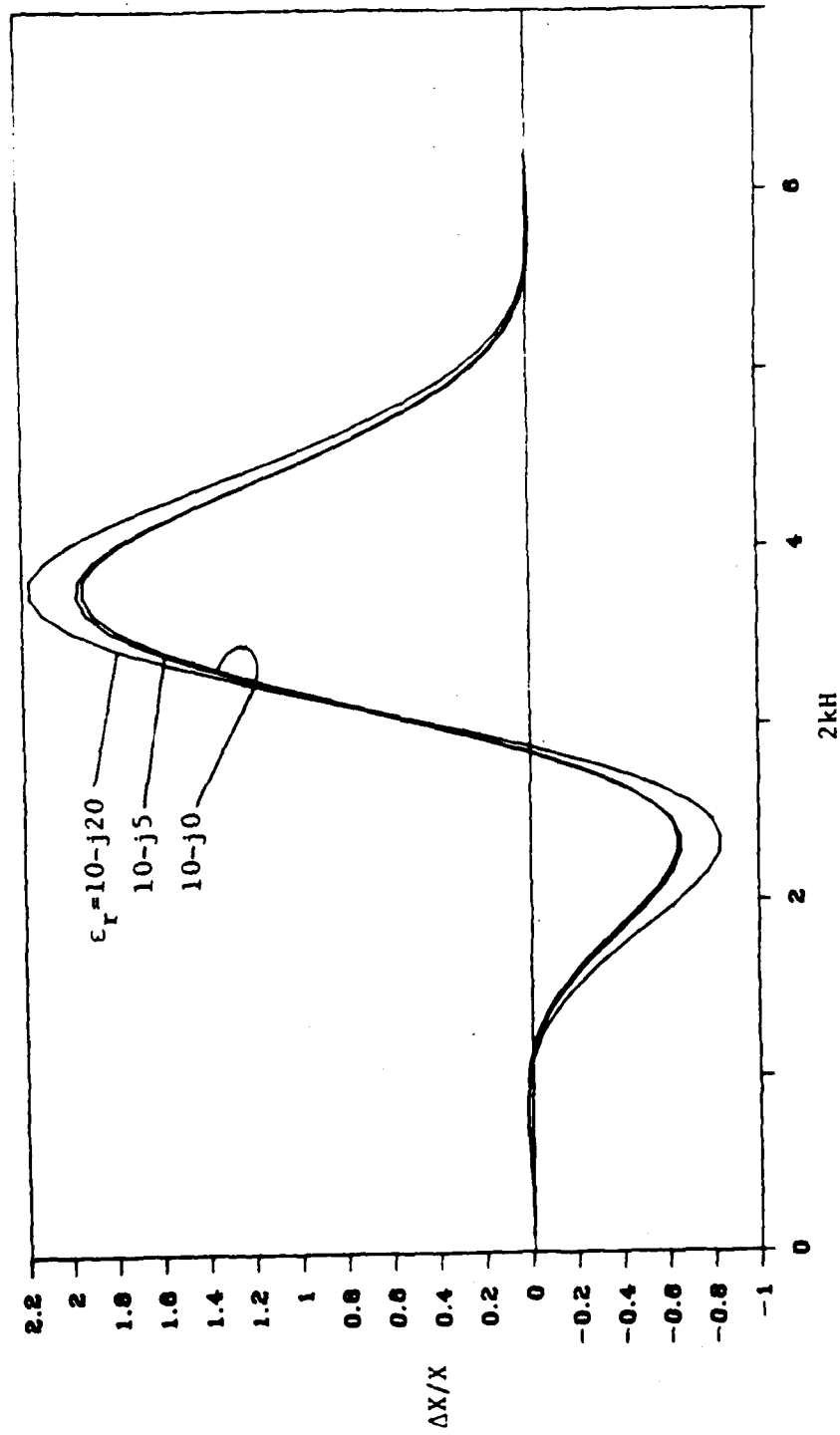


Figure 4.13. Change in input reactance (ΔX) relative to free-space input reactance (X) above various grounds for different length antennas (2kHz) with $h/\lambda = 0.02$.

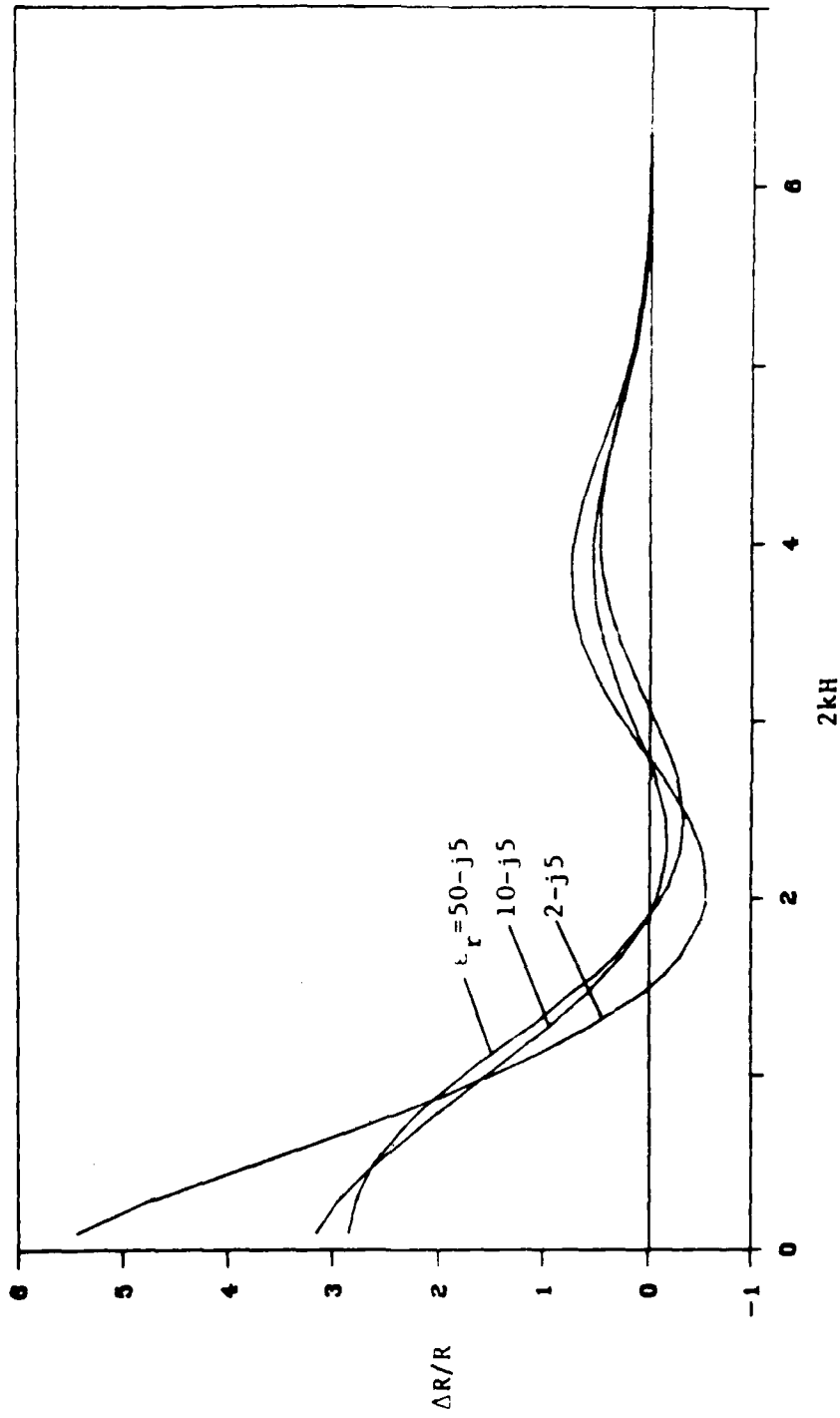


Figure 4.14. Change in input resistance (ΔR) relative to free-space input resistance (R) above various grounds for different length antennas ($2kH$) with $h/\lambda = 0.02$.

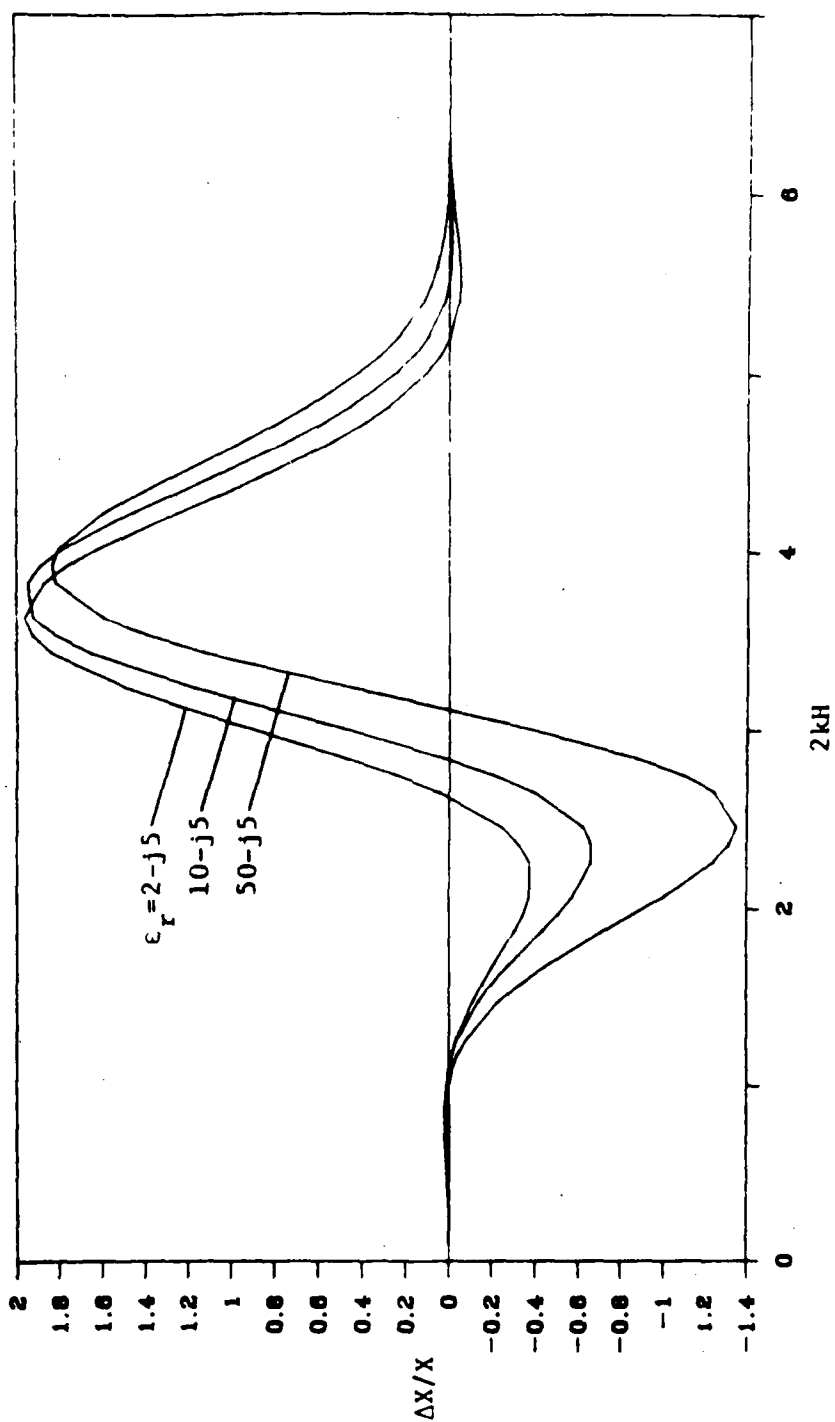


Figure 4.15. Change in input reactance (ΔX) relative to free-space input reactance (X) above various grounds for different length antennas (2kHz) with $h/\lambda = 0.02$.

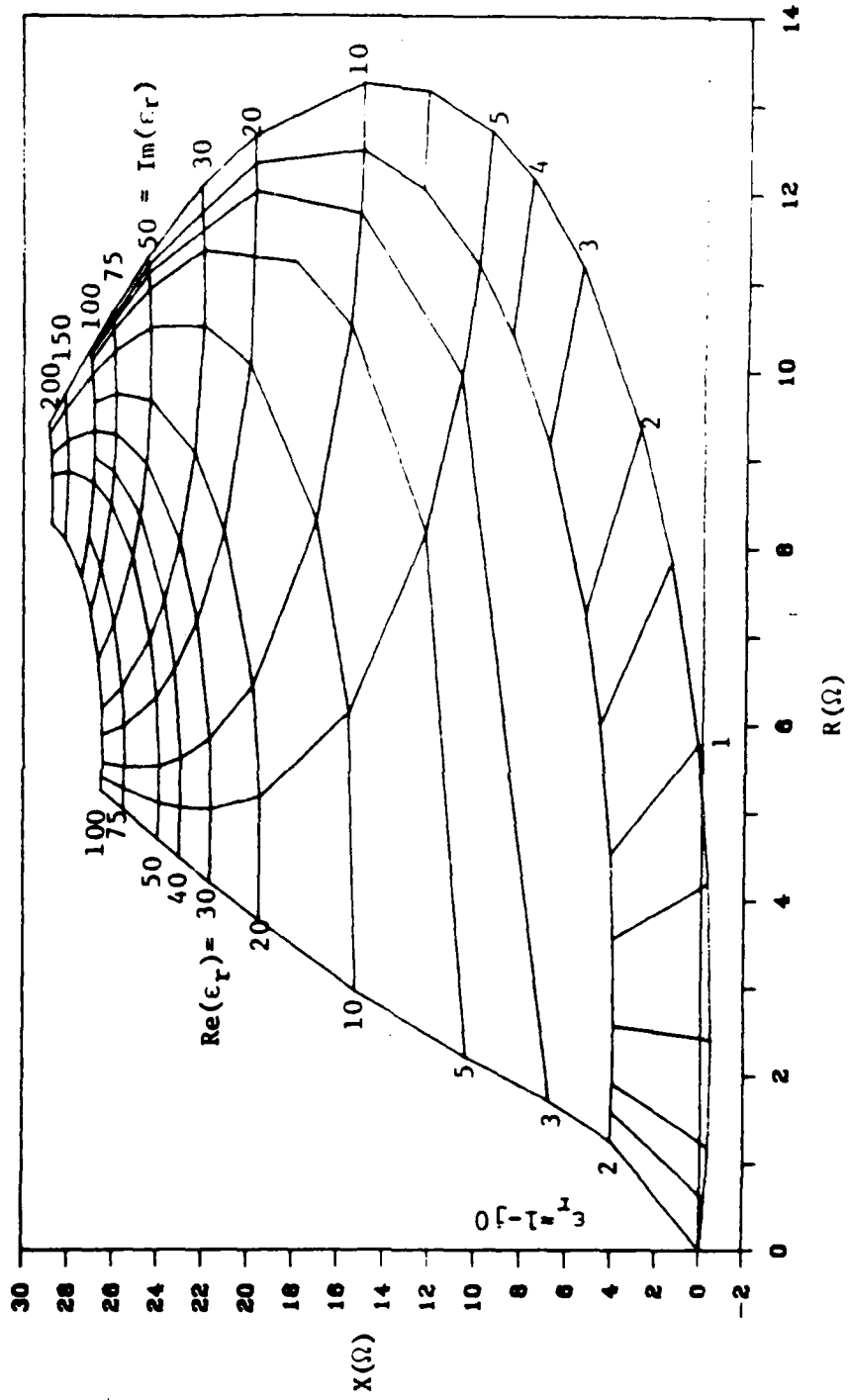


Figure 4.16. Contour map relating half-wave dipole input impedance ($R+jX$) to complex ground permittivity (ϵ_r) with $h/\lambda = 0.233$.

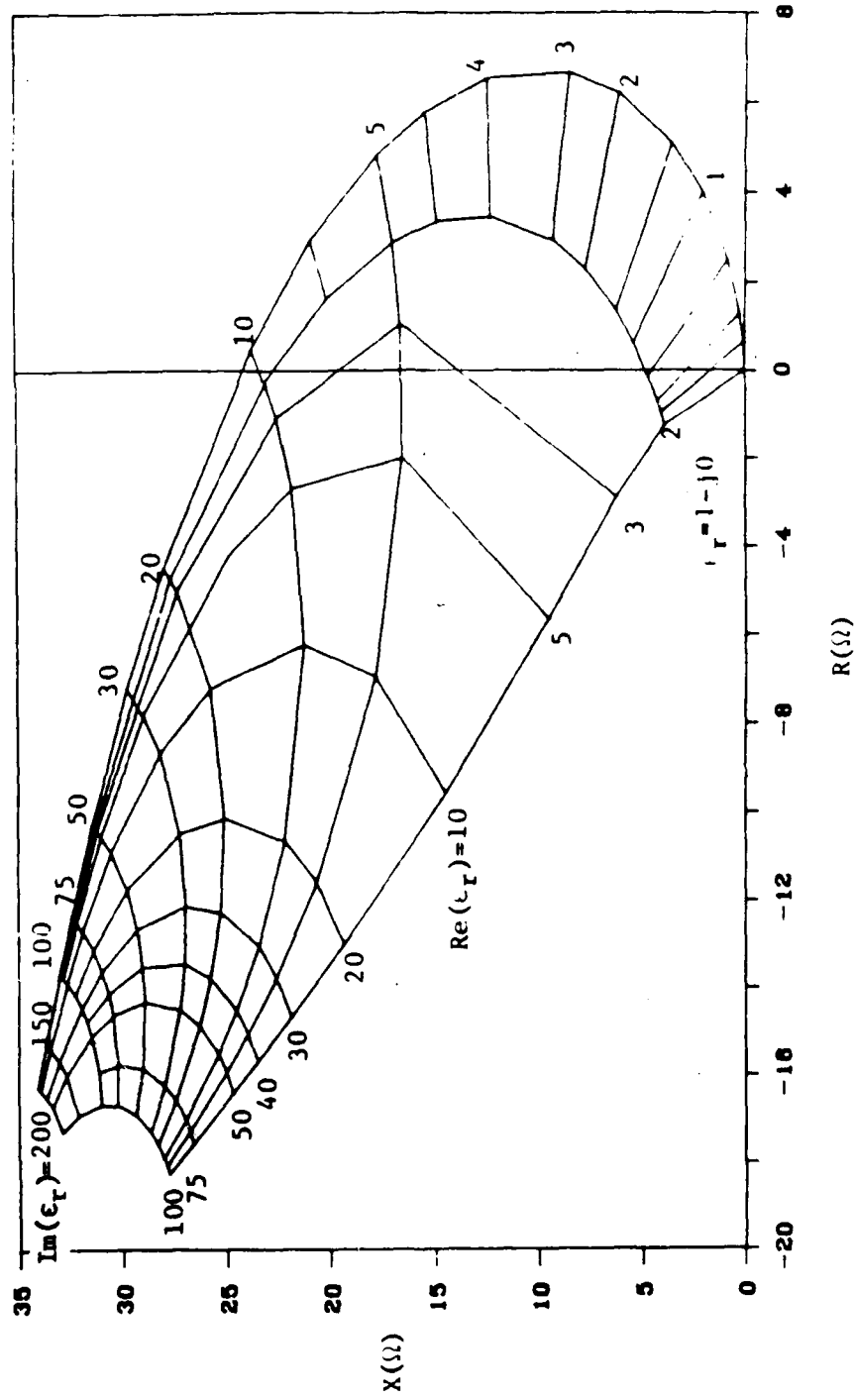


Figure 4.17. Contour map relating half-wave dipole input impedance $(R+jX)$ to complex ground permittivity (ϵ_r) with $h/\lambda = 0.163$.

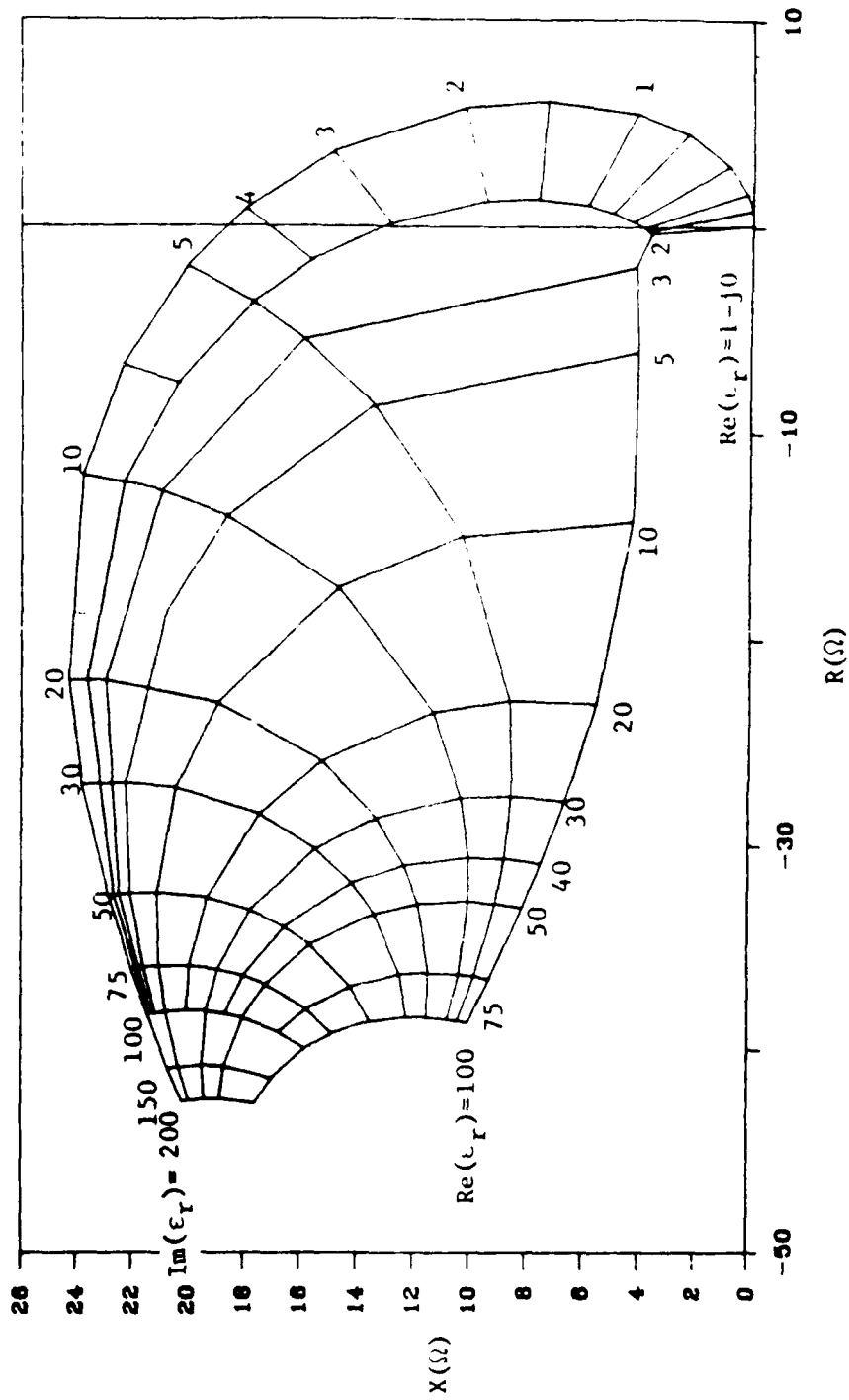


Figure 4.18. Contour map relating half-wave dipole input impedance $(R+jX)$ to complex ground permittivity (ϵ_r) with $h/\lambda = 0.094$.

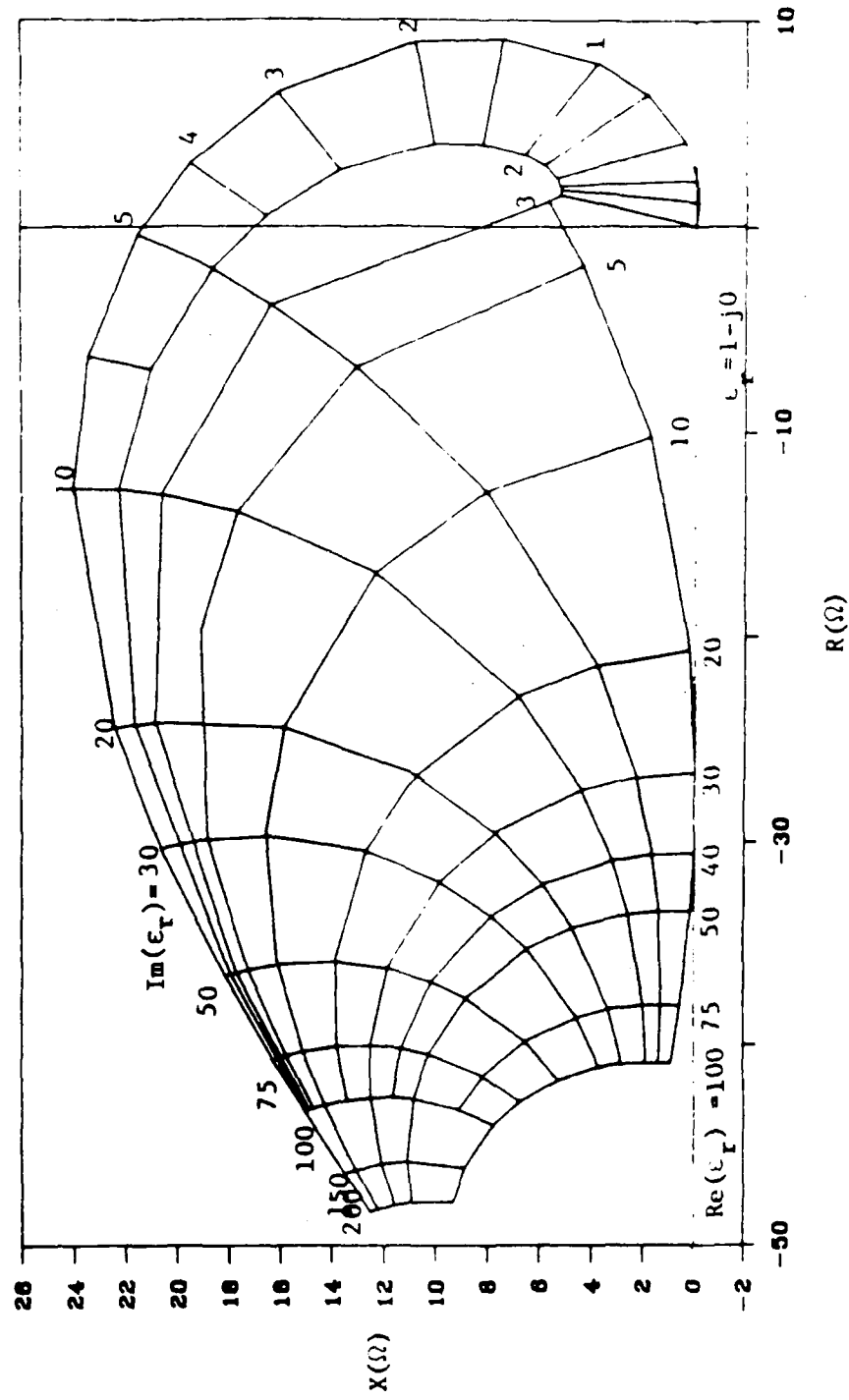


Figure 4.19. Contour map relating half-wave dipole input impedance $(R+jX)$ to complex ground permittivity (ϵ_r) with $h/\lambda = 0.072$.

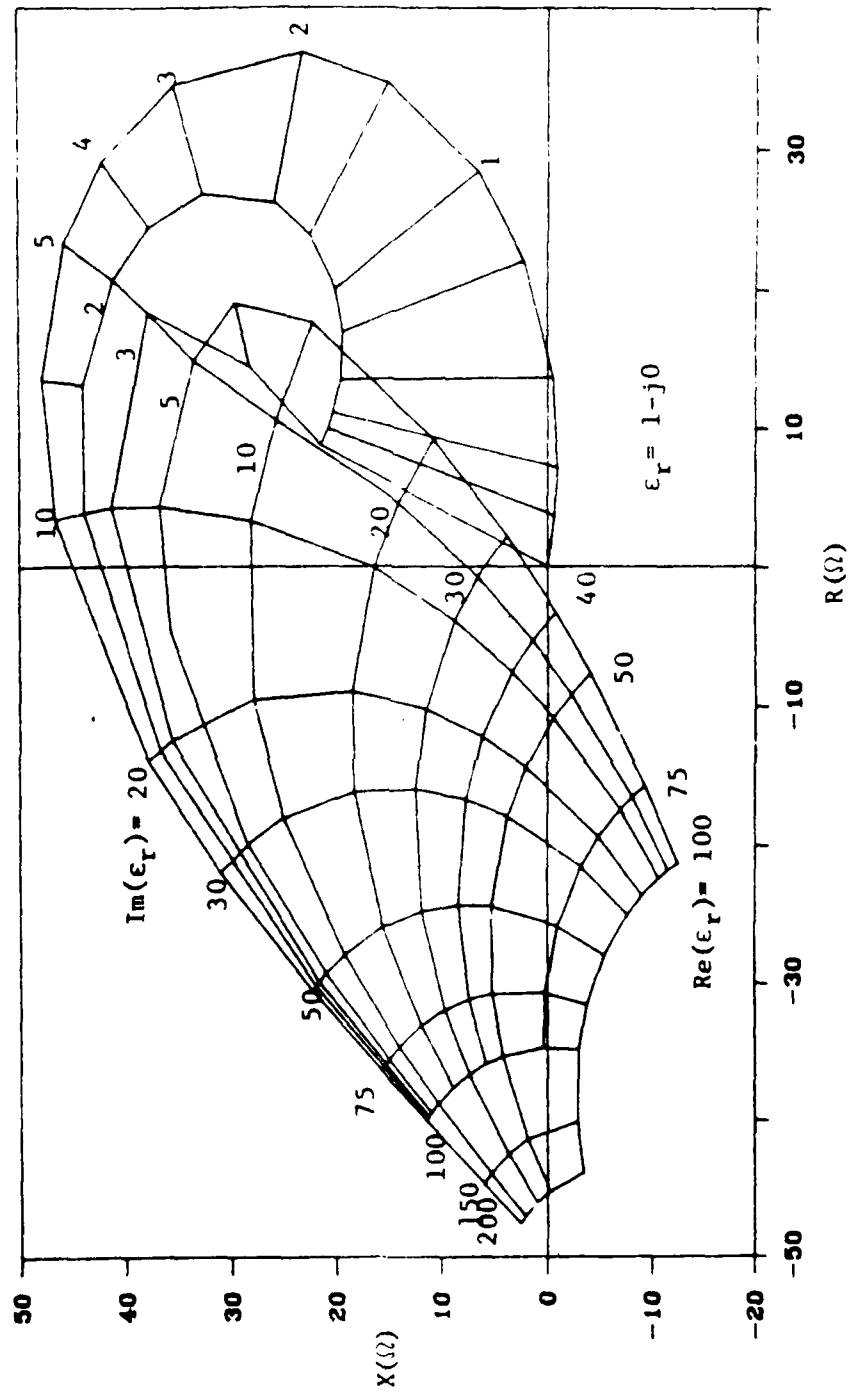


Figure 4.20. Contour map relating half-wave dipole input impedance $(R + jX)$ to complex ground permittivity (ϵ_r) with $h/\lambda = 0.027$.

5. EXPERIMENTAL CONSIDERATIONS

In measuring the input impedance to determine ground permittivity, there are a number of sources of error. These include: 1) impedance measurement; 2) frequency measurement; 3) dipole height; 4) dipole length; 5) free-space impedance; 6) roughness of the ground; 7) inhomogeneities in the ground; 8) change in the current distribution of the dipole due to the ground; and 9) electromagnetic scattering from environment other than the ground.

The first two sources of error are determined by the measuring instrument. If the proper equipment is chosen, these errors can be relatively small.

The height of the dipole is critical, particularly at the lower heights. Figures 4.1 through 4.4 showed that the derivative of ΔZ with respect to the relative height, (h/λ) , of the dipole is large. Hence, even a small error in the height could cause a large error in the permittivity. This source of inaccuracy can be lessened by not placing the antennas too close to the ground.

An error in the measurement of the antenna length has a similar effect as an error in the frequency. It changes the value of $2kH$. An error of this sort may or may not be critical depending on $2kH$ and the permittivity.

Accurate determination of the free-space impedance can also be a problem. To circumvent this, it could be measured, or a contour map relating the permittivity to the difference between input impedances at two different heights could be used.

The extent of the effect of ground roughness on these measurements is difficult to quantify. Of course, it is more important that the ground be smooth directly under the antenna than farther away.

The effect of ground roughness on these measurements is twofold. It decreases the certainty of the height measurement and changes the scattering properties of the half space. For best results, the ground should be as smooth as possible with little or no vegetation. Of course, it is more important that the ground be smooth directly beneath the dipole than farther away.

Inhomogeneities in the ground could be the source of considerable error. Care must be taken to insure there are no pipes or cables buried near the test area. Natural inhomogeneities, such as stratification, can also distort measurements. If stratification does not occur before one skin depth,

$$\delta = \left(\omega \sqrt{\frac{\mu\epsilon}{2} \left(\sqrt{\left(1 + \frac{\sigma^2}{\omega^2\epsilon^2}\right)} - 1 \right)} \right)^{-1}, \quad (5.1)$$

its effect on the impedance will be small. A possible means of compensating for stratification would be to take measurements at a number of different heights and frequencies and use a parameter optimization routine along with the theory presented in [25] to determine the permittivity and depth of each layer of earth.

In Chapter 1, it was assumed that the dipole current distribution is sinusoidal and that the presence of the earth has no effect on that distribution. Of course, neither of these assumptions is true. However, they do provide a good approximation. According to Lindell [16], the fields scattered from the earth induce negligible change in the dipole current if $h \gg \delta_a/2$, where δ_a is defined to satisfy the equation

$$ka = 2k\delta_a e^{-1/k\delta_a}. \quad (5.2)$$

here a is the radius of the dipole. Figures 5.1 and 5.2 are plots of $h/\lambda = \delta_a/2\lambda$ for different frequencies and radii. The regions above these curves correspond to $h > \delta_a/2$. Finally, the measuring equipment and other objects should be placed as far from the antenna as possible.

Of all the possible sources of error, only the current distribution is unique to the theory presented here. Most other experimental procedures will be prone to the same or parallel problems.

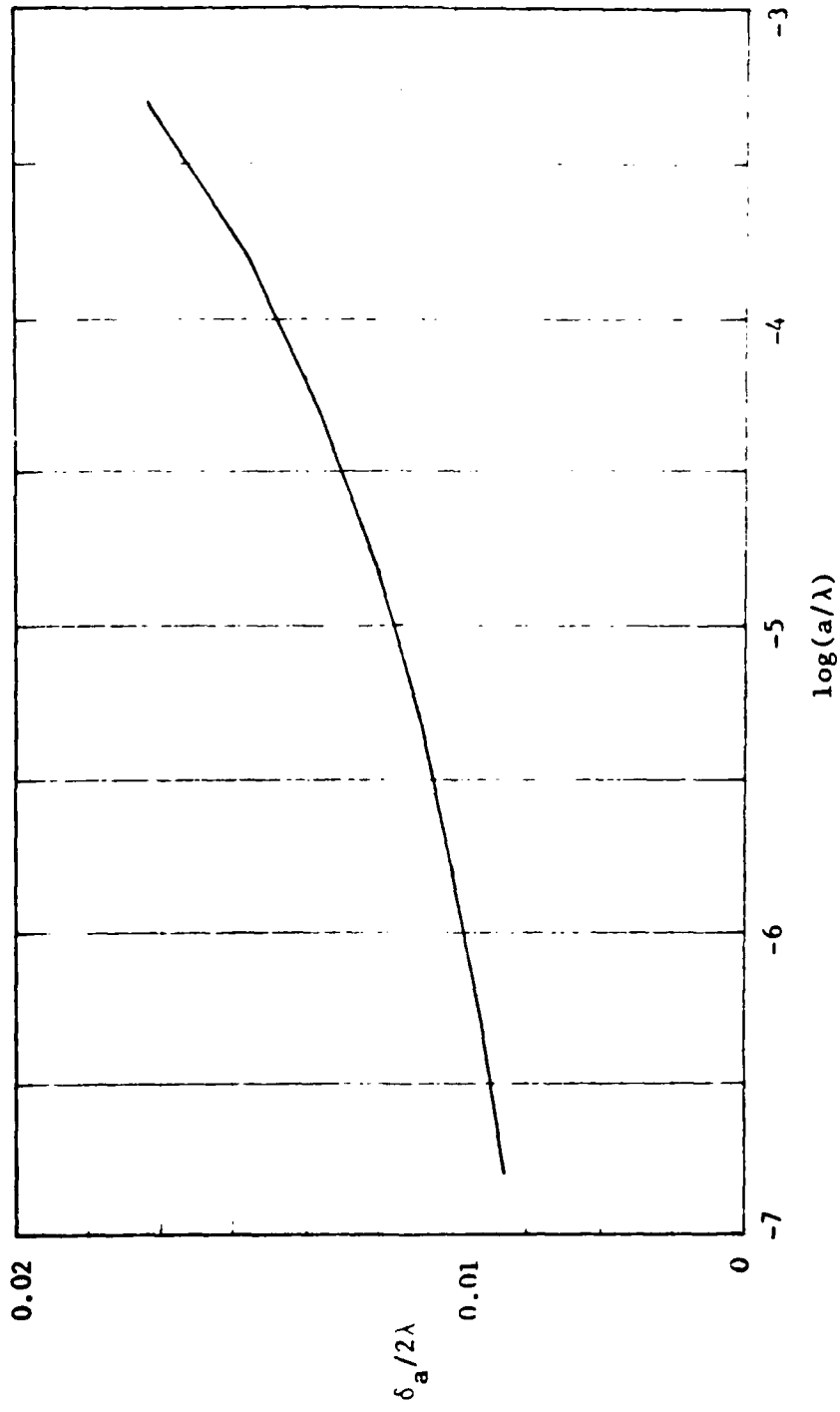


Figure 5.1. Relationship between $\delta_a/2\lambda$ and $\log(a/\lambda)$. The relationship $h/\lambda \gg \delta_a/2\lambda$ must hold true for impedance calculations to be valid.

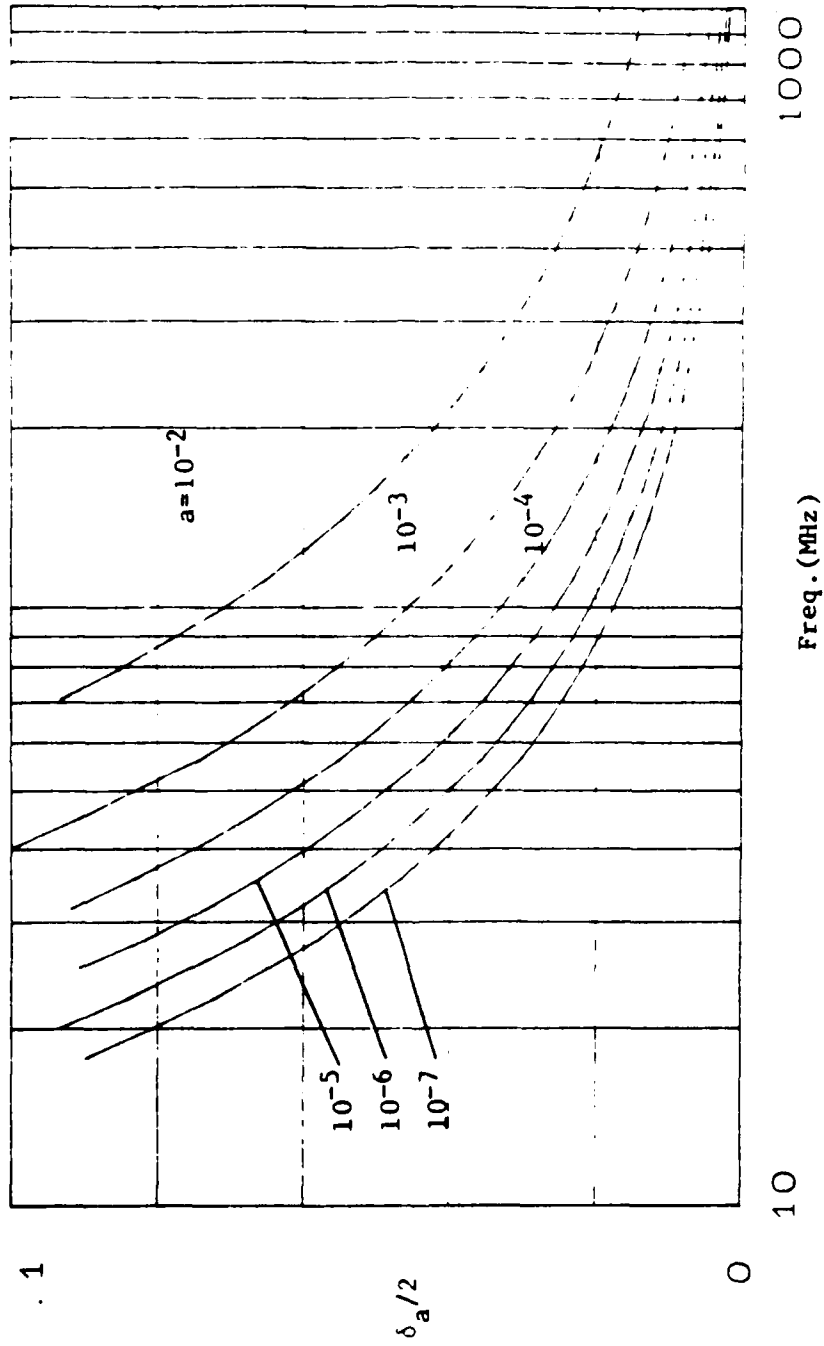


Figure 5.2. Relationship between $\delta_a/2\lambda$ and frequency for various antenna radii. The relationship $h/\lambda \gg \delta_a/2\lambda$ must hold true for impedance calculations to be valid.

6. CONCLUDING REMARKS

The theory between the electric properties of the ground to the input impedance of a horizontal electric dipole has been presented. The necessary numerical computations were discussed. Then patterns of the input impedance were illustrated with respect to the height and length of the dipole. Practical considerations were discussed. Finally, recommendations were made for experimental methods of determining the ground permittivity using this theory.

Attempts were made to experimentally validate the techniques mentioned herein. However, these attempts were unsuccessful. The primary reasons for this are thought to be parasitic reactances at the feed point and scattering from equipment used in the experiment.

Despite the shortcomings of the present study, it is the opinion of the author that the input impedance of a dipole should be a good—although perhaps not the best—means of determining ground permittivity. One possible improvement to this technique would be to use a slot antenna with a more directional radiation pattern. This would increase the dependence of the input impedance on the properties of the earth while decreasing its sensitivity to the measuring equipment nearby. The parasitic reactances would be decreased.

An improvement that could be made to the theory would be the replacement of the integral to infinity in Equations (2.53) and (2.54) by one or two series representations. This would decrease the computation time enough to make it practical to iteratively determine the current distribution on the dipole before using the stationary functional (Equation (2.50)) to compute the input impedances.

LIST OF REFERENCES

- [1] J. L. Nicol, "The input impedance of horizontal antennas above an imperfect plane earth," *Radio Sci.*, vol. 15, no. 3, pp. 471-477, May-June 1980.
- [2] M. Mostafavi and R. Mittra, "Remote probing of inhomogeneous media using parameter optimization techniques," *Radio Sci.*, vol. 7, no. 12, pp. 1105-1111, Dec. 1972.
- [3] A. G. Tijhuis, "Iterative determination of permittivity and conductivity profiles of a dielectric slab in the time domain," *IEEE Trans. Antennas Propag.*, vol. AP-29, no. 2, pp. 239-245, March 1981.
- [4] A. G. Tijhuis and Cor Van Der Worm, "Iterative approach to the frequency solution of the inverse scattering problem for an inhomogeneous lossless dielectric slab," *IEEE Trans. Antennas Propag.*, vol. AP-32, no. 7, pp. 711-716, July 1984.
- [5] C. L. Bennett, "Time domain inverse scattering," *IEEE Trans. Antennas Propag.*, vol. AP-29, no. 2, pp. 213-219, March 1984.
- [6] A. Sommerfeld. "Über die ausbreitung der wellen in der drahtlosen telegraphie," *Annal. Phys.*, vol. 28, pp. 665-736, 1909.
- [7] P. Parhami, Y. Rahmat-Samii, and R. Mittra, "An efficient approach for evaluating Sommerfeld integrals encountered in the problem of a current element radiating over a lossy ground." *IEEE Trans. Antennas Propag.*, vol. AP-28, no. 1, pp. 100-104, Jan. 1980.
- [8] W. C. Kuo and K. K. Mei, "Numerical approximations of the Sommerfeld integral for fast convergence," *Radio Sci.*, vol. AP-13, no. 3, pp. 407-415, May-June 1979.
- [9] E. F. Kuester and D. C. Chang, "Evaluation of Sommerfeld integrals associated with dipole sources above the earth," Univ. of Colorado Electromagnetic Lab. Rep. No. 43, Jan. 1979.
- [10] P. R. Bannister, "Summary of image theory expressions for the quasistatic fields of antennas at or above the earth's surface," *Proc. IEEE*, vol. 67, no. 7, pp. 1001-1008, July 1979.
- [11] S. F. Mahmoud and Ahmed D. Metwally, "New image representation for dipoles near a dissipative earth 1. Discrete images 2. Discrete and continuous images," *Radio Sci.*, vol. 16, no. 6, pp. 1271-1275, Nov.-Dec. 1981.

- [12] J. R. Wait, "Image theory of quasistatic magnetic dipole over a dissipative half space," *Electron. Lett.*, vol. 5, no. 13, pp. 281-282, May 20, 1969.
- [13] I. V. Lindell and E. Alanen, "Exact image theory for the Sommerfeld half-space problem, Part III: General Theory." *IEEE Trans. Antennas Propag.*, vol. AP-32, no. 10, pp. 1027-1032, Oct. 1984.
- [14] I. V. Lindell and E. Alanen, "Exact image theory for the Sommerfeld half-space problem, Part I: Vertical magnetic dipole." *IEEE Trans. Antennas Propag.*, vol. AP-32, no. 2, pp. 126-133, Feb. 1984.
- [15] I. V. Lindell and E. Alanen, "Exact image theory for the Sommerfeld half-space problem, Part II: Vertical electric dipole." *IEEE Trans. Antennas Propag.*, vol. AP-32, no. 8, pp. 841-847, Aug. 1984.
- [16] I. V. Lindell, E. Alanen, and Kari Mannersalo, "Exact image method for impedance computation of antennas above the ground." *IEEE Trans. Antennas Propag.*, vol. AP-33, no. 9, pp. 937-945, Sept. 1985.
- [17] G. E. Roberts and H. Kaufman, *Table of Laplace Transforms*. Philadelphia: W. B. Saunders Co., 1966.
- [18] M. Abramowitz and L. A. Stegun, *Handbook of Mathematical Functions*. New York: Dover, 1965, p. 1025.
- [19] A. Papoulis, *The Fourier Integral and its Applications*. New York: McGraw-Hill Book Co., pp. 277-278, 1962.
- [20] A. P. Prudnikov, Y. A. Brychkov, and O. I. Marichev, *Integrals and Series, vol. 2: Special Functions*. New York: Gordon and Breach Science Publishers, 1986, p.189.
- [21] I. S. Gradshteyn and I. M. Ryzhik, *Tables of Integrals, Series, and Products*. Academic Press, Inc., 1980.
- [22] G. J. Burke, E. K. Miller, J. N. Brittingham, D. L. Lager, R. J. Lytle, and J. T. Okada, "Computer modeling of antennas near the ground," *Electromagnetics*, vol. 1, no. 1, Jan. - March 1981.
- [23] I. V. Lindell and E. Alanen, "Applications of exact image theory in antenna and field calculations in the presence of a dissipative half space," *Conference Proceedings - 15th European Microwave Conference*, Turnbridge Wells, England: Microwave Exhibitions & Publ. Ltd., Sept. 9-13, 1985, pp. 427-432.
- [24] C. A. Balanis, *Antenna Theory*. New York: Harper & Row, pp. 292-295, 1982.
- [25] E. Alanen, I. V. Lindell, and A.T. Hujanen, "Exact image method for field calculation in horizontally layered medium above a conducting ground plane," *IEE Proc.*, vol. 133, part H, no. 4, August 1986.

DISTRIBUTION

HQUSACE

ATTN: CEEC-E (2)

ATTN: CERD-L

ATTN: CEIM-SL (2)

USAHSC, ATTN: Library 22060

ATTN: DET III 79906

US Army Engineer Districts

ATTN: Library (41)

US Army Engineer Divisions

ATTN: Library (14)

US Army Engineer District, Omaha 68102

ATTN: Chief, Engr Div

US Army Engr Div, Huntsville 35807

ATTN: Chief, HNDED-SR

USA Natick, R&D Ctr 01760-5017

Naval Air Systems Command

ATTN: Library

Hanson AFB, MA 01731

ATTN: HQ AFSC

ATTN: ESD/OCR-3

Naval Civil Engr Lab

ATTN: Library 93041

Harry Diamond Labs 20783

ATTN: SLCHD-NW

ATTN: SLCHD-NW-E

ATTN: SLCHD-NW-EP (10)

ATTN: SLCHD-NW-EH

ATTN: SLCHD-NW-ES

ATTN: SLCHD-CS

Defense Nuclear Agency 20305-1000

ATTN: DNA-RAAE

Defense Technical Info. Center 22314

ATTN: DDA (2)

U.S. Govt Printing Office 22304

Receiving Sect/Depository (2)